The Volumetric Rate of Superluminous Supernovae from the Dark Energy Survey

by

Benjamin Peter Thomas

UNIVERSITY OF PORTSMOUTH

This thesis is submitted in partial fulfilment of
the requirements for the award of the degree of
Doctor of Philosophy of the University of Portsmouth.

June, 2019

Abstract

Superluminous supernovae (SLSNe) are a recently discovered class of supernovae (SNe) whose peak luminosities reach more than ten times that of Type Ia SNe. The explosion physics and progenitor systems of SLSNe are poorly understood, but population studies can constrain the possibilities. For example, the volumetric rate of SLSNe should follow the cosmic star formation history if their progenitors are massive stars, and can therefore give a strong indication towards their origin. The volumetric rate is also a critical quantity needed to predict the number of SLSNe that will be detected in the future, informing the observing strategy of upcoming transient surveys.

The Dark Energy Survey (DES) Supernova Survey ran for $\sim$5.5 months each year for five years (2013 - 2018) with a nominal cadence of 7 days, and had the goal of detecting Type Ia SNe for cosmology. The precise, deep photometry of DES also facilitated the discovery of 22 spectroscopically confirmed SLSNe in a redshift range $0.22 \leq z \leq 1.99$ and absolute magnitude range $-19.57 \geq M_{4000} \geq -22.82$.

In this thesis I study the volumetric rate of SLSNe from DES. I fit multicolour models to the lightcurves of the DES SLSN sample, and simulate $> 10^8$ of these representative SLSN lightcurves over the cosmological volume and time observed by DES. By comparing simulated lightcurves to archival information of DES observing conditions, I quantify the probability of detecting SLSN lightcurves in DES as a function of redshift and time. I thereby characterise the photometric completeness of the DES search for SLSNe.

I devise selection criteria that are informed by the observed properties

of SLSNe and their host galaxy environments. I impose these selection criteria on the DES transient catalogue to recover 30 additional SLSN candidates. Together with the spectroscopic SLSNe, these candidates constitute the largest sample of SLSNe that has yet been constructed.

I use a Monte Carlo simulation to compute the volumetric rate of the total SLSN sample, and find $R_{\rm V} = 190\,^{+26}_{-23}\,({\rm sys}) \pm 52\,({\rm stat})\,{\rm SLSNe\,yr^{-1}\,Gpc^{-3}}$, at a volume weighted mean redshift of $\overline{z} = 0.797$. I conduct the most detailed error analysis relative to previous SLSN volumetric rate measurements. The volumetric rate measurement of this work is consistent with previous results and with the shape of the normalised cosmic star formation history, in support of the idea that SLSNe originate from massive stars.

Finally, I use an unsupervised machine learning approach to search for anomalous SN lightcurves. I apply a stationary wavelet transform and principal component analysis to a sample of 28,184 Gaussian processed lightcurves from the DES catalogue. I visualise similarities between the resulting abstract features using the t-distributed stochastic neighbour embedding algorithm and thereby identify six anomalous lightcurves. By inspecting the host galaxies of these, I suggest that two are peculiar core collapse SNe, two are active galactic nuclei, and two are SLSN candidates. I discuss lessons learned for future such analyses.

Table of Contents

List of Figures

List of Tables

Declaration

Whilst registered as a candidate for the above degree, I have not been registered for any other research award. The results and conclusions embodied in this thesis are the work of the named candidate and have not been submitted for any other academic award.

Word count: 36,228 words.

Acknowledgements

I would like to thank my supervisory team, Bob Nichol and Chris Frohmaier. Without your constructive critique and encouragement this thesis would not have been possible. Bob, thank you for your energy, your vision, and for the opportunity to be part of the Dark Energy Survey collaboration. I am grateful for all that I have learned from you. Chris, thank you for your patience, your focus and for imparting to me many invaluable pieces of your knowledge. Both of you have made me a better scientist.

Thanks to the friends I have made at the ICG. In no intended order; Paul, Ben M., Taniya, Pier, Rob, Marco and Matt H.; Ben B., Matt W., Hedda and Xan; you have all had a lasting impact. Without you to distract me with uncountable trips to the pub I probably would have graduated a long time ago, but without having had so much fun.

Third, thank you to my family. In good and bad times you have always been there, cheering me on. I would especially like to express my gratitude to Lorna, whose post has kept me smiling while I wrote this thesis.

Lastly, I would like to thank Hannah. Your love and support has not wavered throughout my PhD. Thank you for allowing me to become a part of your world, and for becoming a part of this one.

List of Acronyms

AAT . . . . . **A**nglo-**A**ustralian **T**elescope

AGN . . . . . **A**ctive **G**alactic **N**ucleus

BCS . . . . . **B**lue **C**hannel **S**pectrograph

CCD . . . . . **C**harge-**C**oupled **D**evice

CDFS . . . . **C**handra **D**eep **F**ield **S**outh

CFHT . . . . **C**anada **F**range **H**awaii **T**elescope

COS . . . . . **C**osmic **O**rigins **S**pectrograph

CSM . . . . . **C**ircum**S**tellar **M**aterial

CTIO . . . . . **C**erro **T**ololo **I**nter-American **O**bservatory

CWT . . . . . **C**ontinuous **W**avelet **T**ransform

DBSP . . . . **D**ou**B**le **SP**ectrograph

Dec. . . . . . **Dec**lination

DECam . . . **D**ark **E**nergy **Cam**era

DEIMOS . . **DE**ep **I**maging **M**ulti-**O**bject **S**pectrograph

DES . . . . . **D**ark **E**nergy **S**urvey

DES-SN . . . **D**ark **Energy** **S**urvey **S**uper**N**ova Survey

DESDM . . . **D**ark **E**nergy **S**urvey **D**ata **M**anagement System

DLR . . . . . **D**irectional **L**ight **R**adius

d.o.f. . . . . . **d**egrees **o**f **f**reedom

EDS . . . . . **E**uclid **D**eep **S**urvey

ESO . . . . . **E**uropean **S**outhern **O**bservatory

ESSENCE . . **E**quation of **S**tate: **S**up**E**r**N**ovae Trace **C**osmic **E**xpansion

FUV . . . . . **F**ar **U**ltra**V**iolet

HSC . . . . . **H**yper-**S**uprime **C**amera

HST . . . . . **H**ubble **S**pace **T**elescope

GMOS . . . . **G**emini **M**ulti-**O**bject **S**pectrograph

GTC . . . . . **G**ran **T**elescopio **C**anarias

IMACS . . . **I**namori **M**agellan **A**real **C**amera and **S**pectrograph

iPTF . . . . . **i**ntermediate **P**alomar **T**ransient **F**actory

LSST . . . . . **L**arge **S**ynoptic **S**urvey **T**elescope

LDSS . . . . . **L**ow **D**ispersion **S**urvey **S**pectrograph

LRIS . . . . . **L**ow **R**esolution **I**maging **S**pectrograph

LSS . . . . . **L**arge **S**cale **S**tructure

MMT . . . . . **M**ultiple **M**irror **T**elescope

NCSA . . . . **N**ational **C**entre for **S**upercomputing **A**pplications

NOAO . . . . **N**ational **O**ptical **A**stronomy **O**bservatory

NTT . . . . . **N**ew **T**echnologies **T**elescope

NUV . . . . . **N**ear **U**ltra **V**iolet

OSIRIS . . . **O**ptical **S**ystem for **I**maging and Low **R**esolution **I**ntegrated **S**pectroscopy

OzDES . . . . **Aus**tralian **D**ark **E**nergy **S**urvey

Pan-STARRS **Pan**oramic **S**urvey **T**elescope **A**nd **R**apid **R**esponse **S**ystem

PCA . . . . . **P**rincipal **C**omponent **A**nalysis

PISN . . . . . **P**air **I**nstability **S**uper**N**ova

PSF . . . . . **P**oint **S**pread **F**unction

pSNID . . . . **p**hotometric **S**uper**N**ova **ID**entification algorithm

PTF . . . . . **P**alomar **T**ransient **F**actory

P200 . . . . . **P**alomar **200**-inch Hale Telescope

RA . . . . . **R**ight **A**scension

ROTSE . . . **R**obotic **O**ptical **T**ransient **S**earch **E**xperiment

SALT . . . . . **S**outh **A**frican **L**arge **T**elescope

SCP . . . . . **S**upernova **C**osmology **P**roject

SDSS . . . . . **S**loan **D**igital **S**ky **S**urvey

SFH . . . . . **S**tar **F**ormation **H**istory

SIRTF . . . . **S**pace **I**nfra**R**ed **T**elescope **F**acility

SLSN(e) . . . **S**uper**L**uminous **S**uper**N**ova**(e)**

SN(e) . . . . . **S**uper**N**ova**(e)**

SNLS . . . . . **S**uper**N**ova **L**egacy **S**urvey

SNSE . . . . . **S**uper**N**ova **S**ingle **E**poch Pipeline

SOAR . . . . **SO**uthern **A**strophysical **R**esearch Telescope

STIS . . . . . **S**pace **T**elescope **I**maging **S**pectrograph

SQL . . . . . **S**tructured **Q**uery **L**anguage

SWIRE . . . **S**IRTF **W**ide-area **I**nfra**R**ed **E**xtragalactic **S**urvey

SWT . . . . . **S**tationary **W**avelet **T**ransform

TDE . . . . . **T**idal **D**isruption **E**vent

t-SNE . . . . **t-**distributed **S**tochastic **N**eighbour **E**mbedding

USNO . . . . **U**nited **S**tates **N**aval **O**bservatory Catalog

UV . . . . . **U**ltra **V**iolet

VIDEO . . . **VI**STA **D**eep **E**xtragalactic **O**bservations Survey

VISTA . . . . **V**isible and **I**nfrared **S**urvey **T**elescope for **A**stronomy

VLT . . . . . **V**ery **L**arge **T**elescope

XMM . . . . **X**-ray **M**ulti-**M**irror Mission

ZAMS . . . . **Z**ero **A**ge **M**ain **S**equence

ZTF . . . . . **Z**wicky **T**ransient **F**acility

2dF . . . . . **2 d**egree **F**ield

Chapter 1

Introduction

This chapter is intended as a review of the literature. Figures 1.3 and 1.9 are my own. References are given throughout.

The death throes of massive stars are still poorly understood. Despite this, significant progress has been made since the first recorded observation of a 'guest star' by Chinese astronomers in 185 AD[1]. The study of the newly named 'supernovae' (SNe; Baade & Zwicky 1934a) accelerated in the 1930s with the first systematic searches (Zwicky, 1938a). These 'supernova patrols' used the 45cm Schmidt telescope at Palomar Observatory in California to regularly image nearby galaxies. Discovery images were manually compared to legacy images to search for transient light, and thereby identify SNe.

Since then, the yield of SN searches has exponentially increased. With the advent of digital imaging using charge-coupled devices (CCDs), robotic telescopes, software pipelines, and a revolution in survey philosophy to systematically search entire areas of the night sky, astronomers are now discovering more than a thousand SNe each year (Figure 1.1).

The physical understanding of SNe has grown accordingly. Baade &

[1]Other ancient guest stars include those observed in 1006, 1054, 1181, 1572, and 1604 AD (Clark & Stephenson, 1982). These are usually confirmed by the modern association with supernova remnants.

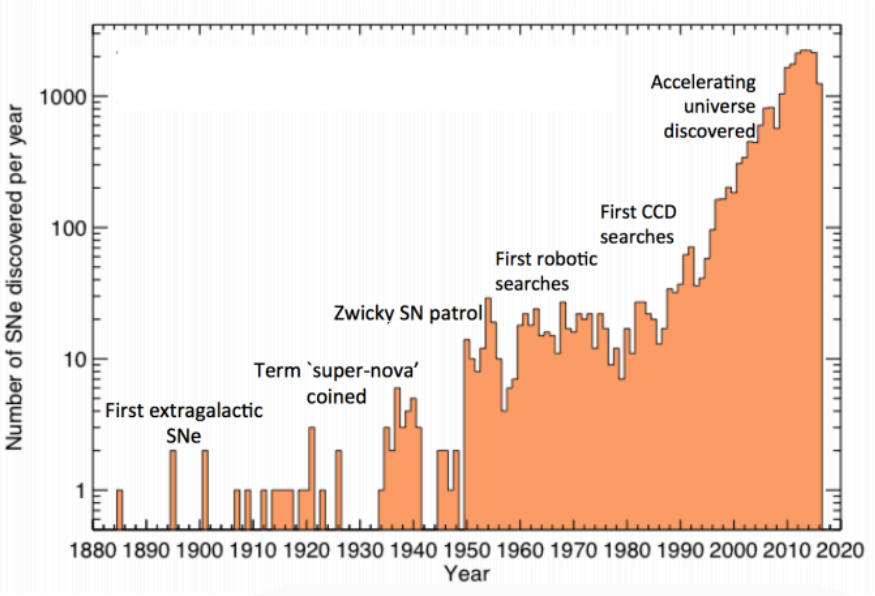

Figure 1.1: The exponential rise in the number of SNe discovered per year. Technological advances have made it possible to observe more SNe than ever before. *Figure credit:* M. Sullivan. *Figure from:* Stritzinger & Moriya (2018).

Zwicky (1934b) originally postulated that these SNe are the collapse of ordinary stars into neutron stars, which emit cosmic rays in the process. Nearly a century later, imaging surveys have precisely measured the variation of the brightness of SNe over time (i.e. their *lightcurves*), while spectroscopic observations have revealed the chemical composition of these events. Both of these techniques have permitted the theoretical modelling of the physical mechanism behind these cataclysmic explosions.

1.1 An Observational Overview of Supernovae

1.1.1 Spectroscopic Classification of Supernovae

Supernovae are initially classified through absorption and emission lines in their optical spectra near maximum light. Minkowski (1941) classified the supernovae which were known at that time into two broad classes - Type II

SNe contain obvious hydrogen lines, while Type I SNe do not. This classification scheme encapsulates nearly all SN explosions that have been observed (Branch & Wheeler, 2017).

Later on, this classification scheme was extended based on additional features which were apparent in the observed spectra of SNe. Type Ia SNe show a strong absorption feature near 6100Å produced by singly ionized silicon (Si II), as well as considerable absorption from iron group elements. The spectra of Type Ib SNe do not exhibit obvious Si II lines (Porter & Filippenko, 1987), but instead features of neutral helium (He I) become apparent near maximum light. Type Ic SNe, on the other hand, show neither conspicuous silicon nor helium absorption lines (Wheeler & Harkness, 1986), but do often show a strong absorption of neutral oxygen (O I) (Branch & Wheeler, 2017). Typical spectra of the basic SN types are shown in Figure 1.2. The history and development of the modern SN classification scheme is reviewed by da Silva (1993).

1.1.2 Photometric Classification of Supernovae

The classification of Type I SNe is largely based on their spectroscopic properties. The two primary classes of Type II SNe on the other hand, reveal the majority of their diversity through the evolution of their lightcurves. All SNe show a basic behaviour in the lightcurve of a rise to maximum light followed by a subsequent decline. It is the nature of this decline through which Type IIP and Type IIL SNe are traditionally classified (Barbon et al., 1979). Type IIP SNe show a short decline after maximum light, followed by a plateau in the lightcurve in which the flux remains constant for up to 3 months. Type IIL SNe on the other hand, show a decline after peak that is approximately linear in magnitudes, and is consistent with the half life (77 rest frame days) of ^{56}Co (Nadyozhin, 1994). More recently, some authors have argued that Type IIL and Type IIP SNe form extremities of a continuum, and should not be considered separate classes (Anderson et al., 2014; Holoien et al., 2016).

Some subtypes of Type II SNe are classified through their spectral lines.

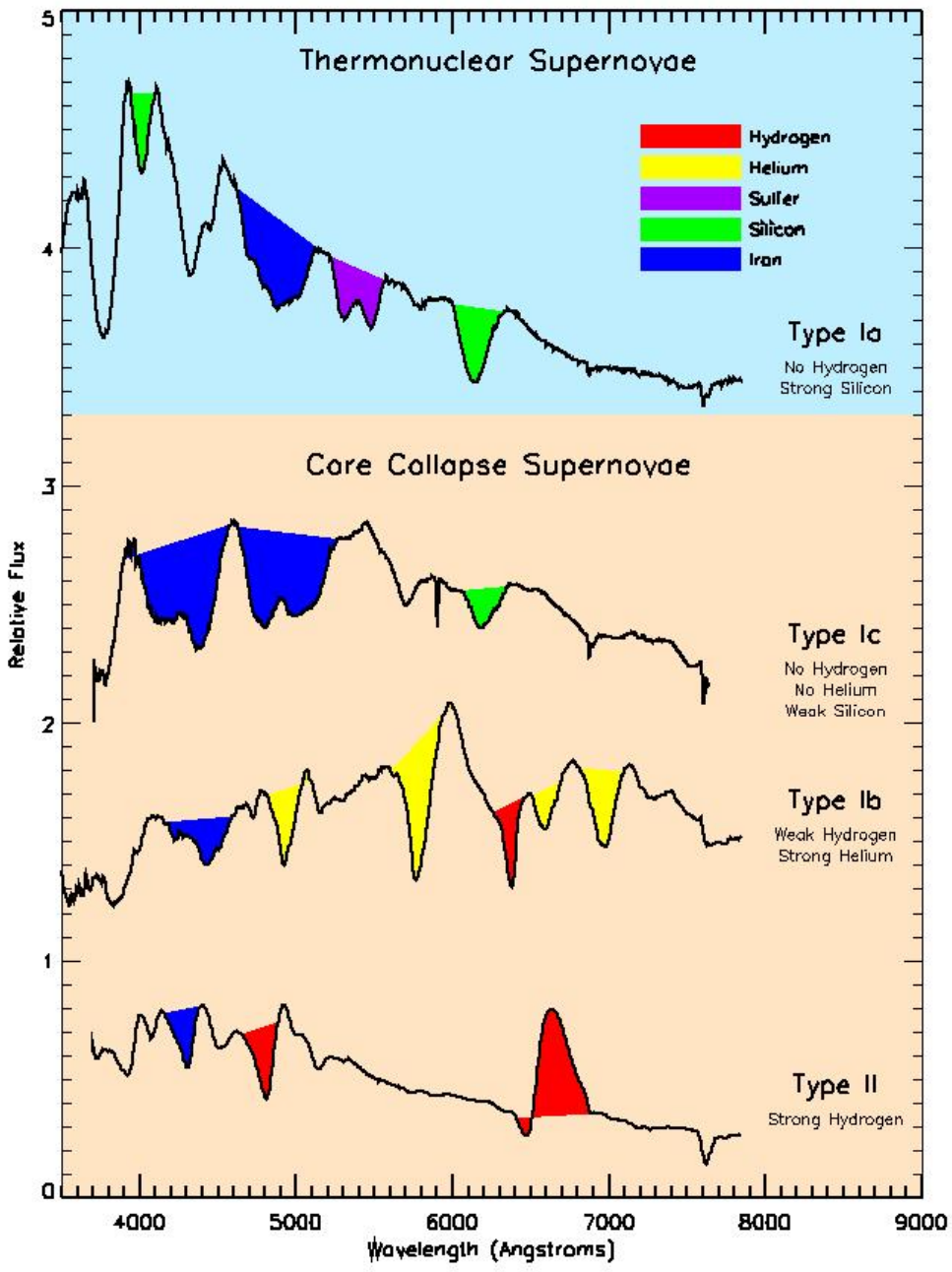

Figure 1.2: Comparison of typical early-time spectra of the traditional types of supernovae. The lines used for classification are marked in colour. *Figure credit:* D. Kasen.

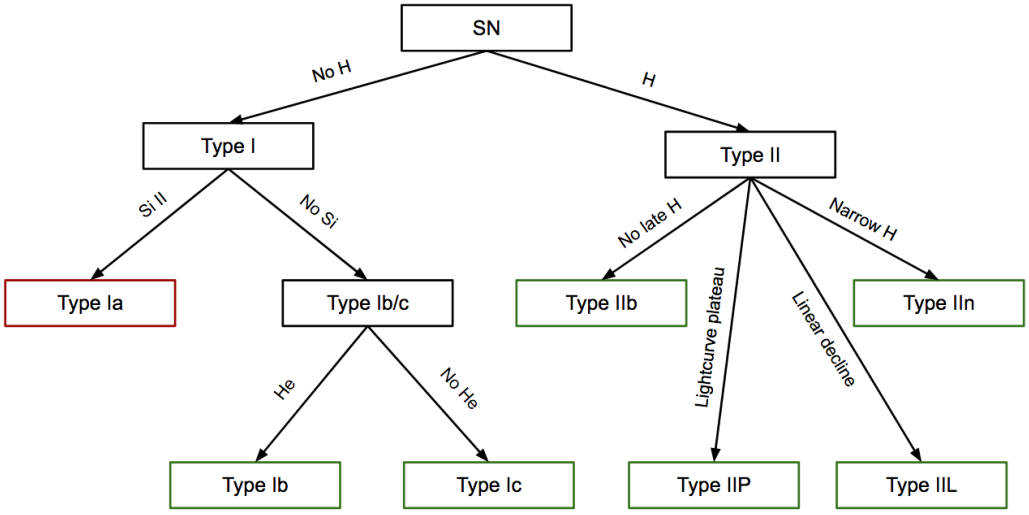

Figure 1.3: A simplified schematic showing the classification of SNe. SN classes in red show thermonuclear explosions, while classes in green show core collapse SNe.

Type IIn SNe show narrow lines of Hα in their spectra, indicating that the emitting/absorbing material is moving at a slow velocity, and interpreted as an indication of the interaction of a fast-moving ejecta with slow-moving circumstellar material (CSM; Schlegel 1990). Type IIb SNe show weak hydrogen in their early spectra, and are thus classified as Type II. Unlike other Type II SNe, the hydrogen lines soon fade, and the Type IIb spectrum begins to show He lines, resembling the spectra of Type Ib SNe (Filippenko, 1988). A schematic of the classification of SNe is shown in Figure 1.3.

1.2 A Theoretical Overview of Supernovae

Alongside the observational classification of the various SN types, significant progress has been made on the theoretical understanding and simulation of the underlying physics which produces these brilliant explosions. From a theoretical perspective, there are two mechanisms which power the standard SN types: the collapse of a massive stellar core, and the thermonuclear explosion

of a white dwarf. A recent review of the physics of core collapse SNe is given by Couch (2017). Meanwhile, a review of the physics of thermonuclear SNe is given by Wang & Han (2012).

1.2.1 Core Collapse Supernovae

As a massive star reaches the end of its main sequence lifetime, the supply of hydrogen in its core is depleted, and the thermal pressure decreases. The star begins to contract under gravity. This increases the temperature at the core, and, if the star is of high enough mass, the gravitational potential energy of the in-falling mass is liberated through the ignition of helium fusion. The helium burning phase of the star is far shorter than its main sequence hydrogen burning phase; there is a smaller supply of helium. Once the helium is expended, the process iterates, and if the star is of a zero age main sequence (ZAMS) mass $\geq 8M_{\odot}$, carbon burning will ignite.

The lighter elements form shells around the core, increasing in atomic number towards the centre of the star in an onion-like structure. Iron has the highest binding energy per nucleon, and thus energy cannot be liberated by the fusion of Fe into heavier elements. It is somewhat ironic that the intrinsic stability of iron causes the total disruption of the star. Without the fusion of any element in the core, the supporting pressure is gone, and the core begins to collapse. The contraction of the massive core is not slowed by electron degeneracy pressure, and it eventually reaches a temperature of $\sim 10^{10}$ K (Janka, 2012). The temperature of this iron core causes it to radiate high energy gamma rays and undergo photodisintegration, in which heavy nuclei absorb energy from gamma rays to disintegrate into lighter nuclei. The dominant nuclear processes are:

$$^{56}\mathrm{Fe} + \gamma \rightarrow 13\,^{4}\mathrm{He} + 4n \tag{1.1}$$

$$^{4}He + \gamma \rightarrow 2p^{+} + 2n. \tag{1.2}$$

This photodisintegration requires a large energy input from the core, which reduces the outward pressure and thereby accelerates the collapse.

The core has already passed the density corresponding to electron degeneracy ($\sim 10^9$ g cm^{-3}; Janka 2012), and as the core continues to collapse free electrons are captured by protons to form neutrons, releasing electron neutrinos:

$$p^+ + e^- \rightarrow n + \nu_e. \tag{1.3}$$

It is the escape of these neutrinos that removes the majority of energy from the free-falling core.

Once the density of the core reaches nuclear density, the strong nuclear force becomes repulsive and the core instantaneously becomes incompressible. The outer layers of the core fall inwards toward this inert proto-neutron star and rebound off the strong nuclear potential, forming an outgoing shock front.

This shock wave propagates outwards through the star, aided by the huge density of outward streaming neutrinos. Neutrinos usually interact very weakly with matter, but under the extreme densities produced from core collapse 0.1% are trapped behind the shock wave, further accelerating it outward (Bethe & Wilson, 1985). As this shock wave propagates through the collapsing outer material it sweeps it up, compressing and heating it. This shock wave catalyses a whole new stage of nucleosynthesis in which large quantities of elements heavier than iron are born, including the radioactive ^{56}Fe, ^{56}Co, and ^{56}Ni.

The initially increasing brightness of the observed lightcurve is powered by the increasing surface area of the expanding photosphere, as the emitted flux is a function of the surface area of the photosphere. Once the ejecta becomes optically thin due to expansion, the photosphere begins to recede deeper into the stellar envelope, and its surface area decreases. Additional energy input in the late-time lightcurve decline is powered by the decaying products of the synthesized Ni^{56}. Lyman et al. (2016) give comparisons of the amount of Ni^{56} that is synthesized in different subtypes of core collapse SNe, along with other explosion parameters.

Circumstellar interaction

As the SN shockwave continues to propagate outwards, it may or may not encounter material which has been shed by the progenitor star prior to explosion (Chevalier & Fransson, 2003). In the case of Type IIP SNe, the outer H-rich envelope is retained up to explosion, and the shockwave propagates through this envelope, ionizing the hydrogen. Ionized hydrogen is opaque to optical light, but as the envelope expands and cools, the hydrogen recombines and becomes transparent. As the envelope cools to recombination temperature (4000-6000K) at smaller radii from the core, the photosphere recedes deeper into the star. The recombination of ionized hydrogen and free electrons in the SN ejecta produces the nearly-constant flux in the plateau of the lightcurve of Type IIP SNe.

Type I supernovae are so categorized due to the lack of spectroscopic hydrogen lines. In the case of Type Ib and Ic SNe, this could be due to the stripping of the H-rich envelope around the progenitor star due to either stellar winds (Heger et al., 1997; Puls et al., 2008), episodic ejection (Smith & Owocki, 2006; Pastorello et al., 2007; Shiode & Quataert, 2014), or binary interaction (Taam & Sandquist, 2000). The exact mass loss mechanism is still not understood, and is reviewed by Smith (2014). SNe Ib differ from SNe Ic in that they show neutral helium lines (He I) in their spectra. The presence (or absence) of helium in the spectra of these SNe indicates the degree to which the outer envelopes of light elements have been 'stripped' prior to core collapse.

Late time Hα lines have been observed in the spectra of mutiple Type I SNe (Vinko et al., 2017). As the SN ejecta continues to expand, eventually it may collide with previously shed envelope matter. This results in an excitation of the latent hydrogen, and subsequent emission of Hα flux. The variability in the late time Hα flux can inform observers to the mass loss history of the progenitor star, as the Hα flux variability over time probes the density of the CSM through which the ejecta propagates.

1.2.2 Thermonuclear Supernovae

Following the fusion of hydrogen and helium, stars with a ZAMS mass $M_{\rm ZAMS} < 8M_{\odot}$ do not have the core temperature necessary to fuse carbon, and instead form an inert core of carbon and oxygen supported by electron degeneracy pressure. This quantum pressure can support a mass of no more than $1.44M_{\odot}$, which is known as the Chandrasekhar limit (Chandrasekhar, 1931, 1984; Lieb & Yau, 1987). There are at least two potential channels through which these so-called "white dwarfs" can continue to accrue mass after formation.

Firstly, if a white dwarf is in a binary system with a main sequence or red giant star, the outer envelope of the companion may expand past the limits of its Roche lobes, and thereby transfer mass to the gravitational potential of the white dwarf (Whelan & Iben, 1973). In this case, the white dwarf will accrete mass from its companion onto its surface, and can thereby approach the Chandrasekhar limit. This channel is known as the single degenerate scenario.

Secondly, if a white dwarf is in a binary system with another white dwarf, this system can lose rotational energy through the emission of gravitational waves, causing the inspiral of the system (Iben & Tutukov, 1984). For two white dwarfs of significantly different mass, the lower mass companion will tidally disrupt and then accrete onto the surface of the higher mass companion. This channel is known as the double degenerate scenario[2] (Webbink, 1984).

As a white dwarf approaches the Chandrasekhar limit, electron degeneracy pressure is overcome by the gravitational potential, and the matter density in the core shoots up, igniting the carbon-oxygen core in a thermonuclear explosion. The low binding energy CO is fused into higher binding energy species, especially ^{56}Ni. The energy released in this transition is enough to

[2]There is also evidence that the inspiral can result in a direct collision of the two white dwarfs (e.g. Röpke et al. 2012; Pakmor et al. 2013). In this case, if the total mass of the system is $> 1.44M_{\odot}$, the explosion may be super-Chandrasekhar.

disrupt the star (Hillebrandt & Niemeyer, 2000).

Type Ia SNe are perhaps the most famous of all SN types, due to their use as standardizable candles and thus as cosmological distance probes (see e.g. Betoule et al. 2014; Scolnic et al. 2018; Abbott et al. 2019 for recent results). In the late 90s the High-Z Supernova Search Team (Schmidt et al., 1998) and the Supernova Cosmology Project (Perlmutter et al., 1999) used SNe Ia to show that the expansion of the Universe is accelerating. The cause of this acceleration is unknown, and is most popularly referred to as dark energy. The nature of dark energy remains one of the most important questions in cosmology today. The discovery of the accelerated expansion of the Universe has since been verified by a cornucopia of independent measurements including baryon acoustic oscillations (Alam et al., 2017; Carter et al., 2018), cosmic microwave background measurements (e.g. Planck Collaboration et al., 2018), weak gravitational lensing and galaxy cluster measurements (e.g. Abbott et al., 2018a), strong gravitational lensing (Bonvin et al., 2017), and recently the use of gravitational wave sources, or kilonovae, as standard sirens (Abbott et al., 2017).

1.3 Superluminous Supernovae

In recent years, a new class of extremely bright and long-lasting supernova has emerged. The first member of this class (SN 2005ap; Quimby et al., 2007) was discovered in 2005 as part of the Texas Supernova Search (Quimby, 2006). This discovery was soon followed with observations of the very luminous SN 2006gy (Smith et al., 2007) and SN 2007bi (Young et al., 2010), indicating the presence of a hitherto undiscovered class of SN.

This new class has been termed superluminous supernovae (SLSNe) due to their extreme energy output (10^{51} erg); SLSNe shine with luminosities ~ 100 times as bright as core collapse SNe at peak, and last as long as 3 months in the rest frame. SLSNe were originally defined by an arbitrary peak absolute magnitude cutoff of $M \leq -21$ (Gal-Yam, 2012), although many

fainter transients exhibiting similar spectroscopic and photometric behaviour have since been observed (e.g. De Cia et al., 2018; Lunnan et al., 2018; Angus et al., 2019). As a result, SLSNe are now classified based on their spectrophotometric evolution.

As with traditional SN types, SLSNe are subdivided into two basic populations. Type II SLSNe (SLSNe-II) exhibit conspicuous hydrogen lines in their spectra, while Type I SLSNe (SLSNe-I) do not. SLSNe-I are the more well studied of the two classes, partly owing to the difficulty in producing theoretical models that represent the observed photometry well, and partly owing to their more frequent occurrence. Similarly to the more common core collapse SN events, a large degree of diversity exists within each of the superluminous classes. Both SLSNe-I and SLSNe-II exhibit a wide range of peak luminosities and duration. For example, Angus et al. (2019) found an intrinsic luminosity distribution for SLSNe-I of $-19.57 \leq M_{4000} \leq -22.82$, where M_{4000} is the peak absolute magnitude in a synthetic passband defined by Inserra & Smartt (2014).

SLSNe-I are spectroscopically classified by the presence of a 'W'-shaped feature around 4000Å, attributed to singly ionized oxygen (OII). Typical spectra of SLSNe-I around maximum light are shown in Figure 1.4. At late times, SLSN-I spectra evolve to closely resemble the spectra of SN Ic around maximum light, and for this reason they are sometimes referred to as SLSN Ic in the literature.

In addition, there is tentative evidence for some bimodality in the distribution of the rise and decline times of SLSN-I, with a small fraction evolving more slowly (e.g. Nicholl et al., 2015). These are sometimes called slow-evolving SLSNe-I in the literature. However, the majority of SLSNe-I are of the fast-evolving subtype. Meanwhile, SLSNe-II are further sub-classified based on the width of the observed Hα line in their spectra. SLSNe-IIn have a narrow Hα line, a strong indication of interaction with slow moving circumstellar material, while SLSNe-II show broader hydrogen emission.

SLSNe remained undiscovered long after the fainter classes of transient

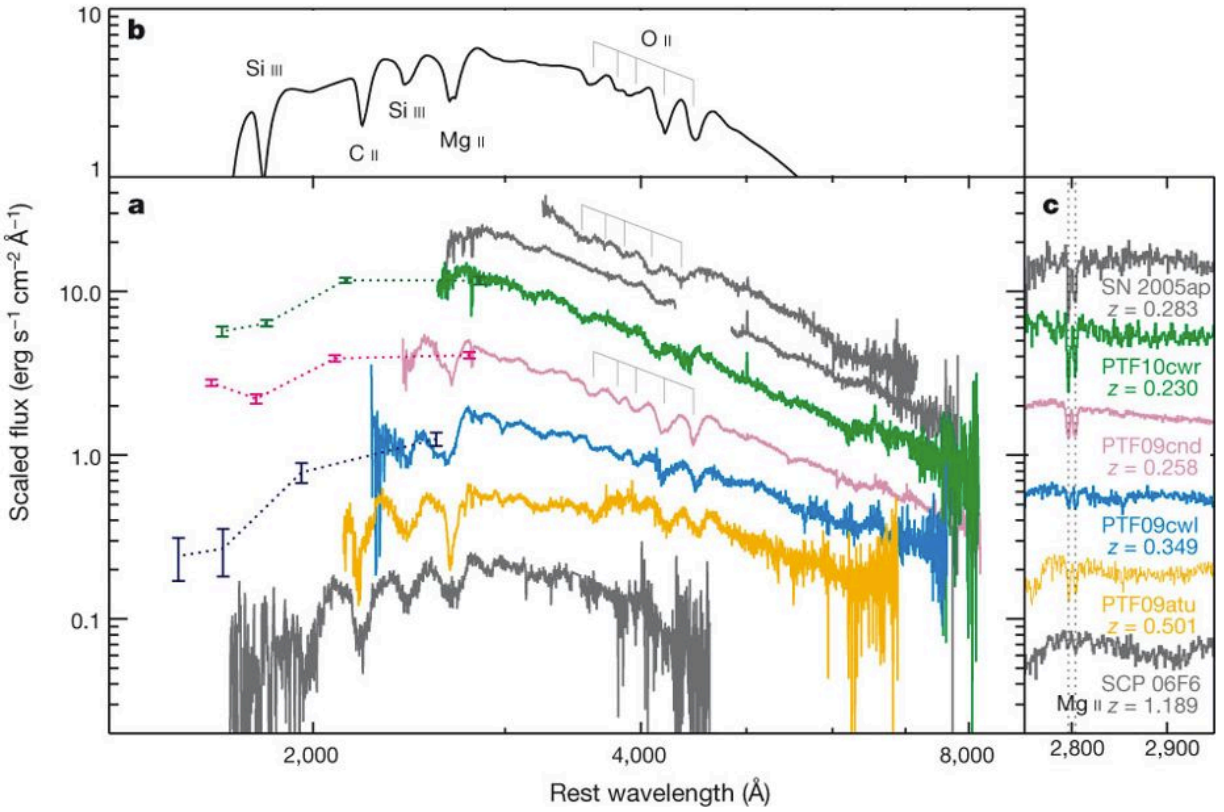

Figure 1.4: Observed spectra of typical SLSNe-I. The central panel shows the observed spectra of 6 different SLSNe-I, which exhibit a blue continuum with prominent broad absorption lines. The top panel shows a synthetic spectrum that suggests the absorption comb around 4000Å originates from O II, which now defines the spectra of SLSNe-I (e.g. Mazzali et al. 2016; Quimby et al. 2018). Significant absorption from Si III, Mg II and C II is present blueward of 3000Å. The right panel shows the determination of the redshifts using narrow Mg II doublets. *Figure credit:* Quimby et al. (2011).

were observed for two reasons. Firstly, they have a strong preference to explode in faint galaxies (specifically star forming, low metallicity dwarf galaxies, Lunnan et al. 2014; Angus et al. 2016; Schulze et al. 2018). The recent rise of untargeted, high cadence and deep astronomical surveys which periodically scan large areas of the sky have serendipitously observed these faint galaxies, whereas previously much brighter galaxies were targeted. Secondly, SLSNe are exceedingly rare, with early studies into the local volumetric rate showing that they form just 0.01% of the total SN population (Quimby et al., 2013; McCrum et al., 2015; Prajs et al., 2017).

1.3.1 Superluminous Supernovae as Cosmological Probes

SLSNe exhibit an exceptionally blue colour, with the majority of their flux emitted in the rest frame ultraviolet (UV) bands. Together with their bright lightcurves, this makes them attractive as cosmological probes, as the bright UV flux will be redshifted into the optical bands at cosmological distances.

Despite the intrinsic diversity in the SLSN class, there may exist a subset of fast-evolving SLSNe-I which can be standardised using an analogous technique to that used for Type Ia SNe (e.g. Guy et al., 2005, 2007). Inserra & Smartt (2014) found an uncorrected intrinsic scatter in the peak magnitudes of SLSNe-I of 0.47 mag. By correlation of the peak magnitude to the decline rate after 30 (rest frame) days from peak, this scatter was reduced to 0.25 mag, demonstrating that brighter events decline more slowly. The authors conclude that SLSNe-I show potential as distance indicators in the high redshift Universe, and with larger samples they may be used to probe the expansion history of the Universe to much higher redshift ($z > 2$) than with SNe Ia ($z \lesssim 1.2$).

While these empirical correlations seem encouraging, the progenitors of both SLSNe-I and SLSNe-II are still under debate. The spectra of SLSNe-IIn show clear evidence for interaction with slowly moving circumstellar material. The progenitors of SLSNe-I and SLSNe-II, on the other hand, remain poorly understood. A wide range of models have been proposed, and in the

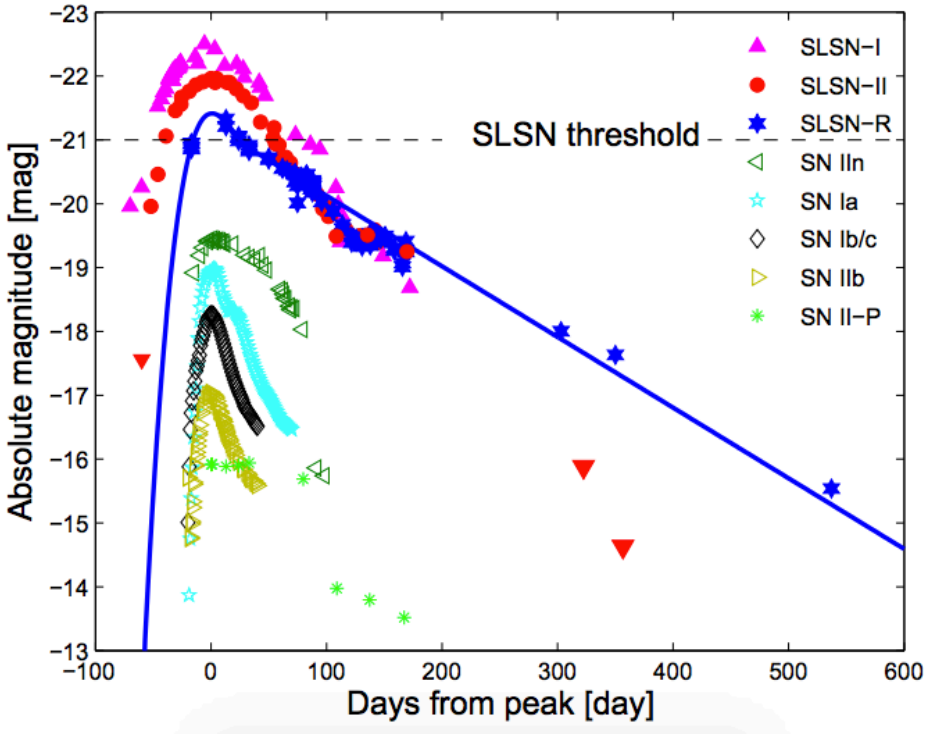

Figure 1.5: Comparison of typical SLSN lightcurves to ordinary SN types. SLSNe are up to 100 times brighter than core collapse events, and show a much longer duration. The arbitrary SLSN magnitude threshold shown here has since been transgressed (although a fainter threshold has been suggested; Gal-Yam 2018), and the class 'SLSN-R' has since been subsumed into SLSN-I. Figure taken from Gal-Yam (2012).

next section I delve into the details of the competing progenitor models to elucidate the astrophysics behind these extraordinary explosions.

1.3.2 Superluminous Supernova Progenitor Models

While the explosion physics of normal SN types, such as core collapse and thermonuclear supernovae, are relatively well understood (although there are still many active areas of research), our understanding of the underlying physics of SLSNe has not had nearly as long to mature. Traditional

lightcurve models for core collapse and thermonuclear models rely on the synthesis and subsequent decay of radioactive species, particularly ^{56}Ni. Attempts to explain SLSN lightcurves with analogous models have shown that the amount of radioactive isotopes which would have to be synthesized in the explosion constitutes too great a fraction of the total ejecta mass to be physical. A plethora of alternative explosion mechanisms to reproduce the lightcurves and spectra of SLSNe have been suggested since their discovery. These progenitor models are broadly separable into three distinct categories.

Pair Instability Supernovae

In very high mass stars which have undergone central helium burning and formed oxygen cores of mass from 60 to 130 $M_{\odot}$[3], the nature of the pre-explosion evolution is expected to differ from that of ordinary core collapse SNe. In conditions with a temperature $T \gtrsim 10^9$ K and $\rho \lesssim 10^5 \mathrm{g\,cm^{-3}}$ (Branch & Wheeler, 2017), gamma rays created in fusion reactions reach an energy greater than the rest mass of the electron, and can spontaneously produce electron-positron pairs,

$$\gamma + \gamma \leftrightarrow e^- + e^+.$$

A small fraction of the electron-positron pairs are predicted to annihilate, producing neutrino-antineutrino pairs, which subsequently stream out of the star, stripping energy from the core and reducing the internal pressure. This causes the star to contract further, raising the temperature and thus increasing the rate of pair production. As this unstable feedback develops, the temperature reaches $\sim 3 \times 10^9$ K, and the oxygen in the core is energised to such a degree that it explosively fuses into iron, completely disrupting the star. This explosion is known as a pair instability supernova (PISN).

This process is predicted to produce tens of solar masses of the radioactive ^{56}Ni, the decay of which can power very bright explosions. The PISN model

[3]The corresponding ZAMS masses depend upon the metallicity and rotation of the star.

predicts an exceptionally slow rise to peak brightness, on the order of 50-100 (rest frame) days. The few percent of SLSN-I lightcurves which are termed slow-evolving SLSNe-I have declines which are consistent with the decay of ^{56}Co, and the PISN model could be a feasible explanation of these observations. However, the long rise time that the PISN model predicts is largely inconsistent with both fast- and slow-evolving SLSN-I lightcurves (Nicholl et al., 2013).

Circumstellar Interaction

The extreme explosion energies of Type IIn SLSNe are usually attributed to the collision of the explosion ejecta with previously shed circumstellar material. In particular, the presence of narrow Hα lines indicates slow-moving H-rich material, and is interpreted as the collision of a fast moving ejecta with previously shed H-rich circumstellar material (Quimby, 2006; Chatzopoulos et al., 2012).

The photometric data for many SLSN IIn candidates are consistent with a photosphere of radius $\sim 10^{15}$cm, similar to normal SN II. However, the temperatures inferred from the data are around 12,000K, significantly hotter than normal SN types. The luminosity of SLSNe IIn is directly attributable to the temperature. While the SNe II must expand to the common radius, losing energy adiabatically, SLSNe IIn already have a significant amount of material at this radius, and so a much greater fraction of the kinetic energy of the ejecta is converted to radiation (Branch & Wheeler, 2017).

In a recent analysis of SLSNe-II (Inserra et al., 2018a), little evidence was found for circumstellar interaction at early times, and the authors favoured multiple energy sources. Even if the observed lightcurves of SLSNe-II are powered by circumstellar interaction, the underlying explosion mechanism is nonetheless masked by this effect. Further work is needed to build confidence in both the energy source and explosion mechanism behind SLSNe-II.

The circumstellar interaction model may also be applicable to SLSNe-I. In this case, both the ejecta and the CSM must be free from hydrogen.

One way to achieve this is through the pulsational pair instability model (Woosley et al., 2007; Chatzopoulos & Wheeler, 2012). In this model, the oxygen rich core of a massive star ($M_{\rm ZAMS} \sim 95-130\,{\rm M}_{\odot}$) encounters the pair instability described above, but the energy released by the sudden ignition of carbon and oxygen fusion is not sufficient to entirely disrupt the star. Instead, many solar masses are ejected from the outer layer of the star by the sudden increase in radiation pressure, and the star cools and re-stabilises. This process may iterate several times, resulting in several shells of H-poor material surrounding the oxygen core, the subsequent collision of which can produce bright lightcurves.

Central Engine Models

The most popular mechanism to power the extreme luminosities of SLSNe-I from the literature is the spin down of a rapidly rotating ($P \sim 1$ ms) and highly magnetised ($B \sim 10^{14}$ G)[4] neutron star, otherwise known as a magnetar (Kasen & Bildsten, 2010; Woosley, 2010). Magnetars are thought to originate from the core collapse of the rotating iron cores of fairly massive stars ($M_{\rm ZAMS} \sim 30 - 40\,{\rm M}_{\odot}$). As the rotating core collapses, angular momentum is conserved, and the result is a very rapidly spinning magnetar. In the early stages of the SN, the magnetar is located at the centre of a dense envelope of material, and the two interact via the strong magnetic field. A corresponding electric field is induced in the envelope, which in turn produces a second magnetic field in opposition to the first. These opposing magnetic fields act as a brake to the rapid spin of the magnetar, and the large rotational energy of the magnetar is converted into X-rays and γ-rays. This high energy radiation propagates outwards and collides with the supernova ejecta, heating it up and providing the additional energy source. Magnetars have been observed in our own Galaxy (Kaspi & Beloborodov,

[4]This magnetic field strength is around a billion times as strong as that of the Large Hadron Collider. If the magnetar model is the correct model for SLSNe-I, this may indicate the presence of exotic particle physics.

2017), although these showed longer spin periods than required for modelling SLSNe-I. However, this does not rule out the existence of more rapidly rotating extragalactic magnetars. A schematic showing the structure of a magnetar-powered SLSN-I in the nebular phase is shown in Figure 1.6.

Inserra et al. (2013) showed that the spin down of a rapidly rotating magnetar can reproduce the quasi-bolometric luminosity of a subset of the observed SLSNe-I. In particular, the relatively slow energy deposition into the SN ejecta predicted by the magnetar model is able to reproduce the SLSN-I lightcurve decline, where other models had under-represented the late time flux.

However, other SLSNe-I have been observed whose lightcurves the magnetar model cannot reproduce. For example, Angus et al. (2019) showed that for the 22 SLSNe observed by the Dark Energy Survey (DES), the magnetar model could only reproduce the quasi-bolometric flux in 14 of the cases, and many of the SLSNe showed small scale flux variations that are not captured by the magnetar model, but may indicate some contribution from circumstellar interaction. Additionally, Bhirombhakdi et al. (2018) showed that while the quasi-bolometric lightcurve of the nearby SLSN-I SN2015bn is fit well by a magnetar model, 95% of the total energy emission in the model lies outside of the ultraviolet, optical, and infrared (UVOIR) bands that inform the fit. The authors use observations taken with the XMM-Newton satellite (Jansen et al., 2001) to constrain the X-ray emission of SN2015bn to $< 1.5\%$ of the total flux across all wavelengths predicted by the model, finding no direct evidence of a central engine, and raising the question of the missing emitted energy in this, and perhaps other, SLSNe-I if they are indeed powered by magnetars.

When the cores of very high ZAMS mass stars collapse, the production of black holes is expected, offering another possibility for central engine models to power SLSN-I lightcurves (Dexter & Kasen, 2013). Following core collapse, the fallback accretion model predicts that some of the matter remains gravitationally bound to the central black hole, and reverses its outward tra-

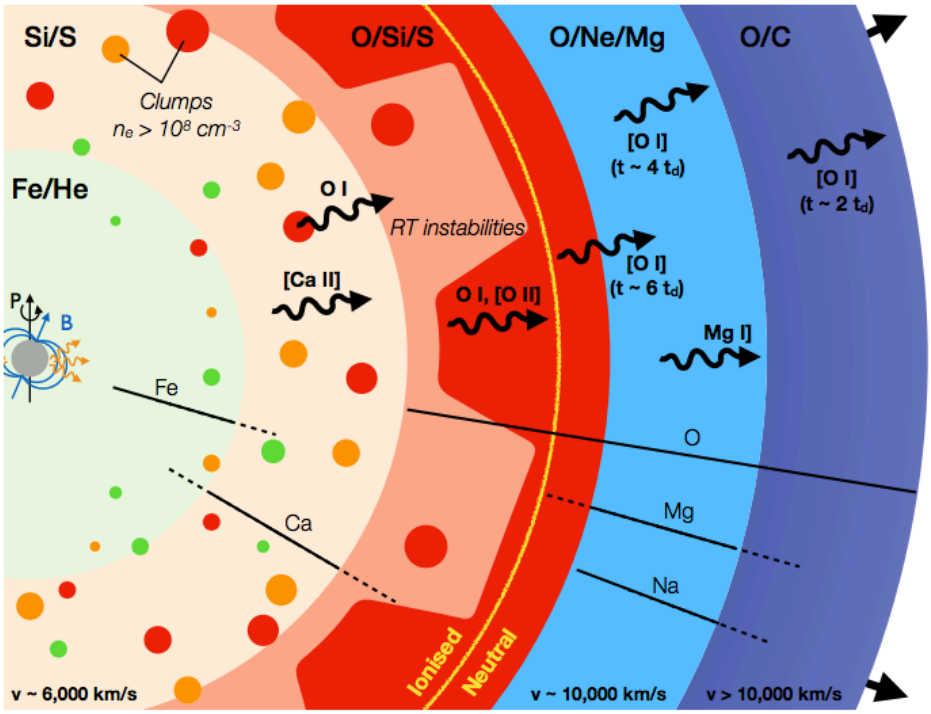

Figure 1.6: The structure of a magnetar-powered SLSN-I in the nebular phase. Zones which produce key spectral lines in the observed spectra of SLSNe-I are labelled. The spin-down of the central magnetar drives hard radiation into the ejecta, heating it and producing the additional energy source required for SLSN-I lightcurves. *Figure credit:* Nicholl et al. (2019).

jectory to fall back onto the black hole and form an accretion disk. The energy liberated in the accretion of this matter onto the black hole can significantly alter the lightcurve of a core collapse SN and potentially produce SLSN-I lightcurves, although this requires the black hole to release emission on a sufficiently long time scale to match the SLSN-I photometry.

It is clear that more work is required to understand the progenitors of both SLSNe-I and SLSNe-II. In the case of standard SN types, progress has been made by studies that investigated the rate of SN explosions, either as a function of the host galaxy properties, or as a function of cosmological redshift. Comparison of these rate results with the expected population of predicted progenitors in the various environments can yield constraints on the progenitor systems. This thesis is primarily concerned with the volumetric rate of SLSNe-I, and in the next section I review the state of supernova rate measurements to date.

1.4 Rates of Supernovae

1.4.1 Rates as a Function of Galaxy Properties

The classical method to calculate the rates of supernovae was invented by Zwicky (1938b, 1942), and later refined by van den Bergh & Tammann (1991). In the traditional SN search paradigm, promising local galaxies are targeted and subsequently revisited after some duration to check whether a SN has exploded. For each host galaxy observation in the search, the time for which a given SN is brighter than the limiting depth of the observation is calculated, and the sum of these times is known as the 'control time'. The control time is thus the total time for which the SN would have been bright enough to have been discovered in all observations of the host galaxy. The supernova rate is then,

$$R_{\rm SN} = N_{\rm SN} \, (\sum_{i=1}^{N_{\rm G}} \tau_i)^{-1}, \tag{1.4}$$

where $N_{\rm SN}$ is the number of supernovae observed, $N_{\rm G}$ is the number of galaxies observed, and $\tau_{\rm i}$ is the control time (in years) for the ith galaxy. The rate $R_{\rm SN}$ is traditionally calculated as a function of the host galaxy brightness, and $R_{\rm SN}$ is expressed in 'supernova units', or SNu, in a particular photometric band. For example $1\,\mathrm{SNuB} = 1\,\mathrm{SN}\,(100\mathrm{yr})^{-1}\,(10^{10}\mathrm{L}_{\odot}^{B})^{-1}$ where $\mathrm{L}_{\odot}^{B}$ is the Bessell B band solar luminosity.

Li et al. (2011) used a refined version of the control time method to measure the rate of the standard SN types against the Hubble type of SN host galaxies (Figure 1.7). From this figure, it can be seen that the Type Ia SN rate is not strongly dependent on the Hubble type of the host, (i.e. SNe Ia explode in any type of galaxy). However, the core collapse Type Ib/c and Type II SNe show a strong preference to explode in late type galaxies. Late type galaxies host younger stellar populations, with significant star formation, and this result is strong evidence that core collapse SNe originate from massive stars, while the thermonuclear Type Ia SNe do not.

1.4.2 Rates as a Function of Redshift

In the cosmological past, the overall metallicity of the universe was lower, while the mean star formation rate was higher. Therefore, studies of SN rates as a function of redshift are expected to inform not only the nature of the progenitors of these events, but also to potentially probe the cosmic star formation history (SFH), particularly through the study of core collapse SN rates. These types of rate measurements typically probe some cosmological volume determined by the survey parameters, and are known as volumetric rate measurements.

SNe inhabiting the Hubble flow ($z \gtrsim 0.1$) are usually observed by untargeted and deep astronomical surveys, almost invariably with the objective of constructing Type Ia SN samples to use as standardized candles to constrain the cosmological expansion history. As a byproduct of these searches, SNe of other types are also observed, enabling the study of not just Type Ia SN volumetric rates, but also of the volumetric rate of core collapse and

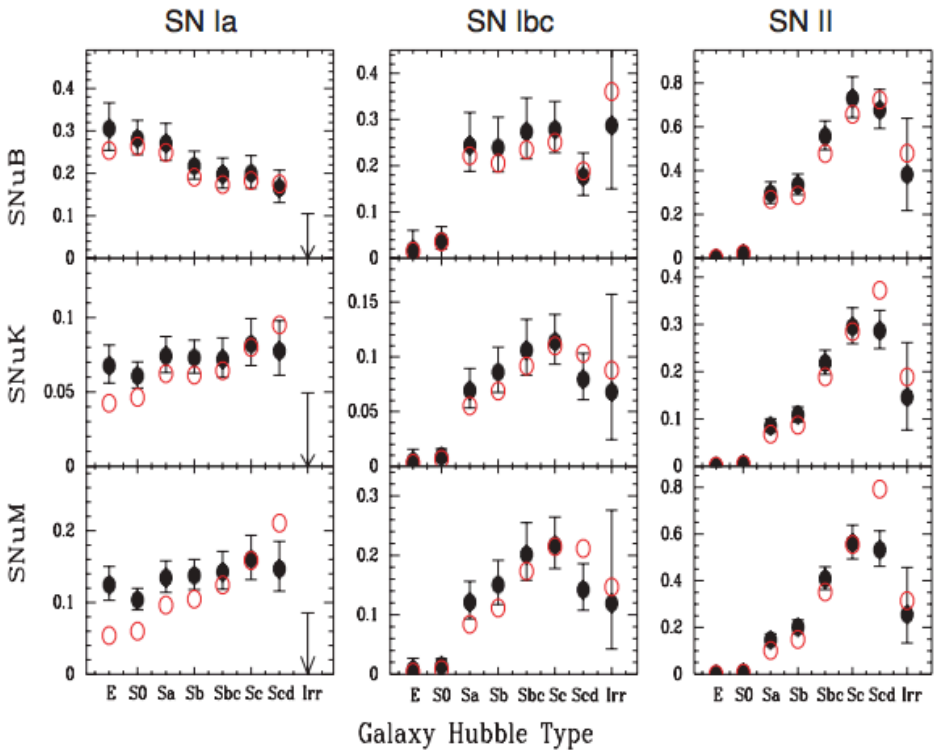

Figure 1.7: The rate of standard SN types as a function of host galaxy Hubble type. Type Ia SNe show a flat distribution with Hubble type, while core collapse SNe tend to explode in late type galaxies. Solid points are calculated using a fiducial galaxy size, while empty points are calculated using a median galaxy size for each Hubble type. *Figure credit:* Li et al. (2011).

superluminous SNe.

The measurement of volumetric rates is renowned within the SN community to be a difficult task, largely due to an often ill-defined completeness in the SN sample. SNe that lie within the observed volume of a survey may go undetected for a plethora of reasons including, but not limited to, pauses in the temporal sampling of the SN fields due to observational scheduling or bad weather, and gaps in the spatial sampling of the SN fields due to gaps between CCDs and dead CCDs.

Volumetric rate studies require a rigorous understanding of the completeness of the SN sample which they use if they are to measure the true rate of the underlying SN population. This completeness is parameterised by the *detection efficiency*. Put simply, the detection efficiency is the the fraction of the underlying SN population which the survey detected. In spectroscopic SN surveys the detection efficiency is a product of two parts - the photometric efficiency and the spectroscopic efficiency. The photometric efficiency is the fraction of the underlying population for which photometry of sufficient quality for further analysis was obtained. The spectroscopic efficiency is the fraction of the photometric sample for which spectra of sufficient quality for classification were obtained.

The volumetric rate of a given SN type in a cosmological volume V is (e.g. Perrett et al. 2010),

$$R_V = \frac{1}{V\Delta T}\sum_{i}^{N}\frac{1+z_i}{\epsilon_i}, \tag{1.5}$$

where ΔT is the time for which the SNe are detectable by the survey, N is the number of SNe detected, z_i is the redshift of the ith SN, and ϵ_i is the efficiency of detecting the ith SN.

As shown in Figure 1.8, the volumetric rate of core collapse SNe closely follows the cosmic star formation history, as expected if the progenitors of these explosions are indeed short lived massive stars. The volumetric rate of SNe Ia (e.g. Dilday et al., 2010; Perrett et al., 2012; Frohmaier et al., 2019), on the other hand, rises less steeply with redshift than does the cosmic SFH,

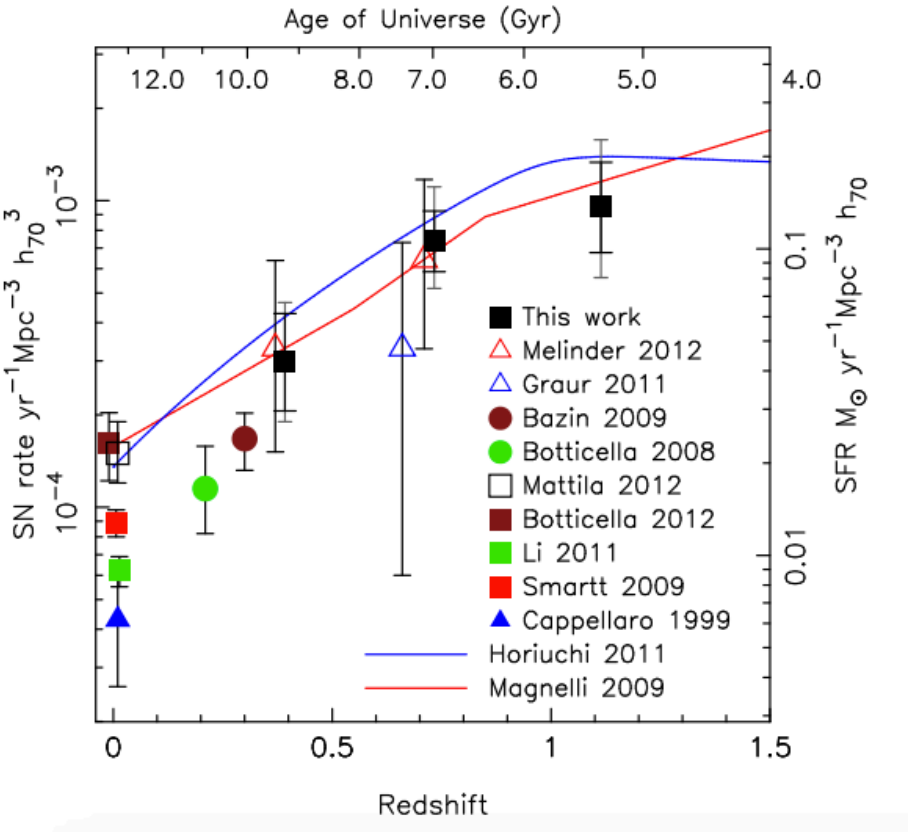

Figure 1.8: Volumetric rate measurements of core collapse SNe as a function of redshift. The lines show two different assumptions for the normalised cosmic star formation history. *Figure credit:* Dahlen et al. (2012).

as expected for stars with a cosmologically significant time delay between formation and subsequent explosion.

1.4.3 Volumetric Rates of Superluminous Supernovae

The majority of this thesis is concerned with the volumetric rate of SLSNe-I. In this section, I describe the motivation for the study of SLSN volumetric rates, and give an overview of the current state of these measurements.

The volumetric rate of SLSNe should follow the cosmic star formation history if their progenitors are massive stars, and can therefore give a strong

indication towards their massive star origin. Assuming SLSNe do originate from massive stars, the volumetric rate measured at different redshift intervals can constrain the shape of the cosmic star formation history with redshift.

Measurements of the volumetric rate of SLSNe are also needed to improve searches for these events by making predictions of the number and distributions which are expected to be found by new and existing surveys such as the Zwicky Transient Facility (ZTF; for a survey overview see Graham et al., 2019), the Large Synoptic Survey Telescope (LSST; for SLSN predictions see Scovacricchi et al., 2016; Villar et al., 2018) and Euclid (for SLSN predictions see Inserra et al., 2018b).

The rate at which SLSNe explode should be consistent with the number of ostensible progenitors expected in the host environment. However, a difficulty in constraining the progenitor systems in this direct manner is that it depends upon a number of poorly understood quantities, such as the fraction of massive stars that form core collapse SNe, and the fraction of core collapse SNe that form rapidly rotating magnetars (if that is the correct model for SLSNe).

A number of measurements of the volumetric rate of SLSNe exist in the literature. Cooke et al. (2012) were the second[5] to estimate the volumetric rate of SLSNe using the SuperNova Legacy Survey (SNLS) carried out by the Canada-France-Hawaii Telescope (CFHT) on Mauna Kea, Hawaii. The authors stacked exposures in the SNLS deep fields to discover 2 SLSN-like events. They obtained spectra for these with the 10m Keck telescope and found redshifts of $z = 2.05$ and $z = 3.90$. From these they estimated an estimate of the volumetric rate of 400 SNe Gpc^{-3} yr^{-1} at redshift of $z \sim 3$, with an error that has subsequently been quoted as 25% (Prajs et al., 2017). The spectroscopic sub-classification of these objects is unknown, while the

[5]Quimby et al. (2011) had previously given a rough estimate of $\sim 10^{-8}\,\mathrm{Mpc}^{-3}\,\mathrm{yr}^{-1}$ at $z \sim 0.3$. They later performed a controlled analysis of the volumetric rate, which is detailed below.

potential of missing objects at these redshifts is also large, especially as they are detected in the far ultra-violet (FUV) which is sensitive to dust extinction. Therefore, this high redshift measurement of all SLSN subtypes is uncertain.

The Robotic Optical Transient Search Experiment (ROTSE-IIIb) is a 0.45m telescope with a wide field of view (3.4 $\deg^2$ per exposure), based at McDonald Observatory in Texas. Quimby et al. (2013) used this instrument to discover 5 SLSNe up to 2009 (2 SLSNe-I and 3 SLSNe-II). They augmented their sample with 19 SLSNe from the literature. They use these objects to calculate a SLSN-I rate of 32^{+77}_{-25} SNe Gpc^{-3} yr^{-1} h^3_{71} at a weighted redshift $\overline{z} = 0.17$. They also find a SLSN-II rate of 151^{+151}_{-82} SNe Gpc^{-3} yr^{-1} h^3_{71} at $\overline{z} = 0.15$, and a total rate for SLSN-like events of 199^{+137}_{-86} SNe Gpc^{-3} yr^{-1} h^3_{71} at $\overline{z} = 0.16$. The weighted redshift is the weighted mean of the redshifts of SNe that contributed to the rate measurement. The weight used for the ith SN is the comoving volume bounded by the observational field and the discovery redshift of that SN.

The Panoramic Survey Telescope and Rapid Response System (Pan-STARRS1; PS1) is a 1.8m telescope with a 7.1 $\deg^2$ field of view based in Haleakala, Hawaii. The PS1 Medium Deep Survey (MDS) is a 10 field astronomical transient search. McCrum et al. (2015) used four spectroscopically classified SLSNe-I from the first year of PS1 MDS, combined with 10 unclassified SLSN-I candidates to estimate a volumetric rate of between $3^{+3}_{-2} \times 10^{-5}$ and $8^{+2}_{-1} \times 10^{-5}$ that of the core collapse SN rate within a redshift range of $0.3 \geq z \geq 1.4$.

Prajs et al. (2017) also use SNLS to measure the SLSN volumetric rate. However, rather than the method of Cooke et al. (2012), they conduct a controlled search for SLSNe within the 5 year main catalogue of SNLS. The SNLS main survey discovered 2 spectroscopically confirmed SLSNe, and Prajs et al. (2017) used a photometric search to discover another good candidate. They used a Monte Carlo simulation method with these 3 objects to calculate a rate of 91^{+76}_{-36} SNe Gpc^{-3} yr^{-1} at a volume weighted redshift of $z = 1.13$.

The Hyper-Suprime Cam (HSC) is a 1.8 $\deg^2$ camera mounted on the

8.2m Subaru Telescope on Mauna Kea, Hawaii. Moriya et al. (2019) use Subaru/HSC to spectroscopically classify 3 high redshift SLSNe of unknown subtype. These spectroscopic classifications are based on very low signal to noise spectra. They assume their detection efficiency $\epsilon = 1$. They find a lower limit to the total SLSN rate of 900 ± 520 SNe Gpc^{-3} yr^{-1} at a redshift $z \sim 2$. They also use two photometrically identified SLSN candidates at host galaxy photometric redshifts of $z \sim 3$ and $z \sim 4$ to compute volumetric rates of 400 ± 400 and $500 \pm 500\,\mathrm{SNe}\,\mathrm{Gpc}^{-3}\,\mathrm{yr}^{-1}$ respectively.

A comparison of these volumetric rate measurements with the normalised cosmic SFH is shown in Figure 1.9. The large uncertainties on the rate measurements allow them to be consistent with the cosmic SFH, and demonstrate that more precise measurements are needed to discover potential inconsistencies between the volumetric rate of SLSNe and the shape of the cosmic SFH, which would give clues to the progenitor systems of SLSNe. The latter two measurements of Moriya et al. (2019) that use single photometric SLSN candidates with galaxy photometric redshifts are not shown due to their lack of constraining power; both of these latter measurements are consistent with zero.

Many detailed measurements of the cosmic SFH exist in the literature (Pascale et al., 2009; Rujopakarn et al., 2010; Ly et al., 2011; Bothwell et al., 2011), that are reasonably consistent with one another (Madau & Dickinson, 2014). For this reason, I do not take a position on the correct model of the cosmic SFH, and have chosen to use the Hopkins & Beacom (2006) parameterisation as has been done historically in volumetric SLSN-I rate measurements (Prajs et al., 2017).

It is clear that more work is required to constrain the volumetric rate of SLSNe, particularly at intermediate and high redshifts. The primary aim of this thesis is to perform a new and controlled measurement of the volumetric rate of SLSNe from DES. In the next section, I give an overview of the layout of this thesis.

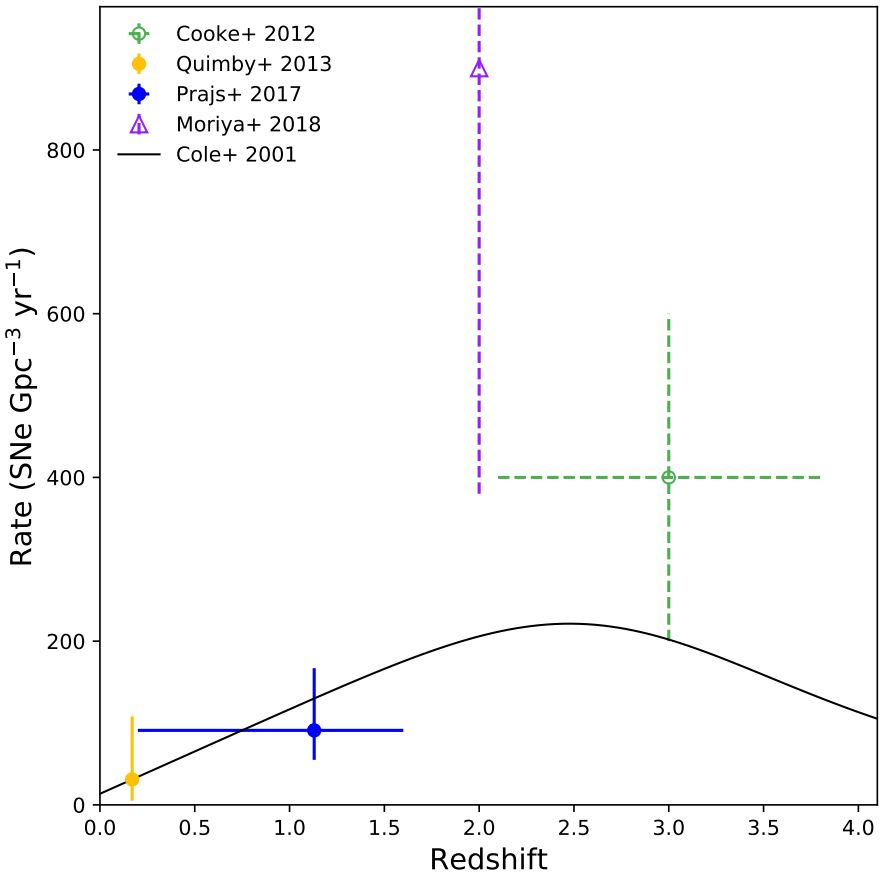

Figure 1.9: The current state of volumetric rate measurements of SLSNe. Solid markers and error bars are measurements of the SLSN-I rate, while empty markers with dotted error bars are measurements of SLSNe with uncertain subtype, but are shown here for comparison. The black line shows the cosmic star formation history of Cole et al. (2001) with the parameterisation of Hopkins & Beacom (2006) normalised to the low redshift Quimby et al. (2013) volumetric rate measurement. See text for more details of the individual measurements.

1.5 Thesis Outline

In the next chapter I introduce DES, and describe the instrumentation, survey objectives, and the DES Supernova Survey (DES-SN). I review the early SLSN search in DES-SN, particularly the work of Papadopoulos et al. (2015).

In Chapter 3, I describe the spectoscopic SLSN sample discovered by DES, particularly the work of Angus et al. (2019). I then detail the construction of the synthetic spectral energy distributions (SEDs) I use to model the lightcurves of these events. I simulate millions of these models to determine the photometric efficiency of the DES-SN search for SLSNe.

In Chapter 4, I perform a search into the DES-SN transient catalogue of $\sim$30,000 transients in search of photometric SLSN candidates which were not spectroscopically classified. I detail the selection criteria and results of this search, and present the photometric sample of SLSNe from DES.

In Chapter 5, I use a Monte Carlo simulation method and results from the previous chapters to compute the volumetric rate of SLSNe from DES. I detail the various components needed for this computation, and describe the statistical and systematic error analyses.

In Chapter 6, I use the lessons learned from this work and apply unsupervised machine learning techniques to explore the DES transient catalogue in a search for additional anomalous SNe.

Finally, in Chapter 7 I conclude with the results of this work, and present an outlook towards the future of SLSN science in upcoming and existing transient surveys such as ZTF (Bellm, 2014; Graham et al., 2019) and LSST (LSST Science Collaboration et al., 2009; Ivezić et al., 2019) which are set to revolutionize the field of time domain astronomy.

Chapter 2

The Dark Energy Survey

This is a review chapter, and references are given throughout. Figure 2.2, Table 2.1, and Table 2.2 are my own.

The Dark Energy Survey (DES; DES Collaboration 2005) ran for ∼5.5 months each year for 6 years. DES was carried out using the Dark Energy Camera (DECam; Flaugher et al. 2015) mounted on the 4m Victor Blanco Telescope at the Cerro Tololo Inter-American Observatory (CTIO) near La Serena in Chile. DECam is a 550 megapixel imaging camera whose constitution includes a hexagonal mosaic of 62 4×2 kpx science CCDs, and 12 additional 2×2 kpx CCDs which are used for calibration and alignment of the system. The 250μm DECam CCDs are thicker than CCDs used in previous imaging surveys, and these 'deep-depleted' CCDs allow DECam to be sensitive to incident photons as far red as 10^4Å (D'Andrea et al., 2018).

The primary aim of DES is to measure the equation of state of dark energy (and any time evolution therein) using four cosmological probes (DES Collaboration, 2005). These are large scale structure (DES Collaboration et al., 2017), galaxy clustering counts and weak gravitational lensing (DES Collaboration et al., 2018a), and SNe Ia as standard candles (DES Collaboration et al., 2019). The first three of these probes are based on the measurement of the coordinates, magnitude, redshift and shape of millions of galaxies, and

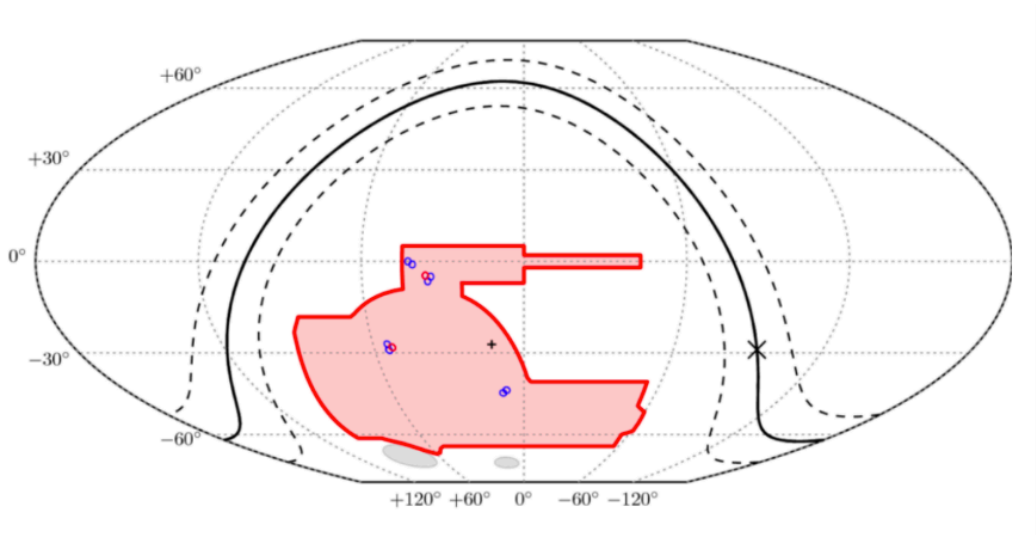

Figure 2.1: The DES wide-field survey footprint is the shaded red area. Small blue circles are SN shallow fields, and red circles are deep fields. The Galactic plane is the solid black line, the Galactic centre is the diagonal black cross, the south Galactic pole is the vertical black cross, and the Large and Small Magellanic Clouds are the grey shaded areas. *Figure credit:* Abbott et al. (2018b).

are limited by different sets of systematic uncertainties which permits the complementarity of their constraints in the Ω_m/Ω_Λ and Ω_m/w planes (e.g. DES Collaboration et al., 2018b). The part of the DES survey pertaining to these three probes was a 5000 deg^2 galaxy survey which observed the southern celestial hemisphere in the g, r, i, z, and Y filters. See Figure 2.1 for the areal coverage of the DES wide-field survey and Figure 2.2 for the system throughput (including filter and atmosphere transmission). The survey concerned with the latter of these probes (Bernstein et al., 2012) was largely independent, but was run in tandem with the wide-field survey described above.

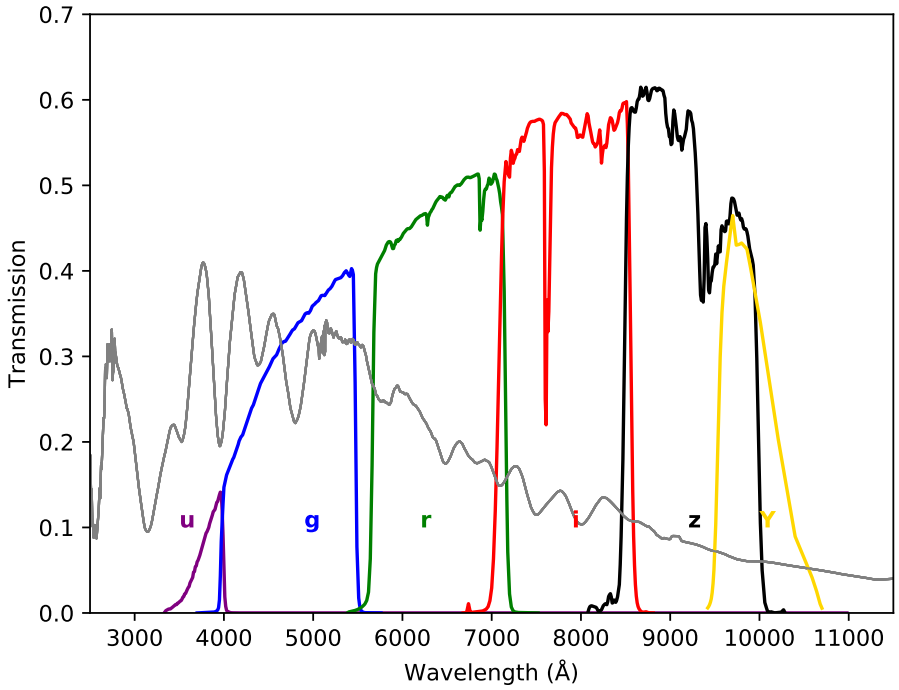

Figure 2.2: The total system throughput for each of the DES filters. The transmission is the product of the quantum efficiency of the CCDs, the throughput of the filters, and the attenuation of the terrestrial atmosphere. The u and Y filters were not used in DES-SN. A scaled SLSN-I template spectrum at $z = 0.8$ is shown in grey for comparison.

2.1 DES-SN Survey Strategy

The DES Supernova Survey (DES-SN; Bernstein et al. 2012; Kessler et al. 2015; D'Andrea et al. 2018) observed 10 fields of hybrid depth every 4 to 7 nights in the g, r, i and z filters. Each of these fields was a single DECam pointing, and had an area of 2.7 deg^2 when accounting for gaps between CCDs and dead CCDs, for a total sky area of the DES-SN survey of 27 deg^2. DES-SN observed 8 shallow fields (C1, C2, E1, E2, S1, S2, X1 and X2) and 2 deep fields (C3 and X3). The field locations were chosen for a multitude of reasons including; their visibility from both CTIO and the northern hemisphere, where many of the spectroscopic facilities for SN follow up and classification are located; the preference to minimise Milky Way dust extinction; the absence of very bright foreground stars; and to overlap with previous survey footprints to provide a cross reference for photometric calibration (Fischer, 2015).

The prefixes of the field names were derived from the galaxy catalogue with which they overlap, 'C' from the Chandra Deep Field South (CDFS; Xue et al. 2011), 'E' from the Elais-S1 field (Gruppioni et al., 1999), 'S' from the SDSS Stripe 82 (Adelman-McCarthy & et al., 2007; Abazajian et al., 2009), and 'X' from the XMM-LSS footprint (Pierre et al., 2004). The suffix of the field name indicates the targeted limiting magnitude, and hence exposure time, of the field exposures: '3' for the deep fields and '1' or '2' for the shallow fields, where the suffix '1' is given to the shallow field with a higher declination. For example, the field X1 was the more northerly of the shallow fields in the XMM-LSS footprint, while X3 was the deep field in that footprint. See Figure 2.3 for a sky map of the DES-SN C fields.

As the DES-SN and DES wide-field surveys were conducted in parallel, the nightly observations of DECam were not trivial to optimally schedule. An automated schedule prioritiser called `obsTac` (Neilsen & Annis, 2014) was used to manage DECam observations. The inputs to `obsTac` included the observing conditions (e.g. weather, seeing, moon position and phase), the completeness of the DES wide-field footprint, and the time since the last ac-

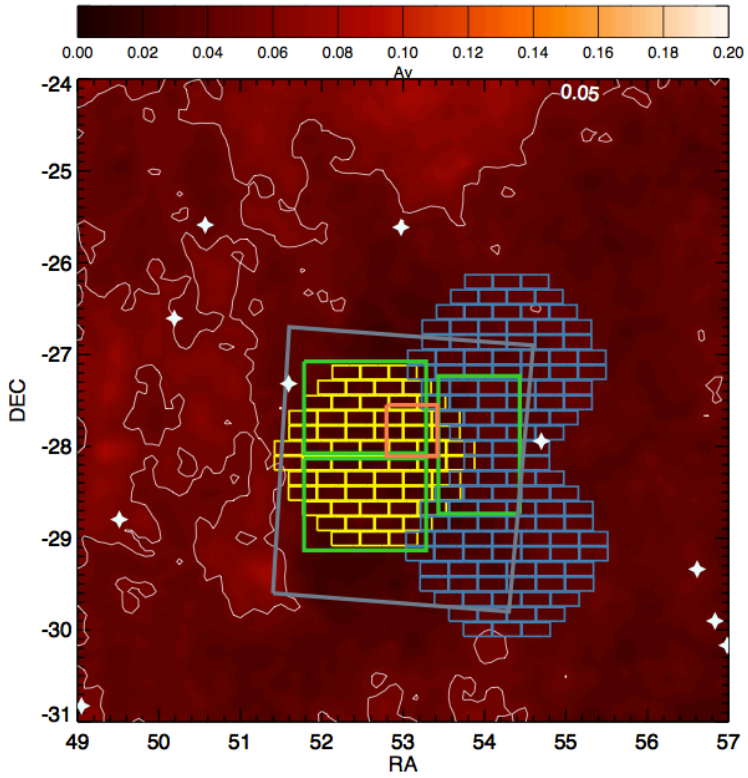

Figure 2.3: Close up of the DES-SN C fields. The shallow fields C1 and C2 are plotted in blue, with the deep field C3 plotted in yellow. Overlaid are the fields of the ancillary surveys: the X-ray CDFS in orange, the near-infrared VIDEO (Jarvis et al., 2013) in green and far-infrared SWIRE (Lonsdale et al., 2003) in grey. A contour map of the Galactic extinction A_v is shown in red. Bright stars are plotted in white. *Figure credit:* Fischer (2015).

cepted exposure in each of the SN field-band combinations (D'Andrea et al., 2018). SN shallow field observations were sequenced such that observations in each of the 4 bands were carried out back-to-back. Deep field observations, however, required an exposure time which was longer by a factor of $\sim$7, and the back-to-back requirement was relaxed such that observations in different filters for a single deep field did not need to occur on the same night (Kessler et al., 2015). In a given field-band, an observation was triggered if the following conditions were met: (1) if the seeing was worse than $1.1''$ and the latest accepted field-band observation occurred > 4 nights previously or (2) if the latest accepted field-band observation occurred > 7 nights previously. Upon reception of the new exposure at the National Centre for Supercomputing Applications (NCSA) in Illinois, the image was passed through the difference imaging pipeline (Section 2.2.2), and labelled as either 'Pass', 'Fail' or 'Junk'. If the image was not of sufficient data quality to receive a 'Pass' label, the timer for the above criteria was not set to zero, and the image was retaken on a subsequent night (D'Andrea et al., 2018). This optimised delay between SN exposures was known as the 'deadman trigger' and naturally provided the cadence of the SN observations. Occasionally a SN observation which would otherwise be triggered was not possible (e.g. if there was insufficient time at the end of the night to complete the exposure sequence) and the observation was instead scheduled for the next night. Typical cadences of DES-SN are shown in Figure 2.4.

Once the raw images were obtained, significant image processing was carried out to obtain well constrained photometry of the SN candidates. All DES data for a single observing night ($\sim$ 1 TB) was transferred via the National Optical Astronomy Observatory (NOAO) Data Transport System (Fitzpatrick, 2010) at a rate of $\sim$1Mbps to NCSA. Further processing steps were carried out on site at NCSA.

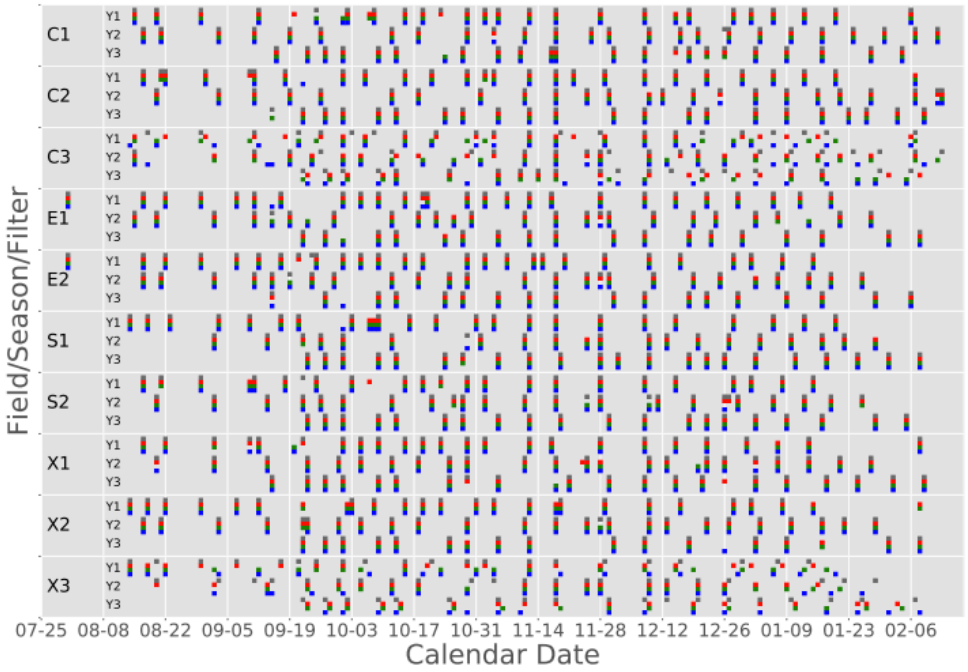

Figure 2.4: Observations of the first 3 years of the DES-SN survey. The filters g, r, i, and z are shown in blue, green, red, and grey respectively. It was required that all four bands were observed back-to-back in the shallow fields, but not in the deep fields due to the longer exposure time. *Figure credit:* D'Andrea et al. (2018).

2.2 DES-SN Data Processing

2.2.1 Preprocessing

The first sequence of steps in the science preparation of the DES images was 'detrending', or the removal of the effect of various instrumental imperfections from the images, and was executed for both the DES-SN images and the DES wide-field images (Sevilla et al., 2011). The detrending procedures were; the masking of known bad pixels in the camera; correction of zero-exposure-time bias from e.g. dark current; flat-field correction to remove pixel-to-pixel variations in sensitivity; pupil ghost correction to account for the effect of multiple light scatterings through the DECam corrector; crosstalk between neighbouring CCDs that share common electronics; nonlinear pixel response such as the well documented 'brighter-fatter effect' (e.g. Antilogus et al., 2014); and overscan correction to account for residual electrons in the CCD which would otherwise bias the readout. See Sevilla et al. (2011); Desai et al. (2012); Mohr et al. (2012); Morganson et al. (2018) for a more thorough exposition of the preprocessing procedures for DECam images.

The images were then passed through the supernova single epoch pipeline (SNSE; Morganson et al. 2018) which masked bright saturated stars and their bleed trails (overflow of electrons into neighbouring pixels along the readout axis), cosmic rays, and satellites. SNSE also fit and subtracted the sky brightness from the image.

2.2.2 The Difference Imaging Pipeline

In modern SN searches (e.g. Equation of State: SupErNovae trace Cosmic Expansion; ESSENCE, Miknaitis et al. 2007; the Sloan Digital Sky Survey SuperNova Survey; SDSS-SNS, Sako et al. 2008; the SuperNova Legacy Survey; SNLS, Perrett et al. 2010; the Panoramic Survey Telescope and Rapid Response System; Pan-STARRS, Rest et al. 2014; the intermediate Palomar Transient Factory; iPTF, Masci et al. 2017), preprocessed science images

were aligned to deep coadded template images of the same sky area. The template image flux was subtracted pixel-by-pixel from the science image flux, and the result was a *difference image*. In the ideal case, the difference image contained only the transient SN light. The flux values from a sequence of these difference images constituted the SN flux variability over time, (i.e. its lightcurve). If the difference imaging procedure was carried out in multiple filters, multicolour lightcurves could be obtained.

The DES-SN difference imaging pipeline `DiffImg` is detailed in Kessler et al. (2015). The various components of `DiffImg` used publicly available `AstrOmatic`[1] codes. `SExtractor` (Bertin & Arnouts, 1996) was used to identify objects, `PSFEx` (Bertin, 2011) to measure the position dependent point spread function (PSF) of the objects, and `SWarp` (Bertin, 2010) to determine an astrometric solution to the alignment of template and search images. The template images were constructed from coadded images in years other than the current science year. Y1 templates were originally constructed from science verification images, but later from Y2 images, Y2 templates were constructed from Y1 images, and templates for the subsequent 3 years were constructed from Y2 images. Single epoch template images were aligned using the United States Naval Observatory All-Sky Catalogue (USNO-B1; Monet et al. 2003), and coadded. These coadds were then realigned with the science image using `SWarp`. A modified version of the code `hotPants` (Becker, 2015) was used to perform the subtraction on a CCD-by-CCD basis.

The difference imaging process was prone to non-astronomical source detections resulting from e.g. astrometric misalignment, called artefacts. Artefacts were rejected based initially on simple quality selection criteria on 35×35 pixel 'stamps' around the extracted sources. These criteria included (1) fewer than 200 pixels with a flux less than 2σ below zero (2) fewer than 20 pixels with a flux less than 4σ below zero and (3) fewer than 2 pixels with a flux less than 6σ below zero (Kessler et al., 2015). These requirements helped to reject 'dipoles' - a common type of subtraction artefact that re-

[1] https://www.astromatic.net/

sulted from small misalignments between the template and science images. Sources coincident with known photometric variable sources and bright stars were similarly rejected (Morganson et al., 2018).

Sources which passed the above criteria were catalogued as 51×51 pixel stamps centered on the source. Further filtering of artefacts was carried out by the machine learning algorithm `autoScan` (Goldstein et al., 2015). `autoScan` is a random forest regression algorithm intended to sort artefacts from true astrophysical transient detections. The algorithm was trained on a sample of 900,000 sources (Kessler et al., 2015), half of which were human verified artefacts and half of which were fake astrophysical transient sources. `autoScan` assigned each stamp a score between 0 (artefact) and 1 (astrophysical detection). Two separate sources which passed `autoScan` with a score better than 0.3 and were separated by less than $1''$ formed a science candidate. As further epochs were detected they were added to the science candidate lightcurve.

The next step was to associate science candidates with their host galaxies. In determining the true host of a candidate one encounters an astrometrical problem. A schematic from Gupta et al. (2016) that portrays this issue is shown in Figure 2.6. In this figure, the central SN is positioned between two nearby galaxies. The centroid of the smaller galaxy is closer to the SN in angular distance, and one might choose to naively designate this galaxy as the host. However, it may also be a distant background galaxy. One solution to this issue is the directional light radius, d_{DLR}, method of Sako et al. (2018). This method normalises the angular separation between SN and prospective host, Ψ, by the DLR:

$$d_{\mathrm{DLR}} = \frac{\Psi\,(\mathrm{arcsec})}{\mathrm{DLR}\,(\mathrm{arcsec})}. \tag{2.1}$$

where the DLR is the angular radius of the prospective host in the direction of the SN. A similar method was used by Sullivan et al. (2006) for SNLS.

In the DES-SN pipeline, d_{DLR} was computed for all galaxies within a $15''$ radius around the transient (Gupta et al., 2016). If no galaxies were found with $d_{\mathrm{DLR}} < 4$, the SN was labelled as 'hostless'. If there were galaxies with

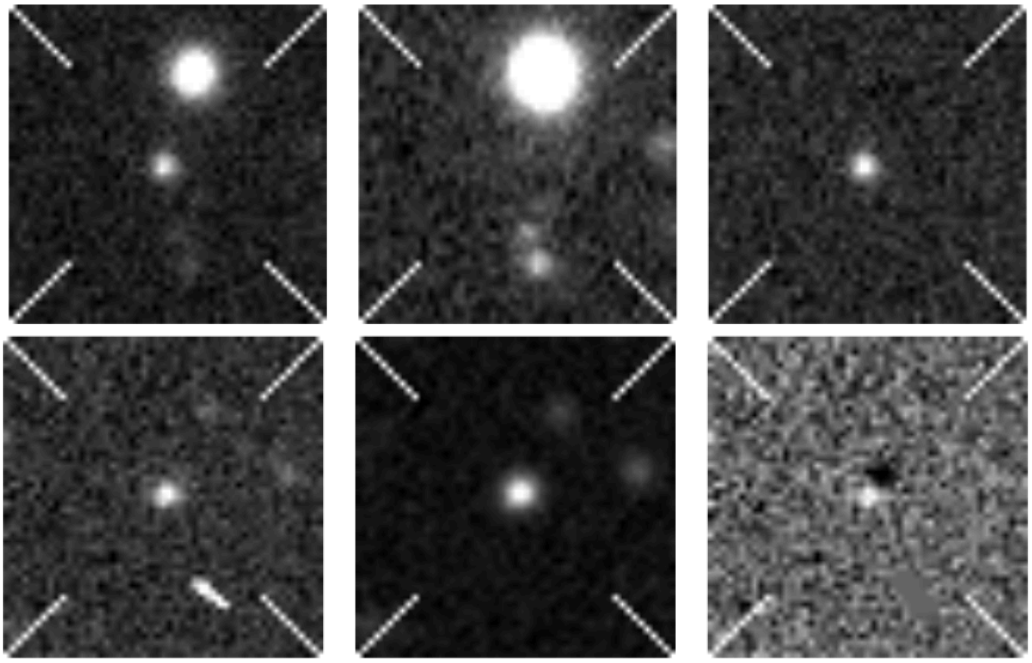

Figure 2.5: Example stamp triplets produced by the difference imaging pipeline. The science image is on the left, the coadded template image is in the centre, and the difference image is on the right. The top row shows a stamp triplet from a classified SN Ic, with a foreground star in the science and template images which has been subtracted out in the difference image. The bottom row shows a common type of artefact, where a dipole effect was caused by a small misalignment between science and template images in the subtraction process (Morganson et al., 2018). These stamps were taken directly from the DES candidate webpage.

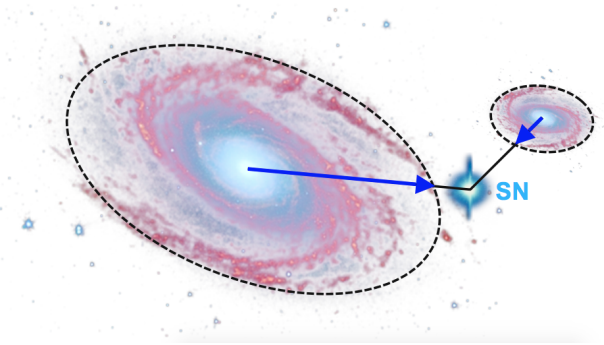

Figure 2.6: Schematic showing the host galaxy identification problem in supernova surveys. The correct host galaxy designation is ambiguous using angular separation alone. *Figure credit:* Gupta et al. (2016).

$d_{\mathrm{DLR}} \leq 4$, the galaxy with the smallest d_{DLR} was labelled as the SN host.

Once the host galaxies were assigned, the flux and uncertainty at other DES-SN observation epochs was computed for the science candidate using a procedure known as 'forced photometry' (Kessler et al., 2015). The forced photometry procedure used `PSFEx` to fit a PSF to the source and thereby extract the flux and its uncertainty. The PSF-fitted flux was computed at the right ascension (RA) and declination (Dec.) coordinates for all previous epochs of observation, including those in which there was no source detection. This process allowed construction of full five year lightcurves for the science candidates. An example single season lightcurve is shown in Figure 2.7.

In most modern cosmological SN surveys, a photometric classifier is needed to select the science candidates that are most likely to be Type Ia, which are then prioritised for spectroscopic follow up. However, it is difficult to know which SNe are true SNe Ia from the lightcurve alone, especially at early times when only a few epochs of the rising lightcurve have been observed. Many photometric SN classifiers have been developed to mitigate the issue of erroneously designating resources to other SN types. The final step of the `DiffImg` pipeline used the photometric SuperNova IDentification algorithm (`pSNID`) (Sako et al., 2008, 2011). This classifier searches a grid of model SN Ia, SN Ib/c and SN II template lightcurves to find the minimum reduced

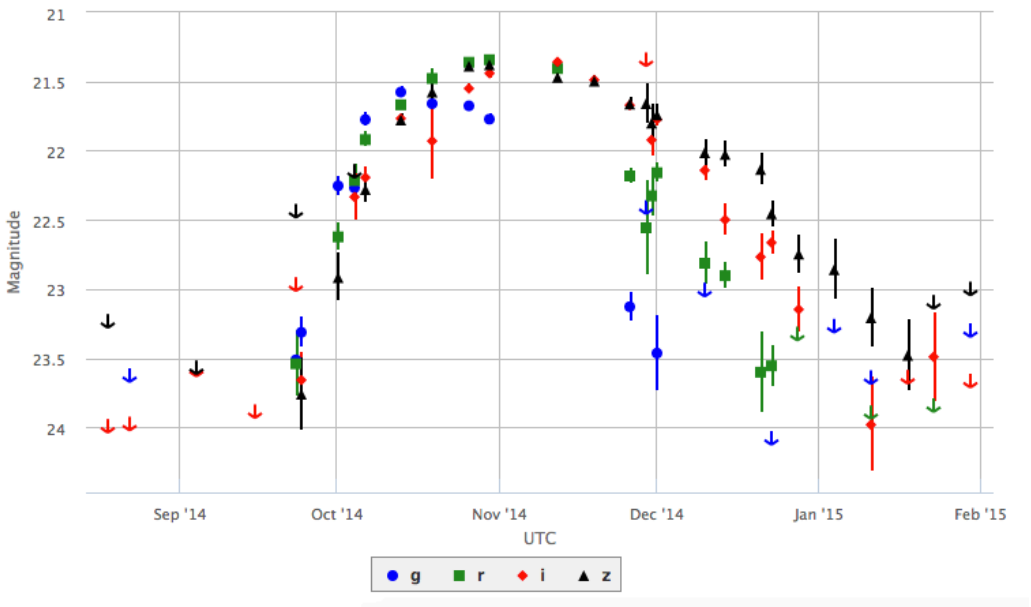

Figure 2.7: Example single season multicolour lightcurve of the spectroscopically confirmed SLSN-I DES14X2byo. Each photometric point represents the flux and uncertainty measurement from the PSF fit to the source on the difference image. The downward pointing arrows are 5 sigma upper limits for 'non-detections' (i.e. when the signal to noise < 5.) The different colours represent different filters (*griz*). This figure was taken directly from the ATC webpage which was used to coordinate the spectroscopic follow up of DES-SN.

$\chi^2_{\rm min}$ for each SN type across a grid of redshifts. When fit to the observed photometry, the relative $\chi^2_{\rm min}$ values between SN type-redshift combinations were used in selecting SNe Ia for spectroscopic follow up in DES-SN. Redshift priors can also be set if available from host galaxy spectra. If the `fitprob` > 0.5 for one or more of the type-redshift combinations, the combination with the highest `fitprob` was designated as the photometric type of the candidate. These candidates were prioritised for spectroscopic follow up.

2.3 Spectroscopic follow up

The spectroscopic observing time that would be required to acquire spectra of (i.e. 'follow up') all transients that were identified by the difference imaging pipeline vastly exceeded the resources available to the DES-SN follow up program (Bernstein et al., 2012). Therefore, the primary DES-SN cosmology analysis will use a photometrically classified sample of SNe Ia. Nonetheless, spectroscopy is vital to DES-SN both to train photometric classification algorithms and to provide host galaxy redshifts to place photometric SNe Ia at precise redshifts on the Hubble diagram (D'Andrea et al., 2018).

The DES-SN follow up program spectroscopically observed both SN explosions ('live SNe') and their host galaxies. Host galaxy spectra were primarily obtained by the Australian Dark Energy Survey (OzDES; Yuan et al. 2015; Childress et al. 2017). OzDES was a 100 night programme over 6 years which used the Two Degree Field (2dF) fibre positioner and the AAOmega spectrograph (Saunders et al., 2004; Smith et al., 2004) with the 3.9m Anglo-Australian Telescope (AAT). In this configuration the AAT footprint is nearly identical to that of DECam, and tens of thousands of targets across the DES-SN fields were routinely observed and revisited across multiple epochs, allowing stacking of spectra to achieve sufficient signal to noise for a secure redshift of the host to be obtained (D'Andrea et al., 2018). I use these host galaxy redshifts obtained with OzDES in Chapter 5 for the computation of the volumetric rate of SLSNe, in particular where the spectroscopic redshift

of the SN was unavailable.

The DES-SN follow up program for live SNe Ia functioned in three parts; a campaign for a magnitude limited sample of spectroscopic SNe Ia; a campaign for SNe Ia in faint hosts; and a campaign for a representative sample of spectroscopic SNe Ia which followed the redshift distribution of photometric SNe Ia observed by DES-SN. These observing campaigns were designed to reduce biases in the final cosmological sample of spectroscopically confirmed SNe Ia, as well as to provide a control sample for later photometric cosmology analyses (D'Andrea et al., 2018).

A parallel spectroscopic campaign was aimed at obtaining spectra of three particular non-Ia types: tidal disruption events (TDEs), type II SNe, and SLSNe. While type II SNe have shown potential as low redshift standardisable candles (e.g. Hamuy & Pinto, 2002), both TDEs (Komossa & Bade, 1999) and SLSNe (Quimby et al., 2007) have been optically observed for the first time relatively recently and therefore present rich fields of research. Of most concern to this thesis is the effort to obtain spectra of SLSNe.

The spectroscopic program to classify SLSNe was developed over the course of DES-SN. Early efforts are described in Section 2.4, while a matured approach is described in Chapter 3. Promising photometric candidates were spectroscopically observed by one of an international array of telescopes. The facilities which contributed to the spectroscopic follow up of SLSNe were; the Gemini Multi Object Spectrographs (GMOS; Hook et al. 2004) mounted on the Gemini North telescope on Maunakea, Hawaii, and the Gemini South telescope on Cerro Pachon, Chile; the Optical System for Imaging and low Resolution Integrated Spectroscopy (OSIRIS; Cepa et al. 2003) mounted on the 10.4m Gran Telescopio Canarias (GTC) at the Observatorio del Roque de Los Muchachos in La Palma; the DEep Imaging Multi-Object Spectrograph (DEIMOS; Faber et al. 2003) and the Low Resolution Imaging Spectrograph (LRIS; Oke et al. 1995) mounted on the 10m W. M. Keck Observatory on Maunakea, Hawaii; the Low Dispersion Survey Spectrograph (LDSS-3) and the Inamori Magellan Areal Camera and Spectrograph (IMACS; Bigelow

et al. 1998) mounted on the twin 6.5m Magellan Baade and Clay telescopes at Las Campanas Observatory, Chile; the Blue Channel Spectrograph (BCS; Angel et al. 1979) mounted on the 6.5m Multiple Mirror Telescope (MMT) at the Fred Lawrence Whipple Observatory in Mount Hopkins, Arizona; the X-shooter echelle spectrograph (Vernet et al., 2011) mounted on the 8.2m Very Large Telescope (VLT) at the European Southern Observatory (ESO) on Cerro Paranal, Chile; and the AAOmega spectrograph using the 2dF fiber positioners (Saunders et al., 2004; Smith et al., 2004) mounted on the 3.9m AAT at the Siding Spring Observatory in Australia.

Once spectra of sufficient quality of these objects were obtained and reduced, classifications could be performed. The number of spectra obtained and classifications made per facility over the 5 year DES-SN program are shown in Table 2.1. The number of classifications made per transient class is shown in Table 2.2. Multiple classifications for a single object may be present in Table 2.1, and the reduction and logging of these spectra is ongoing.

While `pSNID` was used to photometrically identify the relatively well understood SN types (SN Ia, SN Ib/c, and SN II) and thereby to inform the DES-SN spectroscopic follow up programs, it does not yet have the capability to identify SLSNe (Papadopoulos et al., 2015). Therefore, other methods were sought to identify promising SLSN candidates for spectroscopic follow up.

2.4 SLSNe in the First Year of DES-SN

Early work on the search for photometric SLSN candidates in DES-SN was carried out by Papadopoulos (2016). The underlying idea of this photometric search was to accept and reject objects based on a combination of their observed photometric and host galaxy properties, which were available from the data products of the difference imaging pipeline. This is often difficult as (1) assumptions based on photometric properties of SLSNe do not necessarily apply to all members of this diverse population, and true SLSNe may be

Telescope	Total spectra	Evaluated spectra
AAT	2164	848
Magellan	205	116
VLT	200	77
SALT	87	38
Gemini	125	33
MMT	45	27
Keck	47	19
GTC	37	19
NTT	9	8
SOAR	2	2
Okayama	1	1
Lick	1	1

Table 2.1: The number of spectra obtained per facility. The final column shows the number of spectra for which a spectroscopic classification was possible. For a given object, classification quality spectra may have been obtained by multiple facilities. These data were retrieved from `snspect` on 28th May 2019.

Type	Total classifications	Robust classifications
SN Ia	415	356
AGN	59	58
SN II	62	46
SLSN-I	19	16
SN Ib/c	11	7
SN IIb	5	5
SN Ic	4	4
M-Star	3	3
SN IIn	1	0
SN Ia-pec	1	0
SN Ib	1	1
SN I	1	1
SLSN-II	1	0
TDE	1	1

Table 2.2: Classifications made by the DES-SN follow up program. Some classifications were labelled as uncertain in `sncand`, due to either low signal to noise, or because classification features were redshifted out of the observed wavelength range. These data were retrieved from `sncand` on 27th May 2019.

rejected by the criteria and (2) non-SLSN objects may fulfill the criteria and be introduced to the photometric sample as contaminants. Despite this, good candidates can be selected with a careful choice of criteria. These criteria are usually based on the observed properties of SLSNe from past surveys.

Papadopoulos (2016) searched for SLSNe within the first year of DES-SN data. They first applied their selection criteria to the large sample of science candidates produced by the difference imaging pipeline. These criteria were: (1) at least one month of multicolour data, typically 5 to 6 detections with a signal to noise > 3.5 in all 4 *griz* bands; (2) a low `pSNID` fit probability to each of the standard SN types (SN Ia, SN Ib/c, and SN II); (3) a location at least 1 pixel from the prospective host (if one is observed in the template image) and (4) a peak observed brightness at least 1 mag brighter than the prospective host (if observed).

These criteria reduced the 26,000 science candidates from Y1 to a sample of $\sim$1500 objects, the majority of which were artefacts. Upon visual inspection, 300 real astrophysical transients were selected from these, most of which were active galactic nuclei (AGN). However, a small fraction were likely SNe, and on comparison with host galaxy properties 12 of these were identified as promising SLSN candidates. One of these candidates was subsequently spectroscopically classified: DES13S2cmm (Papadopoulos et al., 2015). The remaining 11 were either classified as non-SLSNe, or faded below the limiting magnitude of the spectroscopic facilities before observation was possible (Papadopoulos, 2016).

The DES SLSN spectroscopic program has since matured (Angus et al., 2019), and I describe it in more detail in Chapter 3. As well as live photometric identification, photometric searches are also performed in retrospect (e.g. Prajs et al., 2017). I perform a retrospective photometric search using the entire catalogue of DES-SN transients in Chapter 4 to mitigate the effects of incompleteness in my rate calculation of Chapter 5.

2.5 Data Access

A multitude of data pertaining to each of the science candidates are available from the DES Data Management system (DESDM; Sevilla et al. 2011; Desai et al. 2012; Mohr et al. 2012; Morganson et al. 2018). These data are accessible through the tool `easyaccess` (Carrasco Kind et al., 2019), using `Oracle`, a version of the Structured Query Language (`SQL`). `easyaccess` can be used as an interactive tool from the terminal or through a convenient `python` wrapper.

The data and tables present in DESDM and available with `easyaccess` which are relevant to SN studies include; forced photometry lightcurves and corresponding metadata from `snforce`; transient names, spectroscopic redshifts, and RA and Dec. coordinates from `sncand`; host galaxy information for the closest 3 prospective hosts including spectroscopic and photometric redshifts and their uncertainties and $d_{\rm DLR}$ measurements from `sngals`; and data pertaining to spectroscopic observations of transients in `snspect`. Data from each of these tables are used extensively in this thesis, and permit the entire DES-SN observational and data reduction processes to be traced and recalled in an efficient way.

An essential component of this thesis is the sample of multicolour spectroscopically confirmed SLSN lightcurves, which I retrieve from `sncand`. An example `SQL` query I use to retrieve the lightcurve of the spectroscopically classified SLSN-I, DES14X2byo, is shown below. In the next chapter I present the full sample of SLSN lightcurves from DES and fit modified absorbed black body models to these in preparation for the simulations of Chapter 4.

```
1 select f.mjd_obs,f.flux,f.flux_err,f.band
2 from snforce f join sncand c
3 on f.sncand_id = c.snid
4 where mod(f.status,1024) <= 4
5 and c.transient_name = 'DES14X2byo';
```

Chapter 3

Spectroscopic Superluminous Supernovae and Simulations

The work described in Section 3.1 of this chapter was carried out by Angus et al. (2019). I am a co-author of Angus et al. (2019), but my contribution was the photometric search of Chapter 4. The work detailed in Section 3.2 is my own, although I used a code developed by S. Prajs in Section 3.2.2. The work detailed in Section 3.3 is entirely my own. References to other works, where necessary, are given throughout.

Until 2018, homogeneously selected samples of SLSNe were limited to less than 5 total objects (e.g. Cooke et al., 2012; Howell et al., 2013; Prajs et al., 2017). However, the recent rise of untargeted, wide field, rolling cadence, and deep astronomical surveys (e.g. PTF, Rau et al. 2009; Law et al. 2009; Pan-STARRS, Kaiser et al. 2010) has facilitated statistically informative population studies of SLSNe. In 2018, PTF released a sample of 26 SLSNe-I at low redshift ($z < 0.75$, $\bar{z} = 0.33$, De Cia et al. 2018). Meanwhile, Pan-STARRS released a sample of 17 SLSNe-I in the redshift range $0.3 < z < 1.6$ (Lunnan et al., 2018).

In this chapter I will present the sample of 22 SLSNe that DES-SN spectroscopically classified over its 5 year observational period. I will describe a

modified black body model that I fit to the observed lightcurves to represent their detectability. I used this model to simulate synthetic SLSN lightcurves across the DES-SN observed volume and time, and thereby characterised the photometric completeness of the DES-SN survey for SLSNe.

3.1 Spectroscopically confirmed SLSNe

As detailed in Chapter 2, the spectroscopic follow up program of DES-SN prioritised observation of SNe Ia. However, some resources were designated to the observation of SLSNe (D'Andrea et al., 2018). From Y2 onwards, SLSN candidates were photometrically identified through combinations of the following criteria (Angus et al., 2019); (1) where the entirety of the SN rise was visible in the photometry, the rise time must be > 25 days in the observer frame; (2) where the entirety of the SN decline was visible, the SN must have been visible for > 25 (observer frame) days and show a slow decline rate (< 0.1 mag day^{-1}); (3) the transient must be predominantly blue in colour ($g - r < 1.0$ mag or $r - i < 1.0$ mag); (4) the colour must evolve during the decline (to avoid AGN contamination); (5) the transient must either reside in a dim host ($m_{\rm host} - m_{\rm SN} > 0.7$), or a host that was not detected in the single epoch template images (i.e. a 'hostless' candidate).

Spectroscopic follow-up was triggered for a total of 30 SLSN candidates. Another 2 SLSNe were spectroscopically observed based on high `pSNID` probabilities of fit to SNe Ia, and were later serendipitously classified as SLSNe. As a result of these observations, DES-SN spectroscopically classified 21 SLSNe-I and 1 SLSN-II over its 5 year observing period (Angus et al., 2019). Spectroscopic redshifts were obtained from the reduced spectra using either host galaxy emission lines (Hβ, OII λ3727Å, OIII λ4959Å, λ5007Å) or narrow host absorption features (MgII λ2796Å, λ2803Å, FeII λ2344Å). The multi-colour photometry of the lightcurves of these SLSNe is shown in Figure 3.1. I describe the individual objects which constitute the DES sample below. Peak magnitudes are derived from the model fits of Section 3.2.2, unless otherwise

stated. I describe the redshift distribution and luminosity function of these objects in Section 3.1.2.

DES13S2cmm

This transient was the only SLSN that was spectroscopically confirmed in the first year of DES-SN, and indicated the success of the early SLSN search in DES (described in Chapter 2). A spectrum was obtained with VLT/X-shooter on 21st Nov 2013, and this object was classified as a SLSN-I at $z = 0.609$. I calculated a peak absolute magnitude in the i band of $M_{\rm i} = -20.34$. At the time, this was relatively faint for a SLSN, and DES13S2cmm would not have been classified as a SLSN based on the early criterion of Gal-Yam (2012). The rise of DES13S2cmm was partially observed by the first season of DES, while after peak DES13S2cmm declined slowly, and may be of the slow-evolving subclass of SLSNe-I. This SLSN is described in detail in Papadopoulos et al. (2015).

DES14C1fi

This SLSN-I was the first discovered in DES Y2, and was initially identified as a SLSN candidate due to its slow photometric evolution. A Keck spectrum was obtained on 24th Oct 2014, indicating that this object was a SLSN-I at a redshift of $z = 1.3$, later confirmed by a VLT/X-shooter spectrum taken on 30th Nov 2014. The redshift allowed me to calculate a peak i band magnitude of $M_{\rm i} = -21.62$. The observer frame photometric evolution of this SLSN is similar to DES13S2cmm, despite its much higher redshift, indicating that this SLSN evolved more quickly in the rest frame.

DES14C1rhg

This object was first identified as a SLSN candidate as no host galaxy was detected in the coadded template image. A VLT/X-shooter spectrum of this object was obtained on 29th Dec 2014, from which this object was classified

as a SLSN-I at a redshift of $z = 0.481$ with peak i band magnitude of $M_{\rm i} = -19.35$. DES14C1rhg is therefore the faintest SLSN observed in any survey at the time of writing. Combined with the fast decline in the lightcurve, this object is photometrically anomalous in the sample, despite its spectroscopic similarity to the SLSN-I class.

DES14E2slp

This object was identified as a SLSN candidate as no host galaxy was detected in the template image and it exhibited a relatively long rise and blue colour. A VLT/X-shooter spectrum was obtained on 29th Dec 2014. This transient was classified as a SLSN-I at $z = 0.570$. This object was detected late in the season, and post peak photometry is only available in the g band, making it difficult to constrain the peak magnitude. Angus et al. (2019) use Gaussian processes to estimate a peak absolute magnitude in a synthetic passband centred at 4000Å of $M_{4000} = -20.51$.

DES14S2qri

DES14S2qri was targeted for spectroscopic follow up as its host was undetected in the template images, and it displayed a long rise in the redder bands. A GTC/OSIRIS spectrum was obtained on the 21st January 2015, and this object was classified as a SLSN-I at a redshift $z = 1.49$ and peak $M_{\rm i} = -21.84$. This is a photometrically peculiar SLSN-I due to strong early absorption in the g band, which subsequently subsides.

DES14X2byo

DES14X2byo was identified as a SLSN candidate due to its long rise time, blue colour and lack of a detected host. The spectroscopic coverage of this object was extensive, with observations from GTC/OSIRIS, AAT/AAOmega, MMT/BSC, and Magellan. The classification spectrum was obtained by Keck on 24th Oct 2014, and this object was identified as a SLSN-I at $z =$

0.869, with a peak i band magnitude of $M_{\rm i} = -21.60$. This SLSN-I is bluer than in the archetypal case.

DES14X3taz

DES14X3taz is one of four DES SLSNe to be published independently from the rest of the sample (Smith et al., 2016). This SN exhibited the first case of a pre-peak 'bump' now seen in many SLSN-I lightcurves (e.g. Nicholl & Smartt 2016). It was initially identified in its bump phase as a potential SN Ia, but was not targeted for follow-up. Upon a later visual inspection of the lightcurve it was observed to be rising, and a spectrum was obtained by GTC/OSIRIS on 26th Jan 2015. This object was classified as a SLSN-I at $z = 0.608$. The peak of this object was not detected within the DES-SN season, but Angus et al. (2019) estimated $M_{4000} = -21.72 \pm 0.20$.

DES15C3hav

DES15C3hav was initially targeted as a SLSN candidate due to its long rise time and predominantly blue color. An MMT/BSC spectrum was obtained on the 9th Nov 2015, and this object was classified as a SLSN-I at $z = 0.392$ with peak $M_{\rm i} = -19.48$. The faint peak puts this object on the very lower end of the luminosity function of SLSNe (Section 3.1.2). Post-discovery analysis detected a pre-peak bump in the early lightcurve of DES15C3hav which was redder than the bumps seen in other SLSNe (Angus et al., 2019).

DES15E2mlf

DES15E2mlf was initially identified by `pSNID` as a SN Ia candidate at $z \sim 0.3$. The photometric redshift of a nearby host galaxy matched this prediction, and DES15E2mlf was observed by Gemini/GMOS on 15th Dec 2015 under the program to spectroscopically identify nearby SNe Ia. Surprisingly, the observed spectrum was instead consistent with a SLSN-I at $z = 1.86$. DES15E2mlf therefore has a peak $M_{\rm i} = -22.01$. This object is one of the

brighter SLSNe in the DES sample. DES15E2mlf is described in detail in Pan et al. (2017).

DES15S1nog

DES15S1nog is another example of a serendipitous SLSN discovery in DES. It was initially identified by `pSNID` as a good fit to a SN Ia. A GTC/OSIRIS spectrum was obtained on 11th Feb 2016, and this transient was classified as a SLSN-I at $z = 0.566$ with a peak $M_{\rm i} = -19.92$. This SLSN-I is photometrically anomalous due to its fast rise time, especially in the bluer bands.

DES15S2nr

DES15S2nr was initially targeted as a SLSN candidate due to its long rise time, blue colour, and clear evidence for a pre-peak bump (at the time a recently discovered attribute of SLSNe). Spectra were obtained by a wide array of facilities, including VLT/X-shooter, SALT and AAT/AAOmega. The classification spectrum was obtained with Keck/LRIS, which confirmed DES15S2nr as a SLSN-I at $z = 0.22$ with a peak $M_{\rm i} = -20.45$.

DES15X1noe

DES15X1noe was targeted as a SLSN candidate due to its very slowly rising lightcurve. A spectrum was obtained by GTC/OSIRIS on 28th Jan 2016, and this object was classified as a SLSN-I at $z = 1.188$. This object is one of the most slowly evolving SLSNe in the DES sample, with detected epochs in the year after its initial classification, and a rise time of ~ 50 rest frame days. Angus et al. (2019) estimated an uncertain peak magnitude in the synthetic passband of $M_{4000} = -23.37 \pm 3.37$.

DES15X3hm

DES15X3hm was initially targeted as a SLSN candidate due to its slowly declining lightcurve, blue colour, and undetected host galaxy. A VLT/X-

shooter spectrum was obtained on 9th Sep 2015, classifying this object as a SLSN-I at $z = 0.86$. Angus et al. (2019) estimated a peak $M_{4000} = -22.0 \pm 0.15$. This object is perhaps the most archetypal of the SLSNe in the DES sample.

DES16C2aix

DES16C2aix was targeted as a SLSN candidate due its long rise time. A spectrum was obtained by Magellan on 10th Oct 2016, classifying this object as a SLSN-I at $z = 1.07$, with a peak $M_{\rm i} = -21.44$. This object is particularly interesting as there are no detected epochs in the g band, indicating heavy flux absorption in the UV.

DES16C2nm

DES16C2nm is the final DES SLSN to be independently published in Smith et al. (2018). This object was initially targeted due to its very slowly evolving lightcurve, and was spectroscopically observed and classified as a SLSN-I by Magellan on the 10th Oct 2016. It was subsequently observed by VLT/X-shooter and Keck/LRIS which confirmed its redshift as $z = 1.99$, making it the highest redshift spectroscopically classified SN at the time of discovery. Smith et al. (2018) estimated a peak U band magnitude $M_{\rm U} = -22.26 \pm 0.06$, putting this object in the bright tail of the SLSN luminosity distribution.

DES16C3cv

DES16C3CV was initially targeted as a hostless SLSN candidate with a slow rise. A Magellan spectrum was obtained on 10th Oct 2016, and this object was spectroscopically classified as a SLSN-I at $z = 0.727$. However, the lightcurve of this object is truly anomalous even for a SLSN-I, as it shows two broad peaks of comparable luminosity separated by 60 rest frame days. It has been suggested that this is indicative of significant interaction between the SN ejecta and previously shed circumstellar material (C. Inserra, private communication). The initial peak was of magnitude $M_{\rm i} = -21.42$.

DES16C3dmp

DES16C3dmp was initially targeted as a SLSN candidate due to its blue colour and slow rise. A VLT/X-shooter spectrum was obtained on the 20th Dec 2016 and this object was classified as a SLSN-I at $z = 0.526$, with a peak $M_{\rm i} = -20.43$. The g band peak in the lightcurve of this object is particularly sharp, and the lightcurve declined slowly, with robust detections in the year subsequent to its classification.

DES16C3ggu

DES16C3ggu was targeted as a SLSN candidate due to its blue colour and slow rise. A VLT/X-shooter spectrum obtained on 25th Feb 2017 classified this object as a SLSN-I at $z = 0.95$. The object reached peak outside of the DES season, so model fits are unconstrained. However, Angus et al. (2019) used Gaussian processes to estimate a peak magnitude of $M_{4000} = -21.09 \pm 0.37$.

DES17C3gyp

This object was targeted as a SLSN candidate due to its blue colour, slow rise and faint (but detected) host galaxy. An OzDES spectrum taken with AAT/AAOmega on 24th Jan 2018 tentatively classified this object as a SLSN-I at $z = 0.47$, which constrained the peak $M_{\rm i} = -21.57$, fairly typical of a SLSN-I.

DES17E1fgl

This object was identified as a SLSN candidate due to its blue colour and slow rise. A spectrum was obtained by AAT/AAOmega on 22nd Dec 2017. This spectrum showed similarities to the spectra of SLSN-I at $z = 0.52$, but with a clear H-β feature. Therefore, this object is classified as a SLSN-II; the only hydrogen rich SLSN in the DES-SN sample. The peak brightness of

this object fell outside of the DES season, but Angus et al. (2019) estimated a peak magnitude of $M_{4000} = -20.58 \pm 0.18$.

DES17X1amf

DES17X1amf was identified as a SLSN candidate due to its slow rise and faint host galaxy. A Magellan spectrum was obtained on the 10th Nov 2017, and this transient was classified as a SLSN-I at $z = 0.92$ with $M_{\rm i} = -21.76$. This was fairly bright for a SLSN-I, as expected at high redshift.

DES17X1blv

DES17X1blv was identified as a SLSN candidate due its long rise time and faint host galaxy. A VLT/X-shooter spectrum was obtained on 11th Nov 2017. The spectrum was archived, and was not reduced until this object was rediscovered by my photometric search for SLSN candidates in Chapter 4. When the VLT spectrum was reduced, this transient was classified as a SLSN-I at $z = 0.69$. Model fits gave a peak $M_{\rm i} = -20.37$.

3.1.1 Spectroscopic incompleteness

The signal to noise limit of spectroscopic facilities is a function of the exposure time of their observations, and time on these telescopes is expensive. As a result, the spectra of 10 objects which were identified as SLSN candidates were not of sufficient signal to noise for a secure classification to be made, especially when these objects were observationally faint (e.g. intrinsically faint or high redshift SLSNe). In some cases, observational artefacts may also distort the 2D spectra to such a degree that spectroscopic classification is not possible. The aim of Chapter 4 is to account for this spectroscopic incompleteness, and many of these objects are rediscovered as photometric SLSN candidates and are present in the sample used for my final rate calculation in Chapter 5.

As described above, the spectroscopic sample exhibits a large degree of

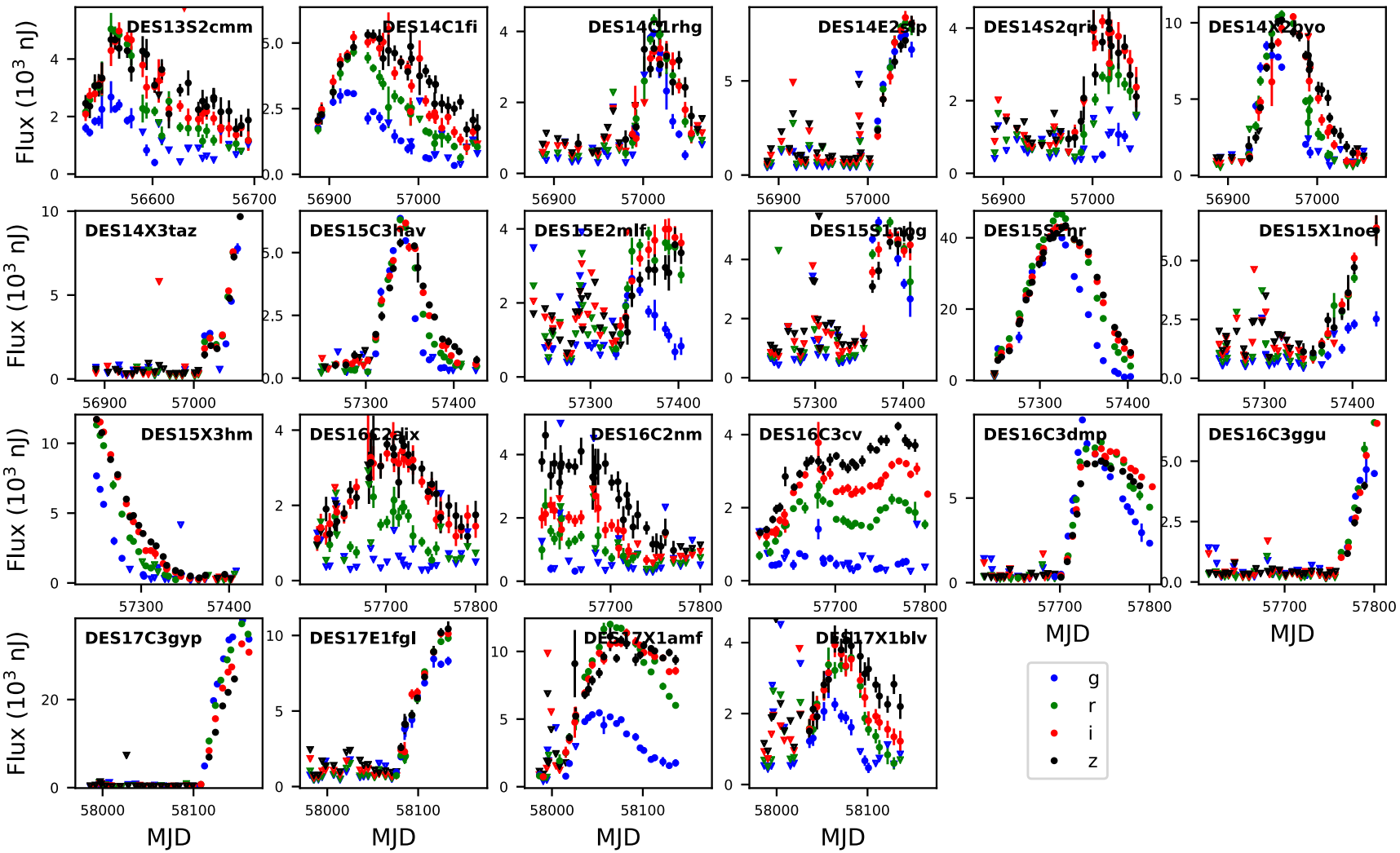

Figure 3.1: Thumbnail multicolour lightcurves of the 22 spectroscopically confirmed SLSNe from DES-SN. Downward facing triangles indicate 5σ upper limits. This is the largest sample of spectroscopically classified SLSNe out to $z < 2$ that exists. The objects exhibit a large degree of photometric diversity. See Figure 3.5 for larger versions with absorbed black body fits.

diversity in their lightcurves (Figure 3.1). The rest frame rise times span a wide range, with some objects peaking as quickly as 12 days, and others taking nearly 50 days to reach maximum (Angus et al., 2019). There are also discontinuities in some lightcurves, with rebrightening events at small temporal scales (e.g. DES16C3dmp), or long scales (e.g. DES16C3cv).

In addition, three SLSNe have lightcurves consistent with a pre-cursory peak at early times (DES14X3taz, DES15S2nr and DES15C3hav). These 'prebumps' have been observed in other SLSNe (Moriya et al., 2015; Piro, 2015; Smith et al., 2016; Kasen et al., 2016; Vreeswijk et al., 2017), and it has been suggested that they may be ubiquitous within the SLSN-I population (e.g. Nicholl & Smartt, 2016). However, Angus et al. (2019) used a Monte Carlo method to confidently rule out the presence of prebumps in 10 of the 22 objects.

3.1.2 Sample distributions

The DES SLSN sample objects were spectroscopically confirmed in the redshift range $0.22 < z < 1.99$. The redshift distribution of the DES SLSN sample is shown in Figure 3.2. At low redshifts, the number of SLSNe discovered grows with the comoving volume element of the Universe, as expected if all SLSNe in that volume were detected (although perhaps a steeper distribution may be expected due to an increasing cosmic SFH). Above $z \sim 0.6$, the number declines due to the inverse square law, i.e. fainter SLSNe fell below the detection limit of DECam, and the detection efficiency declines with redshift. At $z \sim 1.8$, another peak is seen. This peak includes DES15E2mlf and DES16C2nm, two of the highest z SNe of any type which have been spectroscopically classified. As described above, DES15E2mlf was discovered serendipitously under the program for nearby SNe Ia, whereas DES16C2nm was intentionally targeted as a high redshift SLSN candidate.

The luminosity function of the DES SLSN sample is shown in Figure 3.3, and is compared to the luminosity function of objects from the literature. The unweighted observed luminosity distributions are also shown in both

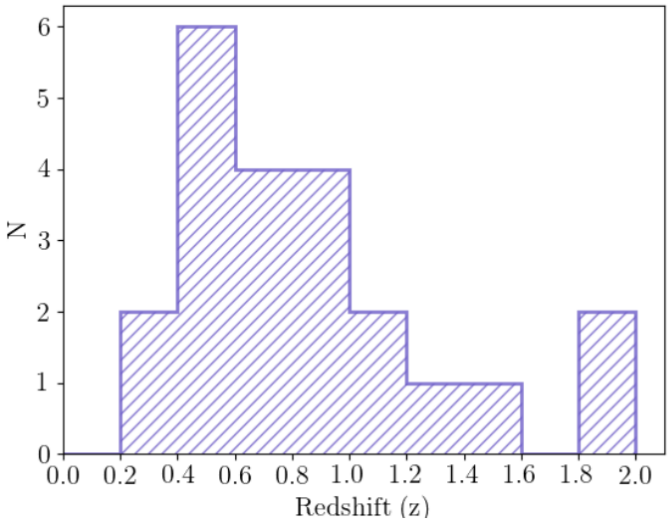

Figure 3.2: The redshift distribution of the spectroscopically classified DES-SN SLSN sample. The objects at $z \sim 2$ are the highest redshift spectroscopically confirmed SNe of any type as of June 2019. *Figure credit:* Angus et al. (2019).

cases, although these are not a realistic representation of the true population properties as they suffer from intrinsic Malmquist bias (fainter objects were not detected at high redshift, while brighter objects were). The volume over which a SN is detectable by a magnitude limited survey is a function of the brightness of the SN. Therefore, to account for the Malmquist bias, the number density in the luminosity function was weighted by the maximum volume, $V_{\rm max}$, over which a given SN is detectable. This accounted for the Malmquist bias in the luminosity function, and the $1/V_{\rm max}$ luminosity function is therefore a better representation of the underlying distribution of the population.

In Figure 3.3 a limiting magnitude of $m_{\rm R} \sim 23.5$ was used to compute $V_{\rm max}$, which represents the depth achievable with 1 hour of observing time with the spectroscopic facility VLT/X-Shooter under good conditions. The literature sample shown in the lower panels was retrieved from all published events at the time of writing that met the criteria: (1) classified as a SLSN-I; (2) observed in a minimum of three photometric bands; (3) five epochs of data in each of those bands.

Gal-Yam (2012) first defined SLSNe as SNe which have a peak magnitude brighter than $M < -21$ in any band. The discovery of SNe with $M > -21$, but with similar spectrophotometric properties to SLSNe, for example in the recent surveys PTF (De Cia et al., 2018) and Pan-STARRS (Lunnan et al., 2018) has strongly disfavoured this arbitrary magnitude limit. Meanwhile, the combination of the depth and the precision of DES photometry has permitted the most underluminous SLSN to be discovered, with $M_{\rm i} = -19.34$ (DES14C1rhg).

3.2 Synthetic lightcurves

Volumetric rate measurements of SNe are defined as the number of SNe per unit volume per unit time (i.e. how many SNe explode in a given cosmological volume per year). Therefore, rate calculations require both a well defined

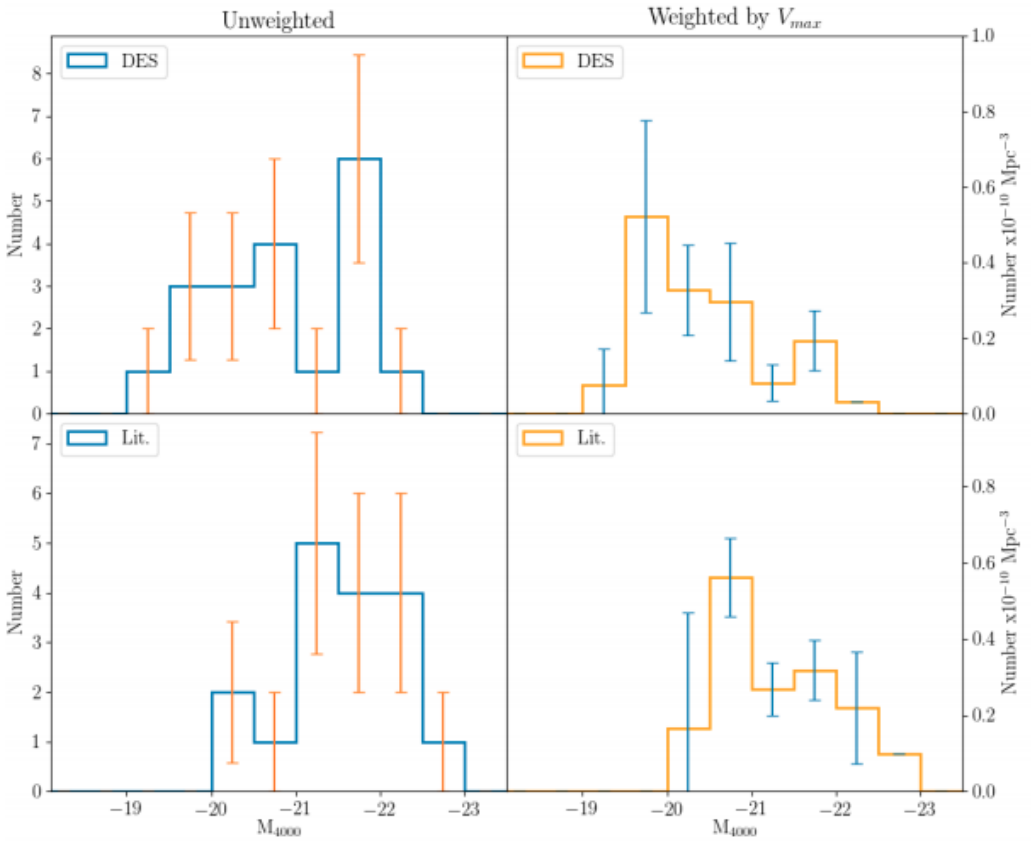

Figure 3.3: SLSN-I luminosity functions. Top panels show distributions of objects from DES-SN, while bottom panels show literature events. The left hand panels show the unweighted luminosity function, while the right hand panels show the luminosity functions weighted by the maximum volume over which the individual objects could have been observed, correcting for Malmquist bias. *Figure credit:* Angus et al. (2019).

survey volume and a well defined survey time. In this section I will describe the method I use to achieve this, including modelling the SLSN sample, and using these models to simulate synthetic lightcurves that are representative of the observed sample of SLSNe in DES. These simulations allow for the determination of the photometric completeness of the DES-SN survey for SLSNe as a function of redshift and explosion date.

Naively, I might have chosen to use the magnetar model to simulate the SLSN sample. However, Angus et al. (2019) have shown that the magnetar model does not produce a satisfactory fit to 8 of the DES SLSNe. Furthermore, I stress here that I did not attempt to model the complex astrophysics of these explosions, but rather to approximate the peak brightness and duration of the lightcurves in order to estimate the limiting redshift and explosion date to which the DES-SN survey could have detected the lightcurves. This required the simulation of millions of synthetic lightcurves (Section 3.3). For this reason, I have chosen to use a model that is less computationally intensive than the magnetar model, as detailed in Section 3.2.1.

To compute a volumetric rate, both the effective volume and effective duration of the survey must be well defined, which in consequence means that the peak brightness and explosion date of the SNe in the model fits must also be well constrained. To facilitate this, I have chosen to reject objects whose peak was not observed by DES. This reduced the spectroscopic sample to 14 SLSNe with good photometric coverage. These 14 SLSNe are modelled in the following section.

3.2.1 Absorbed black body model

I assumed a linearly expanding and linearly cooling spherical black body model similar to Howell et al. (2013). I modelled the radius $R(t)$ and tem-

perature $T(t)$ evolution of the photosphere as,

$$R(t) = R_0 + \frac{dR}{dt}\, t, \tag{3.1}$$

$$T(t) = T_0 - \frac{dT}{dt}\, t, \tag{3.2}$$

where R_0 is the initial radius, dR/dt is the constant photosphere velocity, T_0 is the initial temperature, dT/dt is the constant cooling rate, and t is the rest frame time since explosion.

Constructing the SED

To find the observed spectral energy distribution (SED) implied by this model, I began with Planck's law of black body radiation (Planck, 1900) as a function of wavelength,

$$B_\lambda(\lambda, t) = \frac{2hc^2}{\lambda^5} \left[\exp\left(\frac{hc}{\lambda k_B T(t)} \right) - 1 \right]^{-1}, \tag{3.3}$$

which gives the spectral radiance B_λ (power per unit surface area per unit wavelength) as a function of the wavelength λ and photosphere temperature $T(t)$, where h, c and k_B are the Planck constant, speed of light, and Boltzmann constant respectively.

To find the spectral flux density $F_\lambda^{\rm rest}(R)$, the radiance B_λ is multiplied by the surface area of the photosphere,

$$F_\lambda^{\rm rest}(\lambda, t) = 4\pi R^2(t)\, B_\lambda(\lambda, T)\,. \tag{3.4}$$

The final step to compute the observed SED, $F_\lambda^{\rm obs}$, was to shift the rest frame SED, $F_\lambda^{\rm rest}$, to the observer frame,

$$F_\lambda^{\rm obs}(\lambda_{\rm obs}, t_{\rm obs}) = F_\lambda^{\rm rest}(\lambda_{\rm rest}, t_{\rm rest})\, \frac{1}{4\pi d_{\rm L}^2}\, \frac{1}{1+z}, \tag{3.5}$$

where the factor $1/(4\pi d_{\rm L}^2)$ gives the fraction of the total emitted flux which reaches the observer at a luminosity distance $d_{\rm L}$, and the factor $1/(1+z)$ corrects for the cosmological expansion of the spacetime through which the

photons have travelled. Cosmological expansion is also accounted for in wavelength, $\lambda_{\rm obs} = (1+z)\,\lambda_{\rm rest}$, and time $t_{\rm obs} = (1+z)\,t_{\rm rest}$.

This simple model allowed for the construction of 'perfect' black body SED sequences, $F_\lambda^{\rm obs}(\lambda_{\rm obs}, t_{\rm obs})$, with the intent of reproducing the observed lightcurves of the DES SLSNe. However, SLSN SEDs are known to undergo significant flux absorption from metals in the ejecta (Mg II, C II, Ti III, Si III, C III, Fe III, Co III, Mazzali et al. 2016), which cause the observed SED to deviate from a perfect black body at wavelengths of $\lambda \leq 2800$ Å. Prajs et al. (2017) accounted for this effect by adopting a flux absorption template based on the observed spectra of iPTF13ajg, a SLSN-I at $z = 0.7403$ (Vreeswijk et al., 2014). iPTF13ajg was one of the only SLSNe-I with spectral coverage in the UV at the time of their study.

I followed their method, using the more recently discovered Gaia16apd at $z = 0.1018$ (Yan et al., 2017). This nearby SLSN-I was observed spectroscopically by the Hubble Space Telescope (HST) at wavelengths down to $\lambda \geq 1000$ Å. Because of the far UV spectral coverage, the observed spectrum was useful for UV spectral modelling of SLSNe, which dominates the optical photometry of high-z SLSNe.

I used 3 spectra from the Hubble Space Telescope (HST) Cosmic Origins Spectrograph (COS; Green et al. 2012), the HST Space Telescope Imaging Spectrograph (STIS; Woodgate et al. 1998), and the Double Beam SPectrograph (DBSP; Oke & Gunn, 1982) on the 200 inch telescope at the Palomar Observatory (P200). The far- and near-UV spectra from HST-COS and HST-STIS were taken on the same night, while the optical spectrum from P200 was taken 2 nights earlier, and I assumed that there was negligible spectral evolution in Gaia16apd over this period. I combined and smoothed these spectra in bins of 5Å. I fit a perfect black body to the observed spectrum in regions where there was little to no flux absorption. By then taking the ratio between the black body fit and the observed spectrum, I modelled the absorption strength as a function of wavelength (see Figure 3.4).

The ejecta of SLSNe-I are likely to contain a different amount of met-

als from object to object, which will lead to different degrees of UV flux absorption. I added an additional multiplicative 'line-blanketing' absorption parameter $0 \leq l_B \leq 1$ to account for object-to-object variations in the overall absorption strength at $\lambda \leq 2800$ Å.

The final step in creating the model SED sequences was to correct for Milky Way dust absorption. I adjusted the SED sequences described above using $E(B-V)$ values from the Galactic dust maps of Schlegel et al. (1998) and Schlafly & Finkbeiner (2011). These are computed for each of the DES fields. I adopted $R_V = A_V/E(B-V) = 3.1$ and the Cardelli extinction law (Cardelli et al., 1989). Host galaxy extinction is generally assumed to be negligible as SLSNe explode in faint, metal-poor dwarf galaxies (e.g. Lunnan et al., 2018). While this may be a somewhat coarse assumption, modelling of dwarf galaxy properties on a case-by-case basis is beyond the scope of this thesis, particularly as the host galaxies were not detected in the single-epoch DES images for 42% of the spectroscopic SLSN sample.

In summary, in this section I have created time evolving SED sequences (i.e. flux density as a function of wavelength and lightcurve epoch). Next, I convolved these with the DES filter transmission functions (Figure 2.2) to obtain synthetic lightcurves.

Building a 'perfect' lightcurve

The AB magnitude observed in some filter with transmission function $R(\lambda)$ is given by a convolution of $R(\lambda)$ with the incident SED, $F_\lambda^{\rm obs}(\lambda)$, normalised by a 'zero point' (Hogg et al., 2002),

$$m_{\rm AB} = -2.5 \log_{10} \left[\frac{\int_0^\infty F_\lambda^{\rm obs}(\lambda)\, R(\lambda)\, \lambda\, d\lambda}{\int_0^\infty S_\lambda(\lambda)\, R(\lambda)\, \lambda\, d\lambda} \right], \tag{3.6}$$

where the zero point is related to the reference flux in wavelength space, $S_\lambda(\lambda)$. In the AB system, the reference flux is flat in frequency space, $S_\nu = 3631\,{\rm Jy}$, and is related to $S_\lambda(\lambda)$ by,

$$S_\lambda(\lambda) = \frac{c}{\lambda^2} S_\nu. \tag{3.7}$$

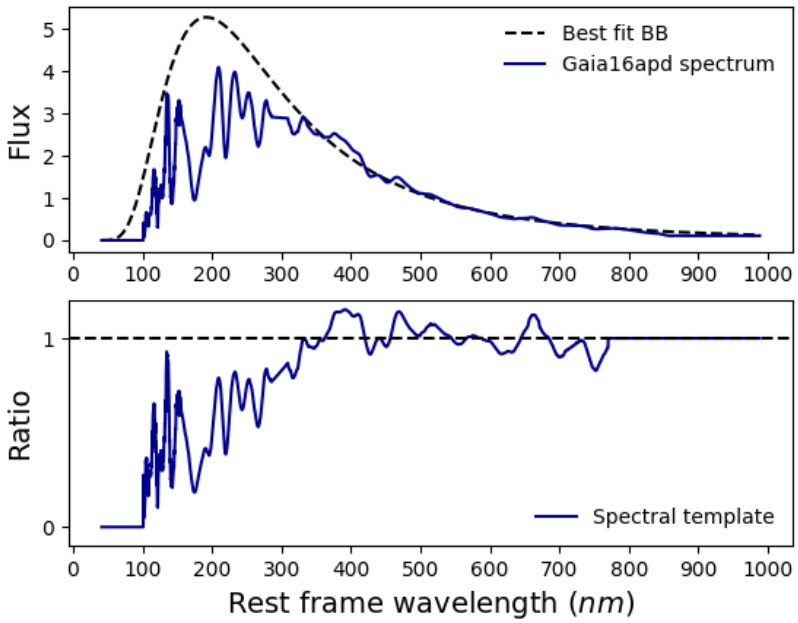

Figure 3.4: The construction of the spectral template used to mitigate the effect of UV metal absorption. The top panel shows the best fit black body curve to continuum regions of the observed Gaia16apd spectrum. The bottom panel shows the ratio of the two, or the absorption strength, a multiplicative function which I used to adjust the SEDs (at $\lambda < 2800$Å) of the black body fits to DES-SN SLSN-I lightcurves.

I used the SED sequences from Section 3.2.1 to compute the observed magnitude as a function of time in all 4 DES-SN bands (*griz*). In the next section I will fit these model lightcurves to the observed photometry for the simulations of Section 3.3.

3.2.2 Reproducing SLSN lightcurves

I fit this model to each of the 14 of 22 spectroscopically classified SLSNe from DES for which the detection season contains the peak. I utilised a log likelihood maximisation routine in `python`, the results of which are shown in Figure 3.5, with best fit values given in Table 3.1.

Synthesizing observed lightcurves

While I have created 'perfect' lightcurves, with flux values determined to ostensibly infinite precision, these are not a realistic representation of the lightcurves that have been observed by DES-SN. There exists stochastic variability in the observed flux values which must be modelled in the simulated lightcurves. Here, I briefly describe the method used to model the uncertainty and stochasticity of the synthetic fluxes.

In order to synthesize realistic observed lightcurves, the flux uncertainty on each epoch must be modelled. To achieve this, I used the code `lcsim`[1] developed by Szymon Prajs (University of Southampton). In brief, the code works as follows. The flux uncertainty is a function of the sky background and the noise due to thermal energy releasing anomalous electrons on the CCD. `lcsim` retrieves the sky background signal, CCD noise, CCD gain (i.e. how many electrons were released on the CCD per incident photon), and the effective zero point of the photometry on a given night from DES observing logs.

The total flux uncertainty $\sigma_{\rm F}$ in an observed aperture is the quadrature sum of the flux uncertainty of the astrophysical source of interest $\sigma_{\rm SN}$, the

[1] https://github.com/SzymonPrajs/lcsim

sky background flux error $\sigma_{\rm sky}$, and the CCD noise error $\sigma_{\rm CCD}$,

$$\sigma_{\rm F} = \sqrt{\sigma_{\rm SN}^2 + \sigma_{\rm sky}^2 + \sigma_{\rm CCD}^2}\,. \tag{3.8}$$

Once these flux uncertainties are simulated, the next step is to randomly draw a new synthetic flux value from a Gaussian distribution centered on the perfect model flux with a standard deviation of $\sigma_{\rm F}$. This gives a new synthetic 'observed' flux, with the uncertainty $\sigma_{\rm F}$ carried over.

I carried out this so-called flux smearing for every simulated epoch, and was thereby able to model the stochastic variability of real astronomical observations in the synthetic lightcurves. This process allows me to empirically define the ability of DES-SN to detect SLSN lightcurves (i.e. the photometric efficiency) in the next section.

3.3 Simulations

The objective of this section is to compute the detectability of SLSNe in DES-SN over a grid of redshift and explosion date, and thereby find the regions in this redshift-explosion date space in which the DES-SN search for SLSNe is photometrically complete. This was achieved by simulating the models shown in Figure 3.5 across redshift and observing time.

The photometric efficiency as a function of redshift is sensitive to the peak brightness of the SLSNe, as intrinsically faint objects are more difficult to detect at high redshift. Therefore, a trade off exists between selecting a redshift range that contains a significant fraction of the spectroscopic sample (to reduce the statistical error on the rate) and setting a lower magnitude limit such that the photometric efficiency at intermediate redshift is well constrained.

In a revision to their original criterion, Gal-Yam (2018) found that a peak absolute magnitude of $M = -19.8$ tentatively separated SLSNe from the dimmer population of SNe Ic. I enforced this criterion on the sample of spectroscopic objects, and DES14C1rhg and DES15C3hav were rejected

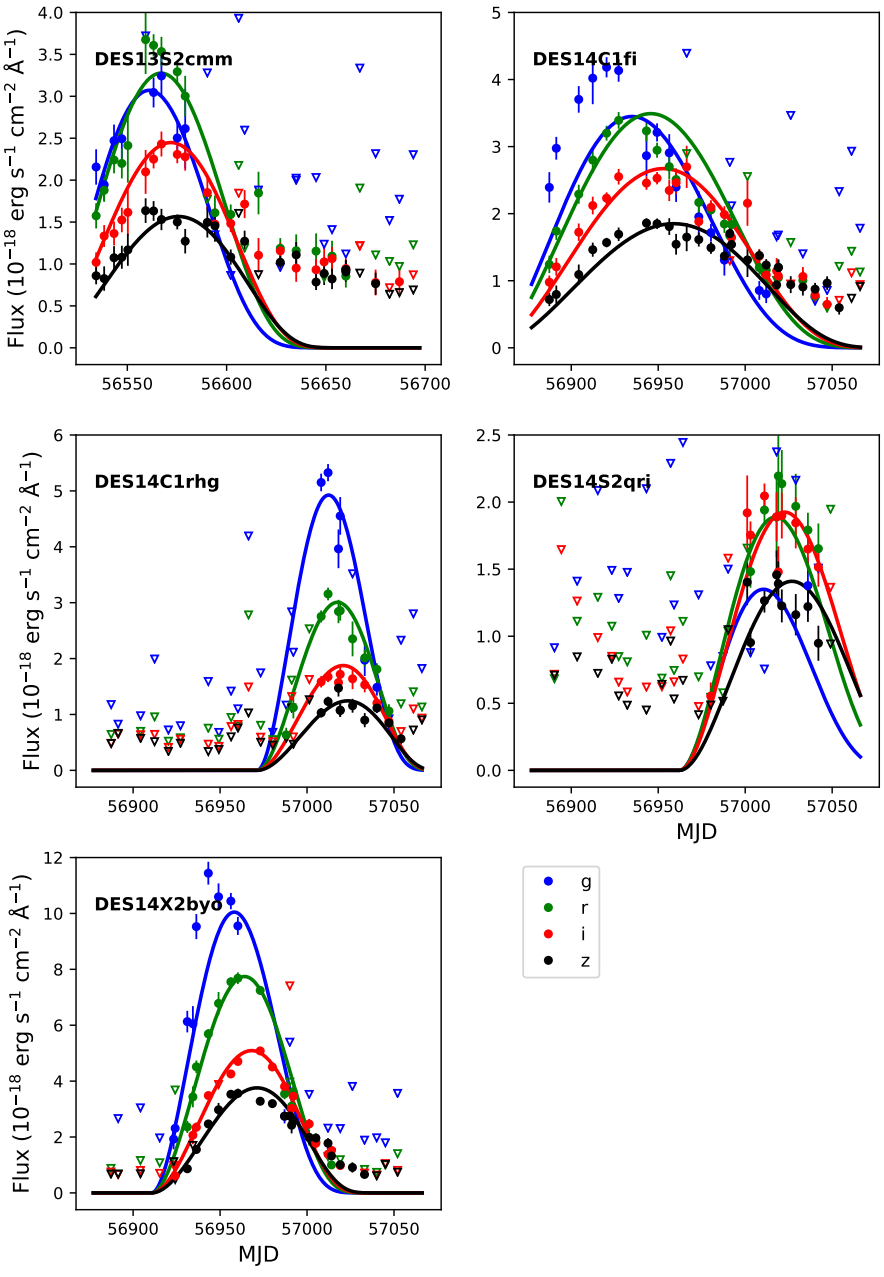
DES13S2cmm
DES14C1fi
DES14C1rhg
DES14S2qrj
DES14X2byd
Flux (10^{-18} erg s^{-1} cm^{-2} Å^{-1})
MJD
g
r
i
z

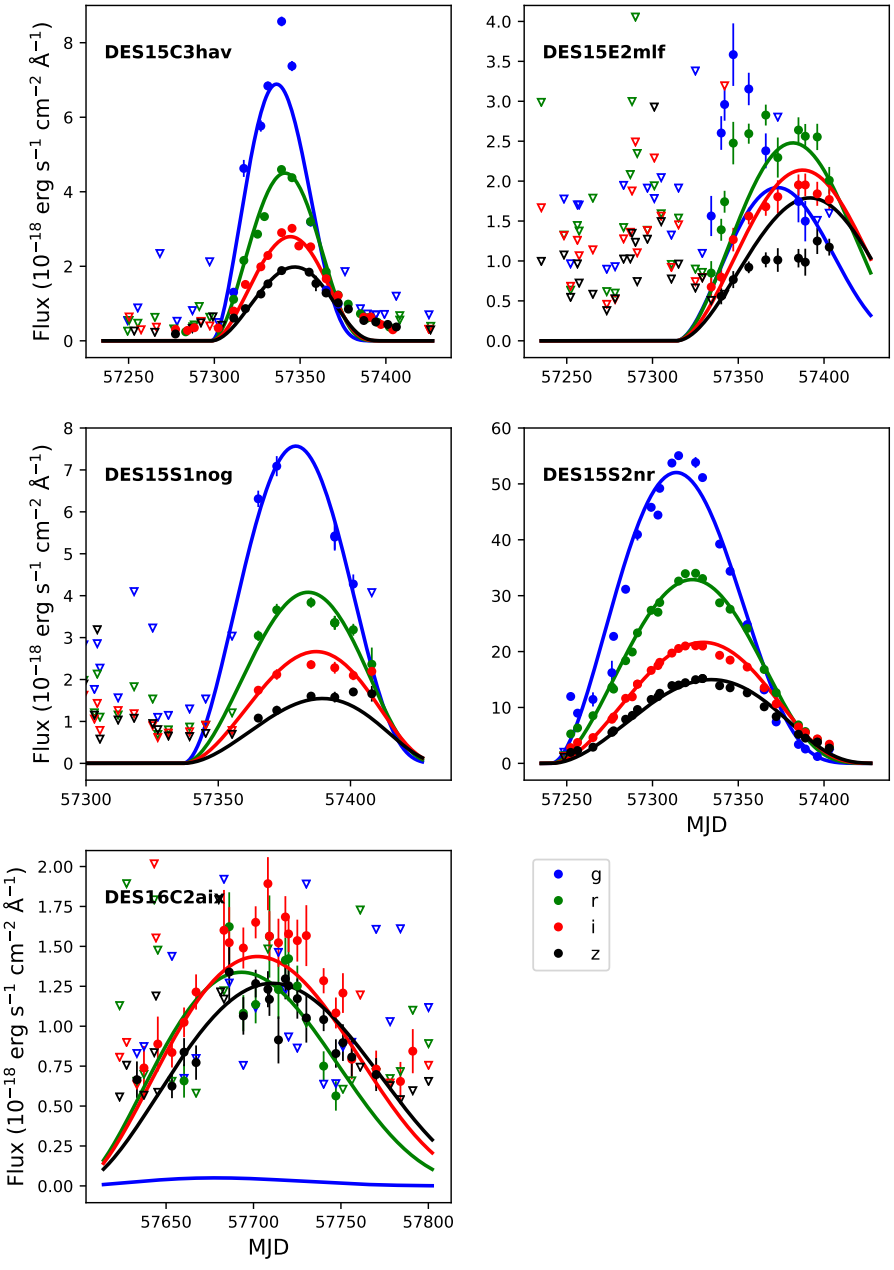
DES15C3hav
DES15E2mlf
DES15S1nog
DES15S2nr
DES16C2aix
Flux (10^{-18} erg s^{-1} cm^{-2} Å^{-1})
MJD
g
r
i
z

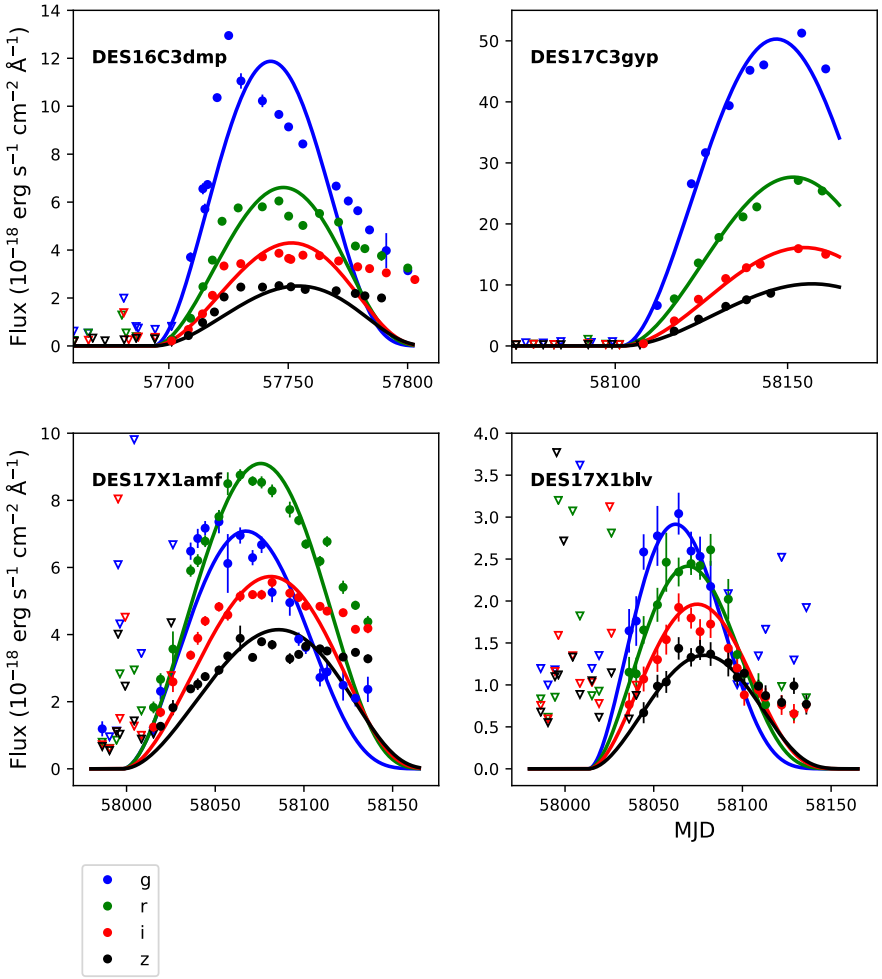

Figure 3.5: Absorbed black body fits to spectroscopically confirmed SLSNe whose peak was captured by the DES observing season. For some of the SLSNe at high redshift (DES14C1fi, DES15E2mlf), the fits did not accurately capture the colour evolution. However, DES14C1fi, DES14S2qri, DES15E2mlf, and DES16C2aix were not included in my volumetric rate calculation (Chapter 5) due to their high redshift.

Name	$t_{\rm exp}$ (MJD)	R_0 (10^{13} cm)	dR/dT (10^{13}cm/day)	T (10^4 K)	dT/dt (10^2 K/day)	$l_{\rm B}$	χ^2/d.o.f
DES13S2cmm	56469	4.890	0.726	1.382	0.706	0.99	3.20
DES14C1fi	56876	4.890	1.418	2.535	2.715	1.00	16.82
DES14C1rhg	56984	4.867	0.802	1.905	2.830	1.00	2.34
DES14S2qri	56970	4.865	3.308	1.906	2.984	1.00	3.10
DES14X2byo	56911	4.869	1.557	2.623	3.576	0.84	9.95
DES15C3hav	57299	4.890	0.505	2.159	2.610	0.01	23.21
DES15E2mlf	57299	4.887	1.421	2.895	2.649	0.88	2.71
DES15S1nog	57327	4.867	0.500	2.206	1.951	0.00	2.84
DES15S2nr	57247	4.890	0.820	1.434	0.843	0.80	14.74
DES16C2aix	57618	4.890	1.749	1.349	0.969	0.10	1.55
DES16C3dmp	57689	4.857	0.768	2.150	1.959	1.00	60.06
DES17C3gyp	58106	4.832	1.596	2.666	3.692	1.00	25.05
DES17X1amf	57985	4.861	1.117	2.397	1.837	0.62	3.52
DES17X1blv	58009	4.831	1.066	1.509	1.344	1.00	1.16

Table 3.1: Fit parameters to the 14 spectroscopic SLSNe-I whose peak was detected by DES-SN. My model was not intended to account for the lightcurve anomalies present in some objects, and despite the large reduced χ^2 in these cases, I considered these fits to be representative of the detectability of SLSNe-I in DES. The derived black body temperatures are comparable to those found by Lunnan et al. (2018) for the Pan-STARRS sample ($1 - 2.5 \times 10^4$ K).

from the sample. The remaining 12 spectroscopic SLSNe are used for the simulations in this section.

There was some stochastic variability within an object's synthetic lightcurve due to the uncertainty in the true flux values inferred from the observations. Thus whether an object was detected at a given redshift or explosion time is also stochastic as it depends on the synthetic flux values. I have therefore chosen a statistical approach. I simulated 100 objects at every point on the redshift-explosion date grid. The fraction of the total that were detected was taken as the photometric efficiency. The photometric efficiency is a measure of the probability of a successful SLSN detection as a function of redshift and explosion date. This gave a grid of photometric efficiency values in redshift-explosion date space for each object.

The model of Section 3.2.1 contained 7 free parameters: the explosion date $t_{\rm exp}$, the redshift z, the initial photospheric radius R_0, the (constant) photospheric velocity dR/dt, the initial temperature T_0, the (constant) cooling rate dT/dt, and the absorption parameter $l_{\rm B}$. To simulate lightcurves I fixed the parameters describing the physical explosion, and iterated over the redshift z and explosion date $t_{\rm exp}$. Each object was simulated in each of the 10 DES fields.

The redshift axis was defined between $0.0 < z \leq 3.0$ in steps of $\Delta z = 0.05$. The explosion date axis was defined between $56334 \leq t_{\rm exp} \leq 58166$ (i.e. from 200 days before the first exposure to the last exposure of DES-SN), with a step size $\Delta t_{\rm exp} = 10$ days. I simulated 100 realisations per object per pair of redshift and explosion date values per field. A *single epoch* was labelled as detected if:

- The signal to noise ratio at this epoch, SNR ≥ 5.
- The flux at this epoch was less than the saturation value of the camera. In electron counts, the saturation limit is $135,000\mathrm{e}^-$.

The signal to noise was computed with the `lcsim` code from the observing conditions (PSF, sky brightness, weather), which were recorded and logged

for each night. The number of detected epochs defined whether or not a *lightcurve* was detected. Lightcurves were detected if:

- ≥ 5 epochs were detected ($\geq 5\sigma$) in at least 3 filters (≥ 15 total detections).
- ≥ 1 epoch was detected before maximum light in at least 2 filters.
- ≥ 1 epoch was detected after maximum light in at least 2 filters.

In total I simulated 14 SLSNe $\times$ 100 realisations $\times$ 60 redshift bins $\times$ 184 explosion date bins $\times$ 10 fields = 154,560,000 synthetic lightcurves. This computationally intensive calculation was carried out in parallel on the local high performance computing cluster SCIAMA. Each grid realisation constituted a single $\sim$100 minute computation. These jobs were queued, with 100 running in parallel at any one time. An example photometric efficiency grid for DES14X2byo in the shallow C1 field is shown in Figure 3.6.

To compute the regions of the redshift-explosion date grid for which DES-SN is photometrically complete *for all SLSNe that were simulated*, I first found the contours which bound the regions of photometric completeness for the individual SNe. The regions in which DES-SN was photometrically complete for all SNe were then the intersections of these contours. These intersections are shown in Figure 3.7 (one set per field). To compute the intersections I used the `python` library `Shapely`[2].

Given the area of the DECam footprint and assuming some cosmological parameters, the redshift axis is transformed to a comoving volume axis in Chapter 5, and the area of the photometrically complete regions in this explosion date-volume space constitutes the effective volume-time for my rate calculation.

Error analysis

To estimate the systematic error on the area of the photometrically complete regions, I considered three primary sources: (1) the contribution from the

[2]https://shapely.readthedocs.io/

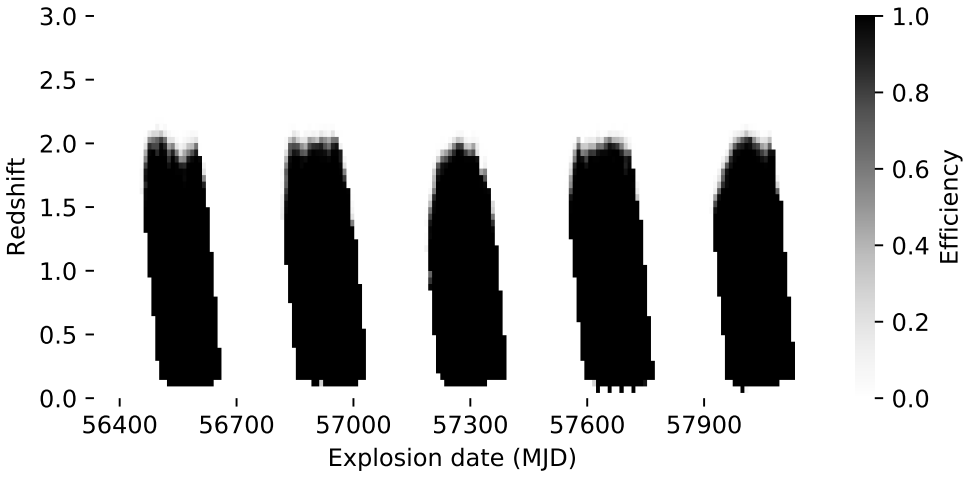

Figure 3.6: Results of the photometric efficiency simulations for DES14X2byo in the shallow field C1. The five shaded areas represent a high probability of detection within the five observing seasons of DES-SN. The photometric completeness is limited by (1) saturation at low redshift; (2) whether or not the peak was detected at the temporal edges and (3) a deteriorating signal to noise ratio at high redshift.

peak flux estimation of the model fits; (2) the contribution from the peak time estimation of the model fits and; (3) the contribution from the binning resolution.

It was clear from visual inspection of the model fits in Figure 3.5 that the g band flux was significantly underestimated in some cases. The criteria defined above required that a lightcurve must be 'observed' in three filters to be considered detected. At high redshift, the g band is the first filter to drop below the signal to noise limit of the photometry, as objects get redder with cosmological distance. Therefore an underestimated g band flux did not significantly affect the photometric completeness. Contributions to the peak flux uncertainty from other bands were not considered, as the r, i, and z bands were adequately represented by the model for the objects that are included in the rate computation.

The second detection criterion requires that the peak of the lightcurve must have been detected. The peak time of the lightcurve was derived from the maximum brightness of the model fits. The error on the peak time cannot be better than the nominal cadence of the DES-SN survey (7 days), as it is these epochs that constrained the fit. I computed the mean width in explosion date of the individual photometrically complete regions; 140 days. I estimated the contribution of the peak time error to the uncertainty on the photometrically complete regions as $7/140 = 5\%$.

Finally, the binning resolution contributed an error given by the bin length $\Delta z = 0.05$ in the vertical direction, and the bin width $\Delta t_{\rm exp} = 10$ days in the horizontal direction. Taking the mean region height in redshift gave an error contribution $0.05/0.82 = 6\%$. Taking the mean region width in explosion date gave an error contribution in the horizontal direction of $10/140 = 7\%$. This latter resolution of the explosion date axis absorbed the effect of any variations in the peak time within the uncertainty given above. Therefore, I calculated the quadrature sum of the two error contributions from the binning resolution to find a total error on the area of the photometrically complete regions of 9%. While this was a rough estimate of the

systematic uncertainty, I note here that my volumetric rate measurement is statistics limited; more details are given in Chapter 5.

3.4 Conclusion

In this chapter I have presented the spectroscopically classified sample of SLSNe from DES. I described the spectroscopic observations made to classify these objects, and described their lightcurves including anomalous behaviours. Atypical features in these lightcurves appear relatively common compared to other samples from PTF (De Cia et al., 2018) and Pan-STARRS (Lunnan et al., 2018).

I described the statistical distributions of these objects, specifically the redshift distribution and the luminosity function. The redshift distribution contained the highest redshift SN of any type which has been spectroscopically classified (DES16C2nm). The luminosity function contained the most underluminous SLSN yet observed (DES14C1rhg). The luminosity function is in further contradiction to the arbitrary magnitude threshold for SLSNe of $M < -21$ defined in Gal-Yam (2012). The DES-SN spectroscopic sample is described in detail in Angus et al. (2019).

I detailed the model I used to represent the detectability of the SLSN sample. Taking simple linear equations for the radius and temperature evolution, I used the Planck black body function to derive SED sequences as a function of time. These SEDs were modified with an empirical absorption model to describe the UV flux absorption due to metals in the SN ejecta, and were adjusted for Milky Way extinction. Convolving these modified SEDs with the DES filter transmission functions, I was able to create 'perfect' lightcurve models. These models were fit to the observed lightcurves to obtain best fit parameters describing the SLSN sample. I then allowed for stochastic variability in the flux values by factoring in the sky background flux and anomalous thermal electrons in the CCDs, which let me recreate synthetic 'observed' lightcurves of the DES SLSNe at any redshift or explosion date.

Finally, I ran photometric simulations of the spectroscopic SLSNe whose peak was detected in the DES seasons, and that were brighter than $M_{\rm i} < -19.8$. The first step of this section was to define criteria that simulated lightcurves must pass to be classed as 'detected'. I used the best fit parameters from my absorbed black body fits to recreate the spectroscopic SLSN sample at redshifts $0.0 \leq z \leq 3.0$ and explosion dates $56334 \leq t_{exp} \leq 58166$ (MJD). I simulated 100 realisations of each object for every redshift-explosion date pair, in all 10 DES-SN fields, which allowed me to evaluate the photometric efficiency at all regions of the DES-SN observed volume and time. I selected the regions in redshift-explosion date space over which the DES-SN search was photometrically complete for all SLSNe that were simulated, and these regions will constitute the final effective volume-time for my volumetric rate computation in Chapter 5. Finally, I estimated the systematic error of these regions to be 9% by considering the uncertainty on the peak time and brightness, and the contribution from the binning resolution.

In the next chapter I will augment the spectroscopic SLSN sample by executing a deep search in the DES database of $\sim$30,000 transients to find objects for which DES-SN obtained photometry but for which it either did not obtain spectra, or the spectra had an insufficient signal to noise ratio for a classification to be made. These photometric objects will be included in my volumetric rate measurement of Chapter 5.

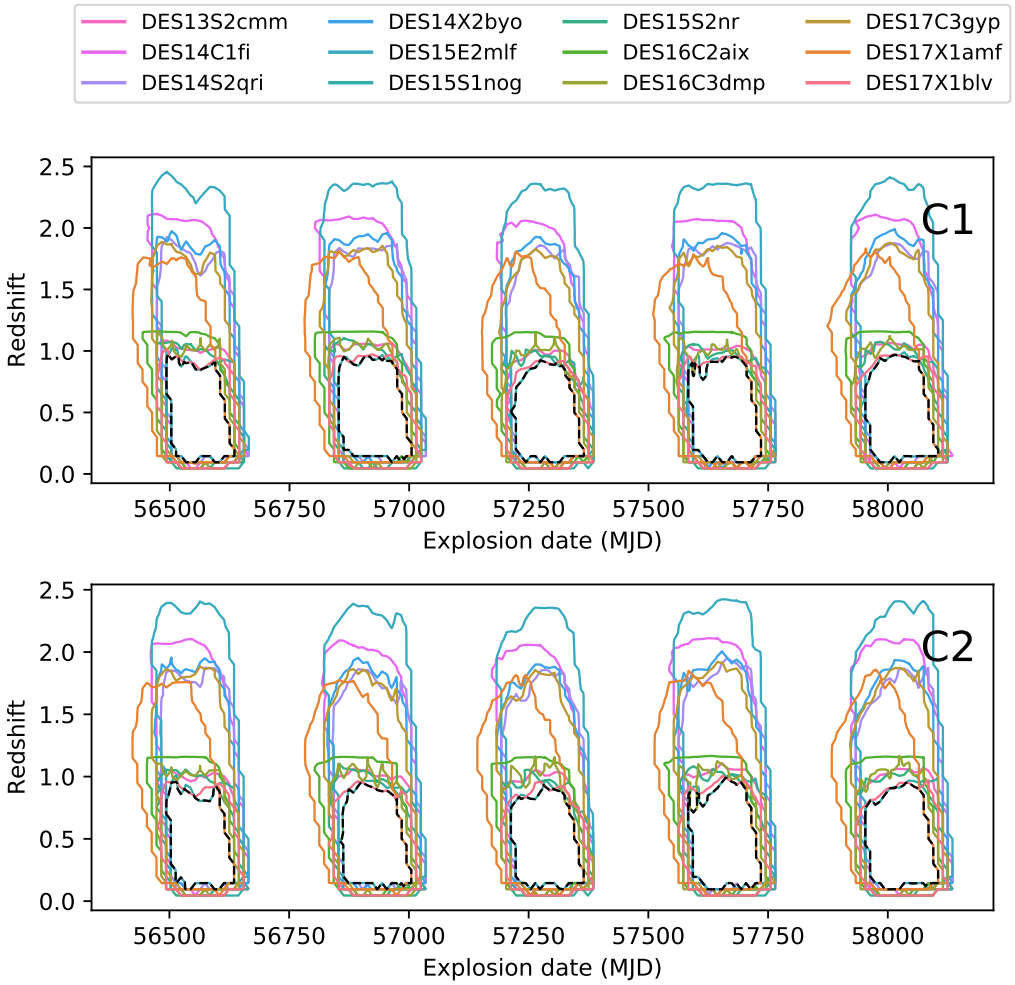

Figure 3.7: These figures show the regions of photometric completeness in redshift-explosion date space for the 12 spectroscopic SLSNe which passed my preliminary selection criteria. The coloured lines are for individual SLSNe, while the dotted black line bounds the region in which DES-SN is photometrically complete for *all* of the simulated SLSNe. These latter regions form the effective volume-time of the survey for my rate computation of Chapter 5. The first four sets of figures show shallow fields, while the final set of figures show the deep fields.

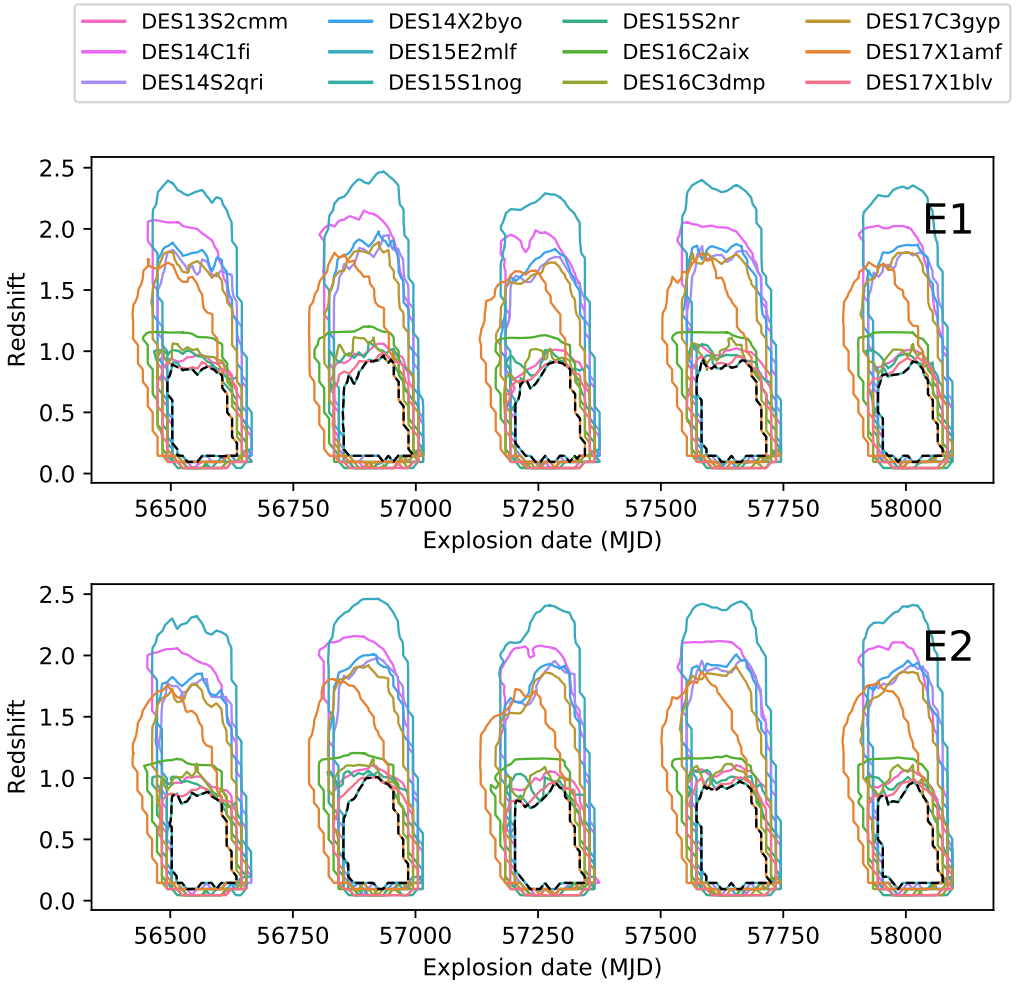
DES13S2cmm
DES14C1fi
DES14S2qri
DES14X2byo
DES15E2mlf
DES15S1nog
DES15S2nr
DES16C2aix
DES16C3dmp
DES17C3gyp
DES17X1amf
DES17X1blv
E1
E2
Redshift
Explosion date (MJD)
0.0
0.5
1.0
1.5
2.0
2.5
56500
56750
57000
57250
57500
57750
58000

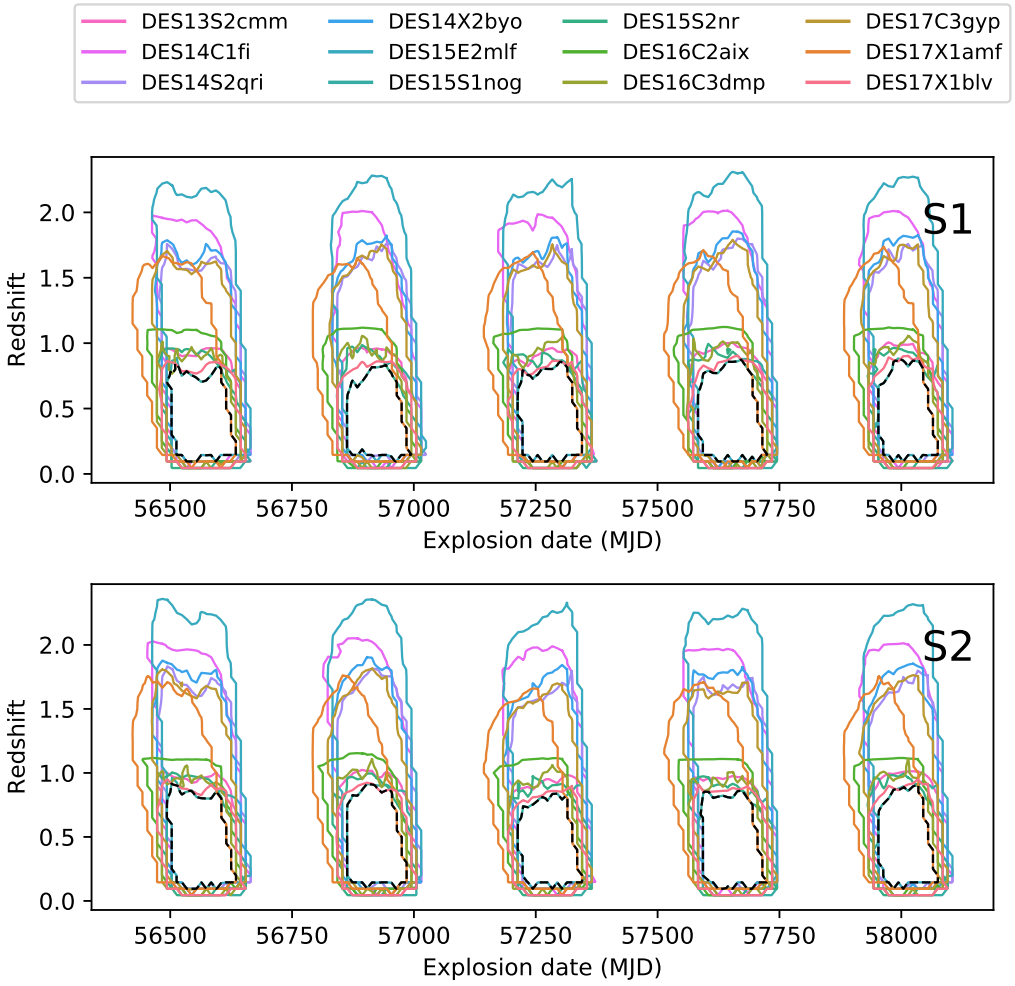
DES13S2cmm
DES14C1fi
DES14S2qri
DES14X2byo
DES15E2mlf
DES15S1nog
DES15S2nr
DES16C2aix
DES16C3dmp
DES17C3gyp
DES17X1amf
DES17X1blv
S1
S2
Redshift
Explosion date (MJD)
0.0
0.5
1.0
1.5
2.0
56500
56750
57000
57250
57500
57750
58000

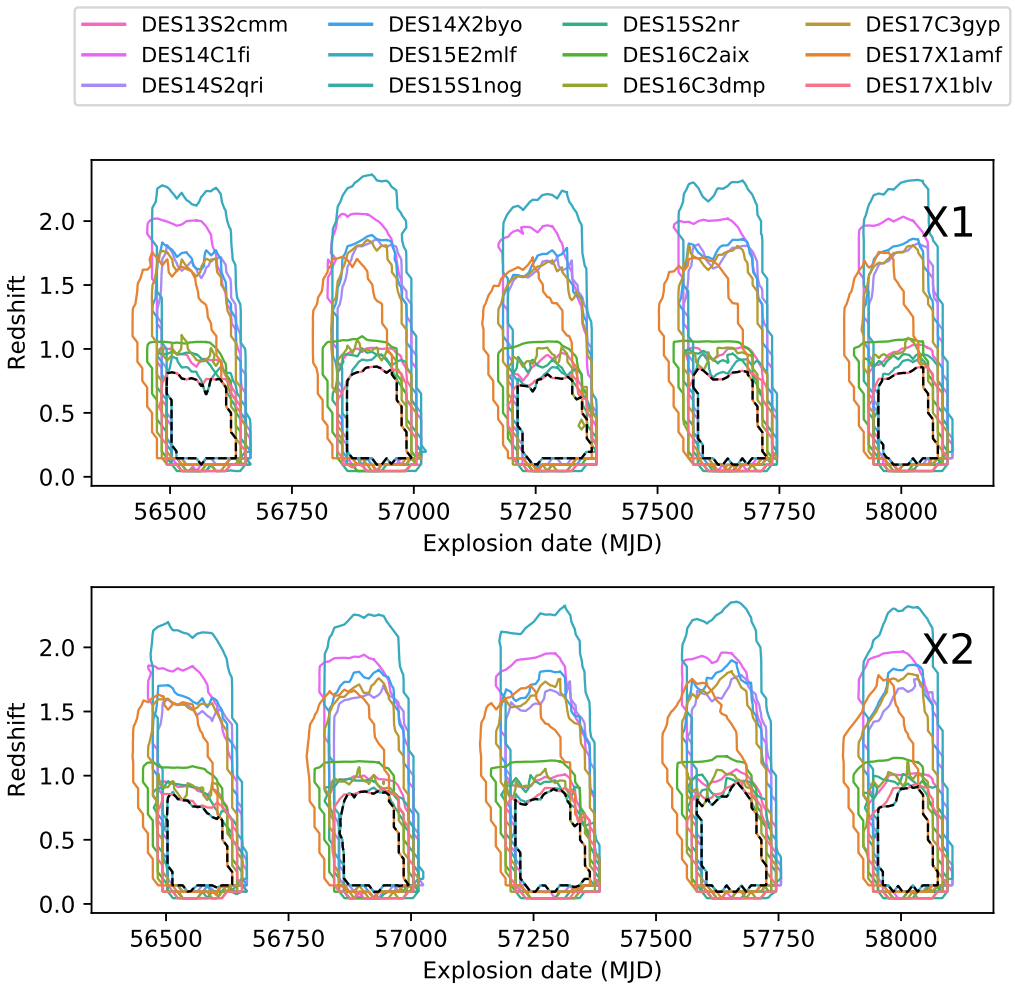
DES13S2cmm
DES14C1fi
DES14S2qri
DES14X2byo
DES15E2mlf
DES15S1nog
DES15S2nr
DES16C2aix
DES16C3dmp
DES17C3gyp
DES17X1amf
DES17X1blv
X1
X2
Redshift
Explosion date (MJD)
0.0
0.5
1.0
1.5
2.0
56500
56750
57000
57250
57500
57750
58000

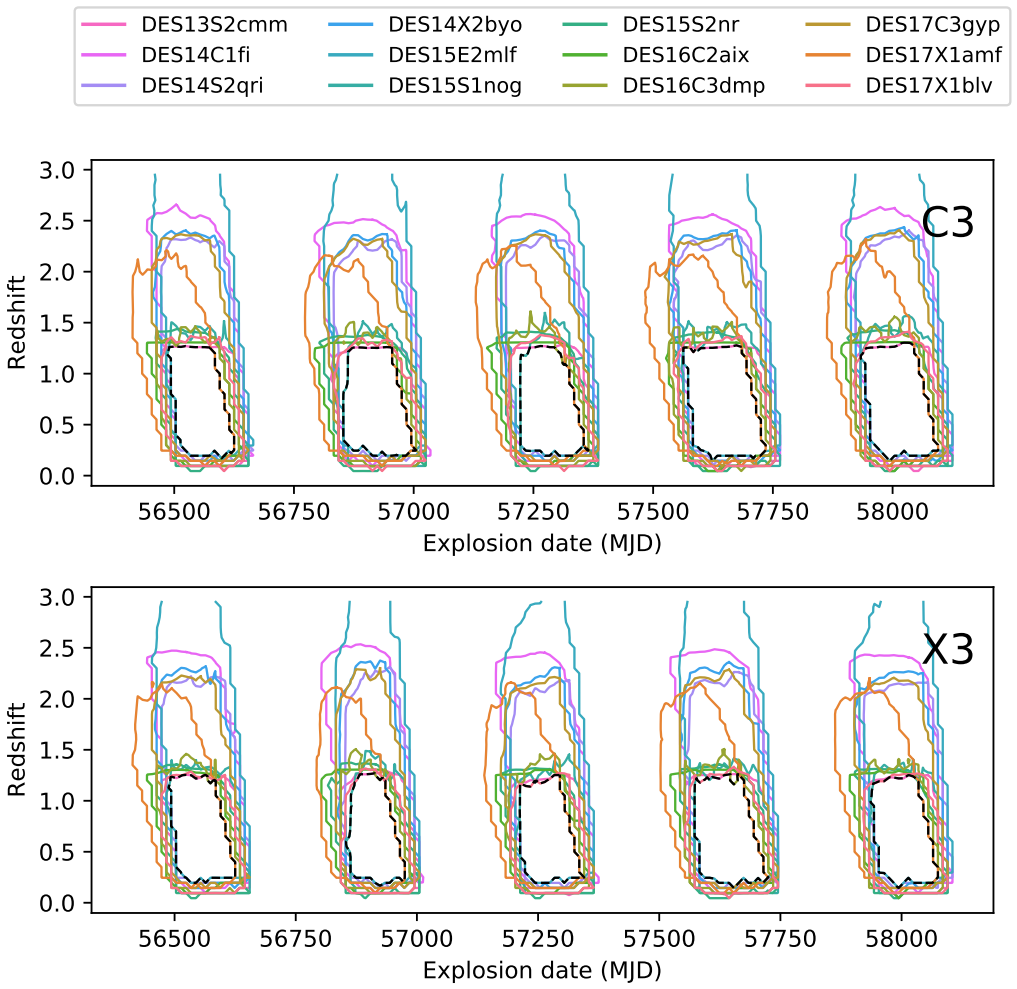
DES13S2cmm
DES14C1fi
DES14S2qri
DES14X2byo
DES15E2mlf
DES15S1nog
DES15S2nr
DES16C2aix
DES16C3dmp
DES17C3gyp
DES17X1amf
DES17X1blv
C3
X3
Redshift
Explosion date (MJD)
0.0
0.5
1.0
1.5
2.0
2.5
3.0
56500
56750
57000
57250
57500
57750
58000

Chapter 4

Photometric Search for Superluminous Candidates

The majority of the work detailed in this chapter is my own, except for; (1) the visual inspection of candidates described in Section 4.2. I led this collaborative effort, which consisted of C. Frohmaier, C. Angus, M. Smith, C. Inserra and myself and (2) the spectra in Section 4.4 were reduced by C. Angus and M.Smith. References to other works, where necessary, are given throughout.

In any magnitude limited survey, it is unfeasible to obtain spectroscopic classifications of all SNe which are photometrically detected. Observationally faint objects require long exposure times on expensive spectroscopic telescopes to obtain spectra with a sufficient signal to noise ratio for robust classifications to be made. In DES-SN, the majority of the available spectroscopic resources were designated to observations of Type Ia SNe, and the program to obtain spectra of SLSNe was therefore limited.

For a volumetric rate measurement it is essential to be able to calculate the fraction, f, of SNe from the underlying population that went undetected by the survey. The detection efficiency ϵ is related to f by,

$$\epsilon = 1 - f. \tag{4.1}$$

The total detection efficiency ϵ is the product of two parts. The first is the photometric efficiency $\epsilon_{\rm P}$. This is related by Equation 4.1 to the fraction of objects $f_{\rm P}$ from the underlying population, with observations of insufficient quality to be counted as photometrically detected, either due to temporal edge effects, a low signal to noise ratio, or a combination of both. The second is the spectroscopic efficiency $\epsilon_{\rm S}$. This is related by Equation 4.1 to the fraction of objects $f_{\rm S}$ in the photometric population for which the survey did not get spectra, or for which the spectra were of insufficient quality to obtain a secure classification. This could be due to a low signal to noise ratio or observational artefacts in the spectra.

In this chapter, I carry out a detailed search into the DES-SN photometric database stored within the DES Data Management System (DESDM, Mohr et al. 2008), and accessed using `easyaccess` (Carrasco Kind et al., 2018), a `Python` library dedicated for DES data access via `SQL` / `Oracle`. I search for SLSN candidates for which the survey obtained good photometry but no spectroscopic classification, either because no spectra were taken, or because the spectra that were taken were of insufficient quality (i.e. those objects which contribute to $f_{\rm S}$ above).

In Section 4.1, I define and justify the automated selection criteria used to drastically reduce the initial sample of $154,748$ objects. In Section 4.2 I describe the human visual inspection and vetting of the remaining 229 objects and the criteria used therein. To achieve this I led a team of both ICG and University of Southampton scientists. This resulted in a sample of 52 objects, which I will discuss in Section 4.3.

4.1 Automated selection criteria

DESDM contains all photometry which was obtained over the 5 DES-SN observing seasons. The total number of objects in the database is 154,748, including real astrophysical objects, synthetic SN Ia lightcurves used for monitoring pipeline performance, and artefacts and duplicate objects from the

difference imaging pipeline. The first step of my photometric search was to define automated selection criteria that remove the majority of obvious contaminants, while retaining SLSN candidates.

4.1.1 Initial selection

One method of characterizing the detection efficiency of objects is to insert thousands of synthetic lightcurves into raw exposures, pass these through the data pipeline, and find the fraction that is recovered at the end (e.g. Kessler et al. 2015). Within DES-SN this method was used to constrain the SN Ia detection efficiencies, and thus a significant fraction of the lightcurves in the database are these 'fake' lightcurves which do not correspond to real objects. The first criterion I imposed on the raw sample of DES-SN transients was to select all objects that had a `snfake_id = 0`, which removed all fakes.

Within the DES-SN pipeline there was also some chance that a single object will receive more than one `snid`, an ostensibly unique identifier. Duplicate objects are indicated by a value of the parameter `cand_type = -15`, and I required objects to have `cand_type > 0`.

As detailed in Chapter 2, the DES-SN pipeline used the machine learning algorithm `autoScan` (Goldstein et al., 2015) to score images based on the probability that they are astrophysical, where a score of 0 indicated an artefact and a score of 1 indicated an astrophysical object. I required lightcurves to have more than 1 epoch (in any filter) that scored better than 0.5 on the `autoScan` test.

I fed the following query to the database:

```
1 select snid from sncand where snfake_id = 0
2 and cand_type >= 0 and numepochs_ml > 1
```

which returned 31,642 of the original 154,748 objects, or 20.4%.

4.1.2 Lightcurve quality

The vast majority of objects in DES-SN are non-astrophysical noise. In order for an object to be marked as a 'transient', and given a `snid`, it must have been detected in at least 2 epochs (D'Andrea et al., 2018). This is not a strict requirement, and many non-astrophysical objects fulfill it simply via statistical fluctuations in their 'detected' epochs.

Each member of the spectroscopic sample of SLSNe from DES have many more detected epochs than this minimum requirement. These objects were detected in at least 3 filters (there were some occasional high redshift g band drop-outs), and these filters each have a minimum of 5 epochs. I therefore required objects to have at least 5 epochs detected (to 5σ or better) in each of at least 3 filters. This criterion returned 8,972 of 31,642 objects, or 28.4%.

4.1.3 Season requirement

Active galactic nuclei (AGN) constitute the largest fraction of astrophysical contaminants in the DES-SN transient catalogue. The lightcurves of these objects are produced by the accretion of matter onto supermassive black holes at the centres of distant galaxies. For a comprehensive review of AGN, see Padovani et al. (2017). Observationally, these objects are distinguished from SNe by their lightcurves[1], which exhibit stochastic flux variations over periods of years or more, usually with multiple peaks detected in all 5 seasons of the DES-SN survey, and very little colour evolution.

Figure 4.1 shows a comparison of a typical AGN lightcurve to a potential SLSN candidate. The flux in each epoch was computed by the DES difference imaging pipeline (Kessler et al., 2015), which was described in detail in Chapter 2. Template images were constructed from previous seasons, except for the first season, when the template was constructed from Y2 images.

[1]They can also be distinguished by the location in their host galaxies; SNe tend to explode away from the centre of their hosts. For this reason, the visual inspection of the difference imaging 'stamps' can be a useful discriminator.

Occasionally, the template image may contain a greater flux than the corresponding aligned pixels in the search image, resulting in a negative flux in the difference image. This was especially likely if the template image contained transient flux, which was often the case for AGN, and occasionally for long duration SNe in DES.

The lightcurves of the confirmed SLSNe showed that SLSN lightcurves from DES-SN span no more than 2 seasons (and usually only one). The tail end of lightcurves are occasionally still detectable in a given season for SLSNe that have exploded at the end of the preceding season. To remove a large number of AGN contaminants, objects which were detected in more than 2 consecutive seasons were discarded. This cut returned 3,438 of 8,972 objects, or 38.3%.

4.1.4 Host galaxy cut

SLSNe explode predominantly in faint, low mass dwarf galaxies, with masses a factor $\sim 10^{-3}$ less than that of the Milky Way (Neill et al., 2011; Lunnan et al., 2014; Leloudas et al., 2015; Schulze et al., 2018). Perley et al. (2016) measured an upper bound to the stellar masses of 32 host galaxies of SLSNe from PTF to be $\log(M_*/M_\odot) < 9$. Meanwhile, Chen et al. (2017) used a sample of 60 SLSN host galaxies from the literature to measure a median stellar mass of $\log(M_*/M_\odot) = 8.3$.

Angus et al. (2016) used HST observations in the IR and UV to find similar SLSN host mass constraints of $7 \leq \log(M_*/M_\odot) < 9$, with a median of $\log(M_*/M_\odot) \sim 8$. They also constrained the UV absolute magnitudes of SLSN host galaxies to $UV_{\rm AB} \geq -16.5$, compared to CCSN hosts, whose UV absolute magnitude they constrained to $UV_{\rm AB} \gtrsim -22$.

I expected that the host galaxy luminosities of objects remaining in the sample would be faint if the transient object was a true SLSN. Indeed, in the spectroscopic sample I found that 42% of the objects were 'hostless', compared to an assumed hostless rate of 5% for the SN Ia analysis of Gupta et al. (2016). These hostless SLSNe exploded in galaxies whose apparent

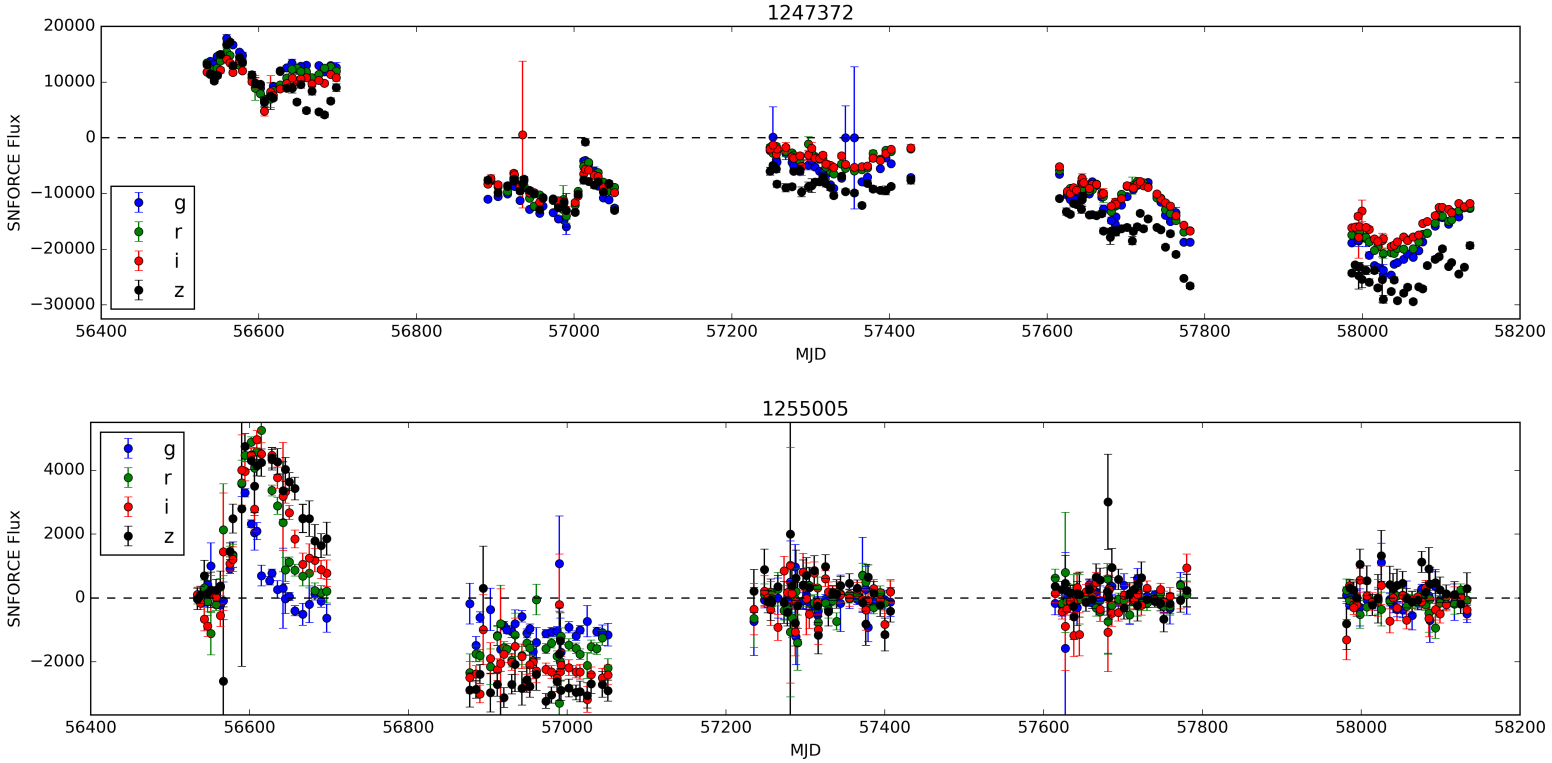

Figure 4.1: Comparison of a typical AGN lightcurve (*top*) to a potential SLSN candidate (*bottom*). All 5 seasons of DES-SN observations are shown. The AGN has continuously varying flux in all 5 seasons, while the SLSN candidate has a constant flux in seasons in which it was not detected. Negative fluxes are a result of difference imaging.

magnitudes were fainter than the single epoch SN field depths (according to Kessler et al. 2015, $m^{\rm lim}_{\rm shallow} \sim 23.5$, $m^{\rm lim}_{\rm deep} \sim 24.5$), and hence were not visible in the images. The host matching algorithm used in DES-SN is described in Chapter 2.

Of the non-hostless members of the spectroscopic SLSN sample, the faintest relative to its host galaxy showed a difference between the host apparent magnitude and the SN peak apparent magnitude $m_{\rm host} - m_{\rm SN} > 0.7$. I therefore required objects to either be hostless, or to be at least 0.7 mag brighter than their host if it was visible in the single epoch images. This criterion mitigated the effect of contamination from 'normal' SN types, and returned 571 of 3,438 objects, or 16.6%.

4.1.5 `pSNID` fit probabilities

The final step of the `DiffImg` pipeline is the photometric identification of SNe using the code `pSNID` (Sako et al., 2011). `pSNID` was described in more detail in Chapter 2. In brief, `pSNID` computes the χ^2 and the probability that the model describes the data (`fitprob`) for a grid of SN Ia, SN Ib/c and SN II templates across redshift. `fitprob` is not normalised across types, and candidates can have a low `fitprob` for all three of the ordinary SN types.

I used the `pSNID` `fitprob` to remove standard SN contaminants in the current sample. To do this, I required that lightcurves must have a `fitprob` value less than some critical value $p_{\rm crit}$, for each of the 3 SN types in `pSNID` (SN Ia, SN Ib/c, and SN II). $p_{\rm crit}$ was found by examining the `fitprob` values for each of the spectroscopically classified sample of SLSNe described in Chapter 3. $p_{\rm crit}$ was then given by the maximum `fitprob` of the spectroscopic sample. These values are $p^{\rm Ia}_{\rm crit} = 0.05$, $p^{\rm Ib/c}_{\rm crit} = 0.01$, and $p^{\rm II}_{\rm crit} = 0.12$. Candidates with `fitprob` values higher than these were discarded from the current sample as they were likely SNe Ia, SNe Ib/c, or SNe II.

The combination of these 3 selection criteria (one per SN type), returned 209 of 571 objects, or 37%.

Masked epochs

The photometric precision of the DES-SN difference imaging pipeline is limited at the 2% level (Kessler et al., 2019). If there was one (or more) discrepant epoch(s) in the fit (e.g. due to cosmic rays), `pSNID` may obtain a bad reduced χ^2 for a 'good' SN Ia due to the small photometric errors, and the SN Ia will in turn *not* be targeted for spectroscopic follow up. This problem was solved early in the DES-SN survey by allowing `pSNID` to reject outliers from the fit, and re-fit without them.

However, this solution has an inconvenient feature for the current analysis. An illustrative case in point is DES17C3aux (Figure 4.2). This good SLSN candidate did not pass the SN Ia `pSNID` cut described above. `pSNID` rejected epochs on the extended rise, forcing the remaining lightcurve epochs to be more consistent with a SN Ia than they would have been if all epochs were included. The masked lightcurve is obviously not representative of the underlying explosion, and this SLSN candidate should not have been rejected from the sample.

I mitigated this issue by investigating objects that had fewer epochs used in the `pSNID` fits (`NPT_x`, where the subscript `x` denotes the SN type) than the total number of detected epochs (`numobs_ml`, epochs that passed the `autoScan` machine learning test). I reran the original selection query from Section 4.1.1, but this time with the additional requirement that `NPT_x / numobs_ml < 1`. The resultant list of objects with masked lightcurves were passed through all of the selection criteria described above (except the `pSNID cut`), and an additional 20 objects were added to the sample.

4.2 Human selection criteria

By enforcing the automated cuts above I have reduced the original sample of 154, 748 to 229 objects. The lightcurves and difference image 'stamps' of these objects were visually inspected to identify promising SLSN candidates and eliminate any obvious contaminants that remained. This 'eyeballing' was

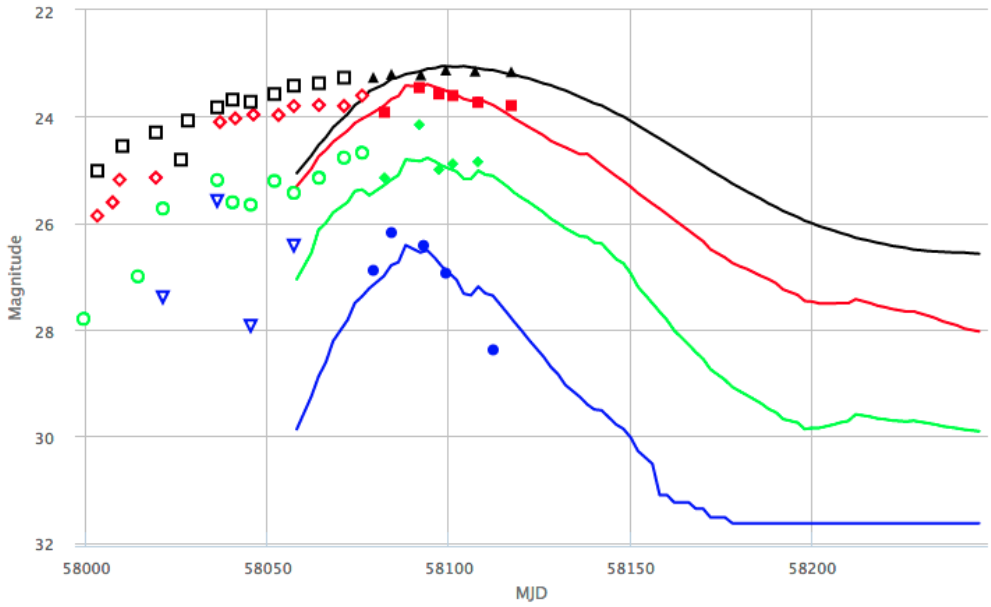

Figure 4.2: `pSNID` SN Ia fit to DES17C3aux, a good SLSN candidate from DES-SN. The empty points on the rise were masked by `pSNID`, and the remaining solid points were then more consistent with a SN Ia. This object would have been removed from the sample without the extra criterion defined in Section 4.1.5. This screenshot was taken directly from the DES-SN ATC webpage, which helped to coordinate the spectroscopic follow up of DES-SN.

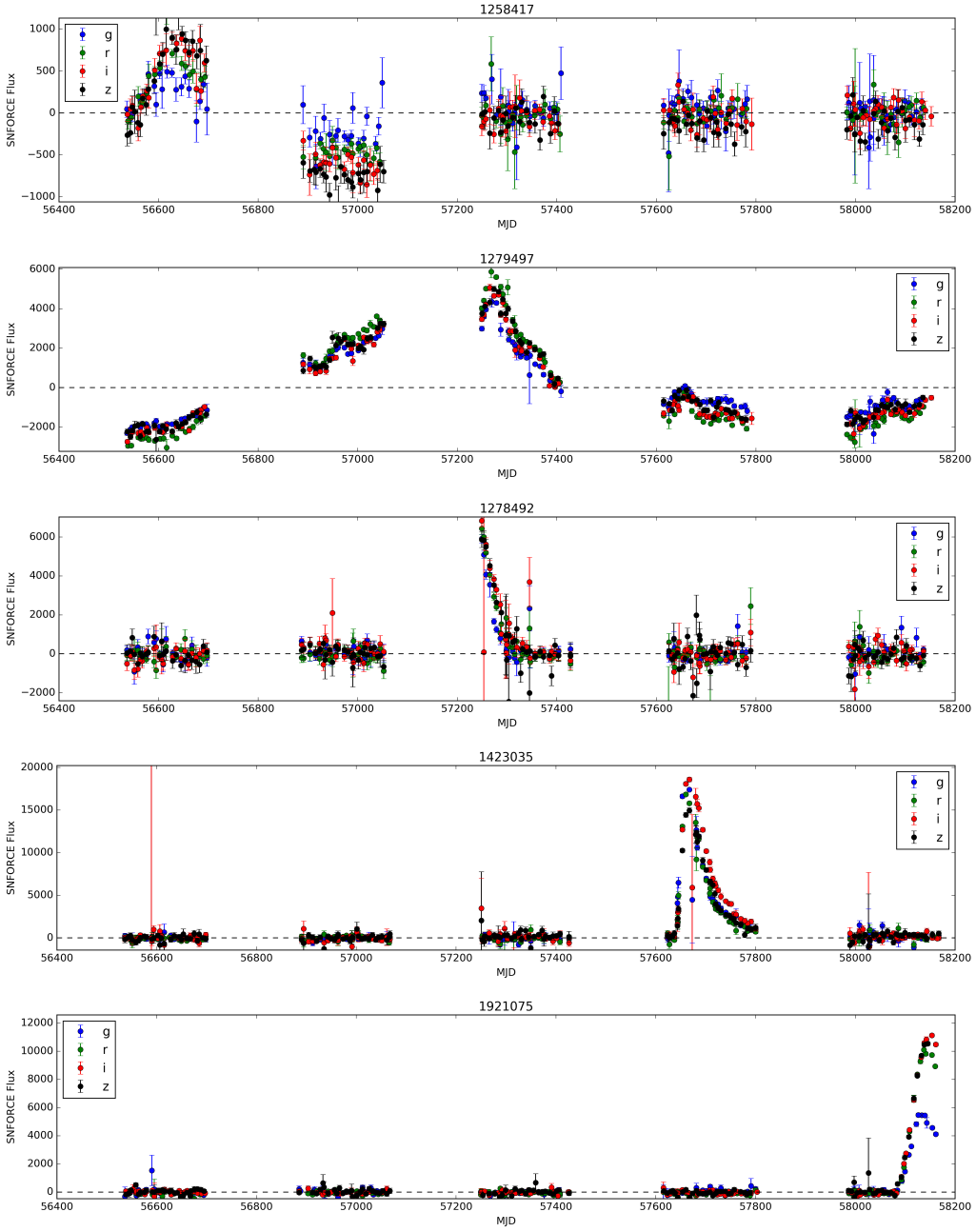

Figure 4.3: Selection of five year lightcurves for objects that passed my automated selection criteria in Section 4.1. From top to bottom, *1st:* A low signal-to-noise SLSN candidate, where the negative flux in Y2 is due to transient flux in the template image; *2nd:* a probable AGN that was detected in only 2 consecutive seasons; *3rd:* A likely SN suffering from temporal edge effects; *4th* A fast rising SN candidate and *5th:* a high quality SLSN candidate. The *2nd, 3rd* and *4th* objects did not pass the visual inspection of Section 4.2, while the *1st* and *5th* did.

	Initial selection	Cut 1	Cut 2	Cut 3	Cut 4
Unclassified	31067 (98.2)	8480 (94.5)	3025 (88.0)	430 (75.3)	175 (76.8)
SLSN	22 (0.07)	22 (0.25)	22 (0.64)	22 (3.85)	22 (9.21)
Type II SN	68 (0.21)	66 (0.74)	62 (1.80)	20 (3.50)	17 (7.46)
Type Ia SN	410 (1.30)	336 (3.74)	296 (8.61)	94 (16.5)	11 (4.82)
Type Ib/c SN	16 (0.05)	15 (0.17)	13 (0.38)	2 (0.35)	2 (0.88)
AGN	55 (0.17)	50 (0.56)	18 (0.52)	2 (0.35)	2 (0.88)
Other	3 (0.01)	2 (0.02)	1 (0.03)	0 (0.00)	0 (0.00)
Total	31642	8972	3438	571	229

Table 4.1: The number of each spectral type which passed my automated cuts. The percentage of the total sample after the corresponding cut was made is shown in brackets. In the top row the labels refer to: *Initial selection:* My initial selection of objects (Section 4.1.1) *Cut 1:* Lightcurve quality cut (Section 4.1.2) *Cut 2:* Season requirement (Section 4.1.3) *Cut 3:* Host galaxy brightness cut (Section 4.1.4) and *Cut 4:* `pSNID` fit probability cut (Section 4.1.5)

carried out as a collaboration between 2 members of the ICG (C. Frohmaier and myself) and 3 members of the Southampton Supernova Group (C. Angus, M. Smith, and C. Inserra). We wished to carry out this final stage of sample selection in an unbiased way, and to mitigate the subjectivity of human opinion. To achieve this, we designed 4 quantitative criteria to guide each of the examiners. These were used to either pass or fail objects based on their lightcurves.

4.2.1 Peak requirement

Rest frame SLSN lightcurves typically have a duration on the order of months. DES-SN observed 10 fields over a $\sim$5.5 month period. The observer frame lightcurves are therefore vulnerable to temporal edge effects, particularly at high redshift where they become stretched by cosmological time dilation.

For lightcurves missing the epochs of maximum light (where they reach peak brightness outside of a season), it was impossible to constrain the peak brightness and peak time, and model fits became unfeasible. Beyond this, these objects were outside of the effective volume-time of the rate computation (Chapter 5). For these reasons objects with a missing peak were excluded from the spectroscopic sample when simulating for the efficiency as a function of redshift and explosion date (Chapter 3).

To maintain consistency between the photometric and spectroscopic samples, and also to ensure that objects were within the effective volume-time, I required that the epoch(s) of maximum light must have been within the corresponding observing season. To achieve this I enforced that the observed lightcurve must have had at least 1 epoch either side of maximum light, in at least 2 filters. I required at least 2 filters as single epochs can appear as maxima due to purely statistical fluctuations.

4.2.2 Non-detections

As stated above, the difference imaging pipeline can give negative flux values if transient flux exists in the template image. Meanwhile, detected epochs in my automated criteria were defined as those with a positive flux detection of at least 5σ. The previous requirement to be 'detected' in at most 2 seasons would not have removed objects whose lightcurves vary below zero in their third or subsequent seasons. As AGN lightcurves were often constituted by epochs with negative flux, some of these may have remained within the sample.

Supernovae in the DES data were observed in at most 2 DES seasons. In years in which the SN was not detected, they showed a constant flux, usually consistent with zero within the photometry noise. I required lightcurves to be of constant flux in seasons in which they were not detected within the measured photometry noise.

4.2.3 Rise and decline time

Type IIP SNe have a rise time of < 5 rest frame days, with a plateau of $\sim$ 100 rest frame days after peak (Hicken et al., 2017). Type IIL, Type IIn, and Type IIb SNe each have a similar rise time of < 20 rest frame days (Arcavi, 2017), although their declines vary significantly. Type Ia SNe, on the other hand, typically have a rise time of 18.98 ± 0.54 (rest frame) days (Firth et al., 2015), with a slower decline.

Meanwhile SLSNe have a rise time of $\sim$25 days in the rest frame. In order to mitigate contamination from other SN types in the final sample, I required objects to have an observer frame rise time of > 25 days, and an observer frame decline time of > 25 days. A caveat to this cut was the following. If the entire rise time was not available in the data (i.e. if the very early lightcurve was cut by the temporal edge of the observing season), I did not enforce the rise time criterion. Similarly, if the entire decline was not available, I did not enforce the decline criterion.

SLSNe tend to rise faster in the blue bands than they do in the red bands, as the initially hot photosphere adiabatically cools as the SN expands. I therefore required that objects must fulfill this criterion in at least 2 bands (usually at least r and z).

Furthermore, the beginning and end of the rise (or decline) are ill defined due to the $\sim$7 day cadence of the DES-SN survey. This introduced an uncertainty (7 days) in the exact explosion date (and peak date) due to a finite sampling time.

This is the final selection criteria I enforced upon the objects. Overall I have reduced the original 154,748 objects to 52 objects, including spectroscopically classified SLSNe, unclassified SLSN candidates, and spectroscopically classified contaminants.

4.3 Final sample from photometric selection

The 52 objects that remained after enforcing all cuts are listed in Table 4.2. 14 of the 22 spectroscopically classified SLSNe were recovered. 7 spectroscopic SLSNe of the original 22 were removed from the sample as their peaks were not observed. The definition of the effective volume-time in the previous chapter was partially based on observation of the peak. These objects were therefore outside of the effective volume-time in the rate computation. DES16C3cv, however, was removed due to its anomalous double peaked lightcurve. Lightcurves of these spectroscopically classified objects can be seen in Figure 3.5.

8 of the 52 objects had spectroscopic classifications of non-SLSN, and were contaminants. Of these 7 objects, 1 was a confirmed SN Ia, 4 were SNe II, and 2 were possible stripped envelope events (SNe Ib/c). Lightcurves of these contaminants can be seen in Figure 4.11.

30 of the 52 objects were not spectroscopically classified. Lightcurves of these unclassified SLSN candidates can be seen in Figure 4.10. A total of 43 spectra were obtained for 16 of these unclassified candidates by the

AAT, Gemini, Magellan, GTC, Keck, and VLT. The majority of these lacked sufficient signal in the spectra for a secure classification to be made. However, 18 of these 43 spectra had yet to be reduced. My photometric pipeline highlighted these objects to researchers at Southampton, and these 18 spectra were subsequently reanalysed. Of these, 2 spectroscopic classifications were made, and these objects are detailed in the following section.

4.4 Resultant spectroscopic classifications

4.4.1 DES17X1blv

DES17X1blv was an excellent SLSN candidate, and DES-SN provided good lightcurve coverage. At the time of running my photometric pipeline this object had not been classified. It rose for ~ 4 observer frame weeks, peaked at an apparent magnitude of $m_r = 22.6$ within the first half of Y5, and subsequently declined for the following $\sim$8 weeks of the season. After rising for $\sim$30 (observer frame) days, DES17X1blv was spectroscopically observed by Magellan on 10th November 2017. This was followed by observations with VLT on 11th November, and AAT on 19th November. The VLT spectrum was reduced by M. Smith and C. Angus in Autumn 2018 and a spectroscopic classification of a SLSN-I at $z = 0.69$ was made. The lightcurve is presented in Figure 4.4, and the spectrum in Figure 4.5. At this redshift any Hα emission present in the spectrum would have been redshifted out of the observed wavelength range, and the absence of hydrogen in the spectrum is not entirely secure (this is the case for many of the spectroscopically confirmed SLSNe-I in the DES sample). This object was nonetheless added to the sample of confirmed SLSNe-I from DES, and is presented in Angus et al. (2019).

4.4.2 DES16C3eco

DES16C3eco was an unusual object which passed the above criteria. This object has a relatively fast rise (11, 15, 25 and 35 observer frame days in

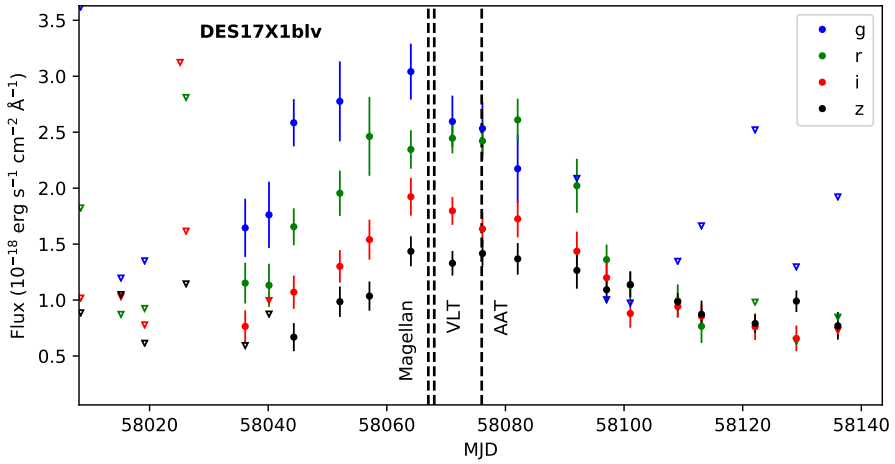

Figure 4.4: The lightcurve of DES17X1blv. This object was a promising SLSN-I candidate highlighted by the photometric search pipeline described in this chapter. Vertical dashed lines indicate the lightcurve phase of spectroscopic observations. The VLT spectrum was reduced by M.Smith and C.Angus, and this object was classified as a SLSN-I at $z = 0.69$.

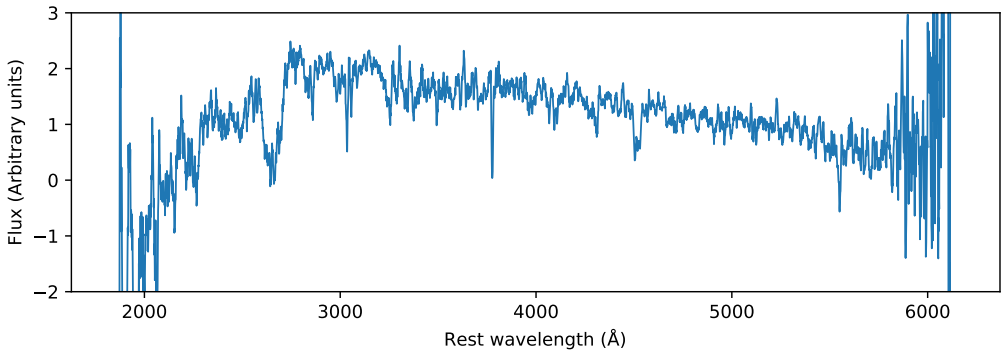

Figure 4.5: The 1D reduced VLT spectrum of DES17X1blv. A blue continuum can be seen, with a broad absorption feature at 2650Å from Mg II and C II. The faint absorption 'comb' from OII can also be seen between $4000 - 4500$Å, which defines the SLSN-I spectroscopic class.

the *griz* bands), a peak in Y4 around 31st December 2017, and a very long plateau in the tail. This object was still detectable more than 12 observer frame months after peak at which point DES-SN concluded its observations.

The first spectroscopic observation of DES16C3eco was carried out by Keck on the 2nd January 2017, while the object was at peak. Follow up observations (see Figure 4.6) occurred in the subsequent DES-SN season, by AAT on 20th November 2017, Keck on 14th December 2017, and Gemini on 14th January 2018.

Interest in this object was revitalised due to the photometric pipeline described here. C. Curtin (University of Melbourne) reduced the Keck spectrum, but observational artifacts distorted this spectrum in the red to such a degree that classification was not possible. However, M. Smith at Southampton reduced the Gemini spectrum, which revealed a strong emission feature at $\lambda = 7320$Å. The Gemini spectrum of DES16C3eco can be seen in Figure 4.7. If this feature is due to Hα emission, this would lead to a tentative spectroscopic classification of a Type II SN at $z = 0.12$. However, the tail of this SN is exceptionally long for any SN type. Meanwhile, there are a small number of AGN in the DES sample which also show flat lightcurve evolution on the order of months, and another possibility is that this object may belong to this class of AGN. A consensus has not yet been reached on the underlying astrophysics of this unusual object.

4.5 Conclusion

In this section I have described the criteria that I used to select objects from DESDM to construct the photometric sample for my rate computation of Chapter 5. These criteria were divided into those that were automated and those that were carried out by visual inspection of the lightcurves and difference images (stamps).

The automated criteria included selections based on the number of epochs detected, the number of seasons in which an object was detected, the bright-

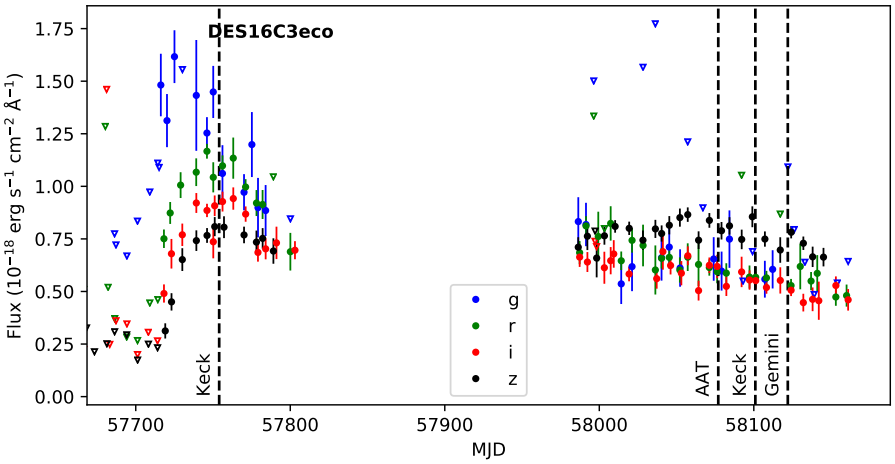

Figure 4.6: The lightcurve of DES16C3eco, an extremely long duration transient highlighted by the photometric search pipeline. The figure shows photometry from Y4 and Y5. This object was first detected in Y4, and still detected at the end of Y5, when DES-SN concluded observations. The vertical dashed lines indicate the lightcurve phase of spectroscopic observations. From a single emission feature in the Gemini spectrum this object may be a Type II SN at $z = 0.12$.

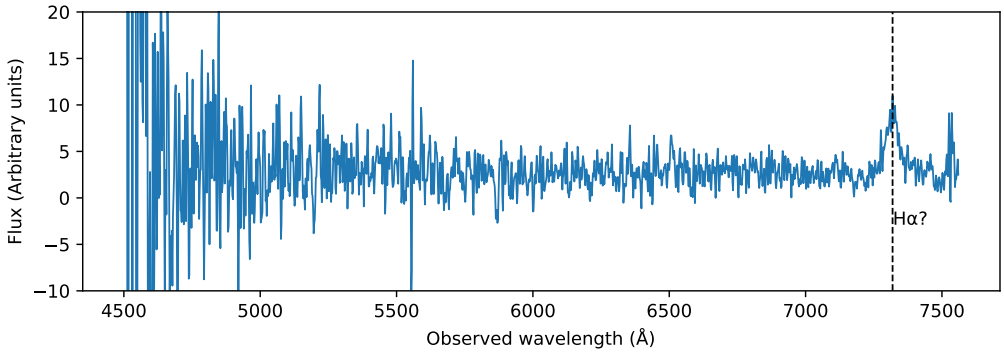

Figure 4.7: The spectrum of DES16C3eco. While the signal to noise ratio is low, there is a clear feature at 7320Å. If, as is suspected, this feature is due to Hα emission, then this object may be a Type II SN at $z = 0.12$.

ness of the object relative to its host galaxy, and the probability of fit of 'ordinary' SN templates (with `pSNID`) to the observed photometry.

The human selection critera included selections based upon the temporal location of maximum light, a flat lightcurve in non-detection years, and the extended rise and decline of the lightcurve.

Enforcing these selection criteria on the raw sample of DES transients gave a sample of 52 objects. After removing 8 contaminants, I was left with 14 spectroscopically classified SLSNe-I and 30 photometric SLSN candidates, which were passed to the analysis of Chapter 5. The distribution of these objects over discovery field can be seen in Figure 4.8 and over discovery year in Figure 4.9.

A critical quantity required to compute the volumetric rate is the number of transients that have good quality survey photometry but that lack a spectroscopic classification. Traditionally, a spectroscopic efficiency parameter is used to account for these 'missing objects'. However, this parameter is difficult to constrain as a function of redshift, as the redshifts of the objects that contribute to it are often unknown. Therefore, I have chosen a different method. In this chapter I have undertaken a deep search into the DES photometry for SLSN candidates that were not spectroscopically classified. I assume that this search has retrieved *every* SLSN that exists within the DES photometry and that lies within the effective volume-time of my rate calculation. I therefore set the spectroscopic efficiency in the rate equation $\epsilon_{\rm spec} = 1$ (Chapter 5), as objects without a spectrum are nonetheless included in my rate computation.

However, the criteria described in this chapter are based on the observed tendencies of the known SLSN population, but it is possible that a small number of SLSNe may have been excluded from the sample. For example SLSNe have a strong preference to explode in star forming dwarf galaxies, as described above. However, the recently discovered SN2017egm exploded near the center of a massive spiral galaxy (Nicholl et al., 2017a) and hints that on rare occasions SLSNe may explode in bright hosts. If such rare SLSNe exist

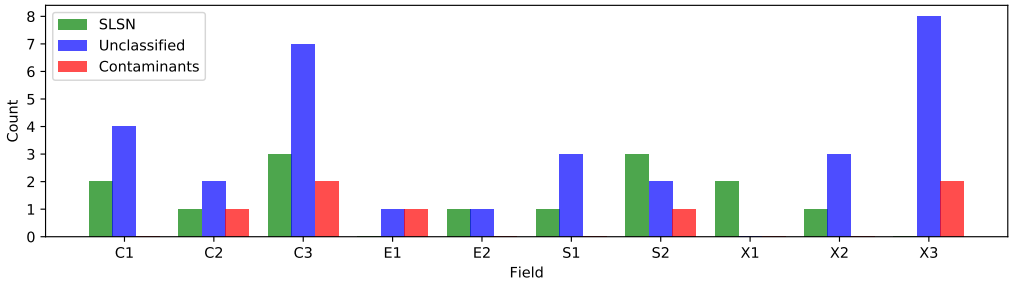

Figure 4.8: The number of transients which passed the photometric selection criteria as a function of the DES observing field in which they were discovered. Fewer of the relatively faint objects discovered in the deep fields (C3, X3) were spectroscopically classified.

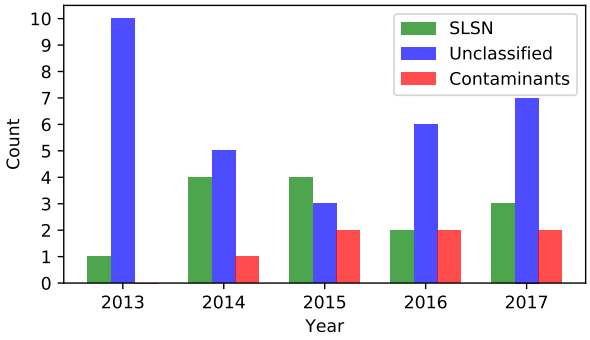

Figure 4.9: The number of transients which passed the selection criteria as a function of the DES year of their discovery. The DES-SN spectroscopic follow-up strategy matured after Y1, resulting in more classifications.

within the DES-SN sample, they would have been excluded by the selection criteria described here.

In the next chapter I will use this sample of SLSNe with the photometric efficiency simulations of Chapter 3 to carry out the final steps necessary to compute the volumetric rate of SLSNe-I from DES.

Name	RA	Dec	Peak i	Redshift	Redshift source	Spectral class
DES13C2ehl	55.07	-29.45	-	0.528±0.0829	gal photo	-
DES13C3hzn	53.13	-28.58	-	0.738±0.0789	gal photo	-
DES13E1nkg	8.13	-42.43	-	-	-	-
DES13S1ne	42.51	0.91	-	-	-	-
DES13S2cmm	40.64	-1.36	-20.34	0.662	sn spec	SLSN-I
DES13S2uhm	41.17	-1.02	-	-	-	-
DES13X2jup	34.94	-6.65	-	-	-	-
DES13X3aajk	37.14	-4.91	-	0.295	gal spec	-
DES13X3aall	36.84	-4.04	-	-	-	-
DES13X3obu	36.25	-4.53	-	-	-	-
DES13X3oy	35.90	-3.98	-	-	-	-
DES14C1fi	53.46	-27.06	-21.62	1.30	sn spec	SLSN-I
DES14C1fs	54.88	-27.03	-	0.744±0.050	gal photo	-
DES14C1gf	53.88	-27.46	-	-	-	-
DES14C1rhg	54.43	-27.71	-19.35	0.470	sn spec	SLSN-I
DES14C3rhw	51.82	-28.73	-	0.341	sn spec	SN II
DES14S1dch	43.47	-0.59	-	-	-	-
DES14S2sz	41.84	-1.19	-	-	-	-
DES14S2qri	40.88	-1.13	-21.85	1.49	sn spec	SLSN-I
DES14X2byo	35.95	-6.14	-21.60	0.869	sn spec	SLSN-I
DES14X3afm	36.62	-4.08	-	0.627±0.0824	gal photo	-
DES15C3de	52.52	-28.82	-	0.490±0.0830	gal photo	-
DES15C3fx	52.21	-28.25	-	0.200	sn spec	SN Ia
DES15C3hav	52.97	-28.25	-19.48	0.392	sn spec	SLSN-I
DES15E2mlf	10.39	-43.45	-22.01	1.86	sn spec	SLSN-I

Name	RA	Dec	Peak i	Redshift	Redshift source	Spectral class
DES15S1nog	43.06	-0.74	-19.92	0.566	sn spec	SLSN-I?
DES15S2nr	40.19	-0.89	-20.45	0.220	sn spec	SLSN-I
DES15X2asl	35.62	-6.96	-	0.327	gal spec	-
DES15X2mez	35.87	-6.51	-	-	-	-
DES15X3nad	35.98	-4.17	-	0.100	sn spec	SN II
DES16C1drb	53.56	-26.91	-	-	-	-
DES16C1mm	54.99	-27.38	-	0.366	gal spec	-
DES16C2aix	55.17	-29.38	-21.44	1.07	sn spec	SLSN-I
DES16C3dmp	52.87	-28.54	-20.43	0.565	sn spec	SLSN-I
DES16C3eco	52.81	-27.70	-	0.621±0.0824	gal photo	-
DES16E1mz	8.57	-43.65	-	0.229	sn spec	SN I
DES16S1ene	41.76	0.07	-	-	-	-
DES16X3bdj	35.73	-5.21	-	0.200	sn spec	SN Ib/c?
DES16X3cer	36.81	-4.31	-	-	-	-
DES16X3dlk	36.96	-5.19	-	-	-	-
DES17C2hnn	54.12	-28.71	-	-	-	-
DES17C2pf	53.54	-28.78	-	0.136	sn spec	SN II
DES17C3aux	52.91	-27.79	-	0.986±0.0789	gal photo	-
DES17C3dpb	52.90	-28.98	-	0.898±0.0805	gal photo	-
DES17C3efr	52.90	-27.18	-	-	-	-
DES17C3frx	51.51	-28.00	-	0.548±0.0509	gal photo	-
DES17C3gyp	51.97	-28.40	-21.57	0.47	sn spec	SLSN-I?
DES17E2ay	10.59	-44.24	-	0.186	gal spec	-
DES17S2oo	41.31	-1.26	-	0.225	sn spec	SN II
DES17X1amf	34.44	-5.60	-21.76	0.918	sn spec	SLSN-I
DES17X1blv	35.25	-4.48	-20.37	0.69	sn spec	SLSN-I
DES17X3cuq	37.33	4.67	-	-	-	-

Table 4.2: The final 52 objects from the search for photometric SLSN candidates. The absolute peak i band magnitude is derived from absorbed black body model fits to the spectroscopically classified SLSNe.

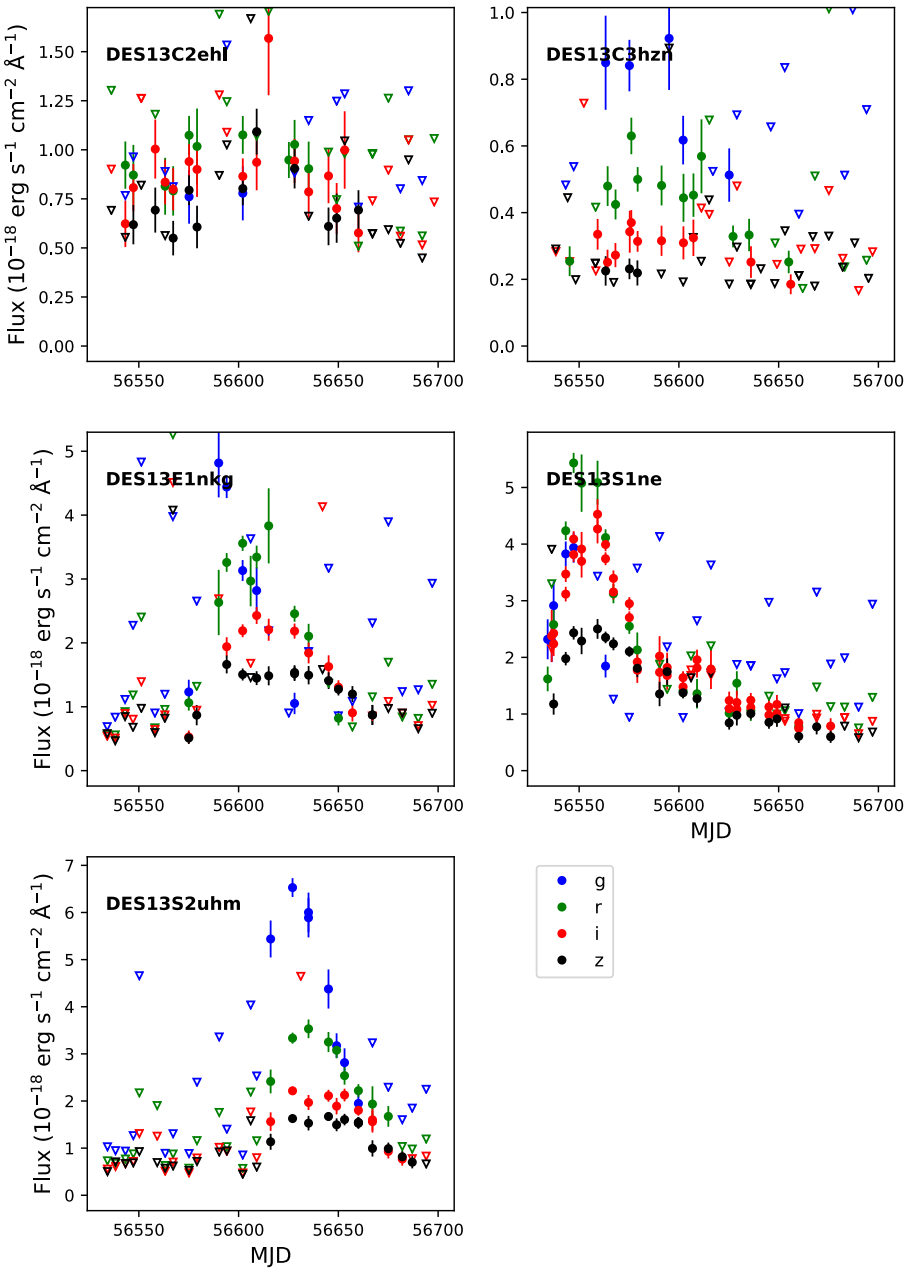

Figure 4.10: Single season lightcurves of the 30 photometric SLSN candidates that passed the photometric search pipeline.

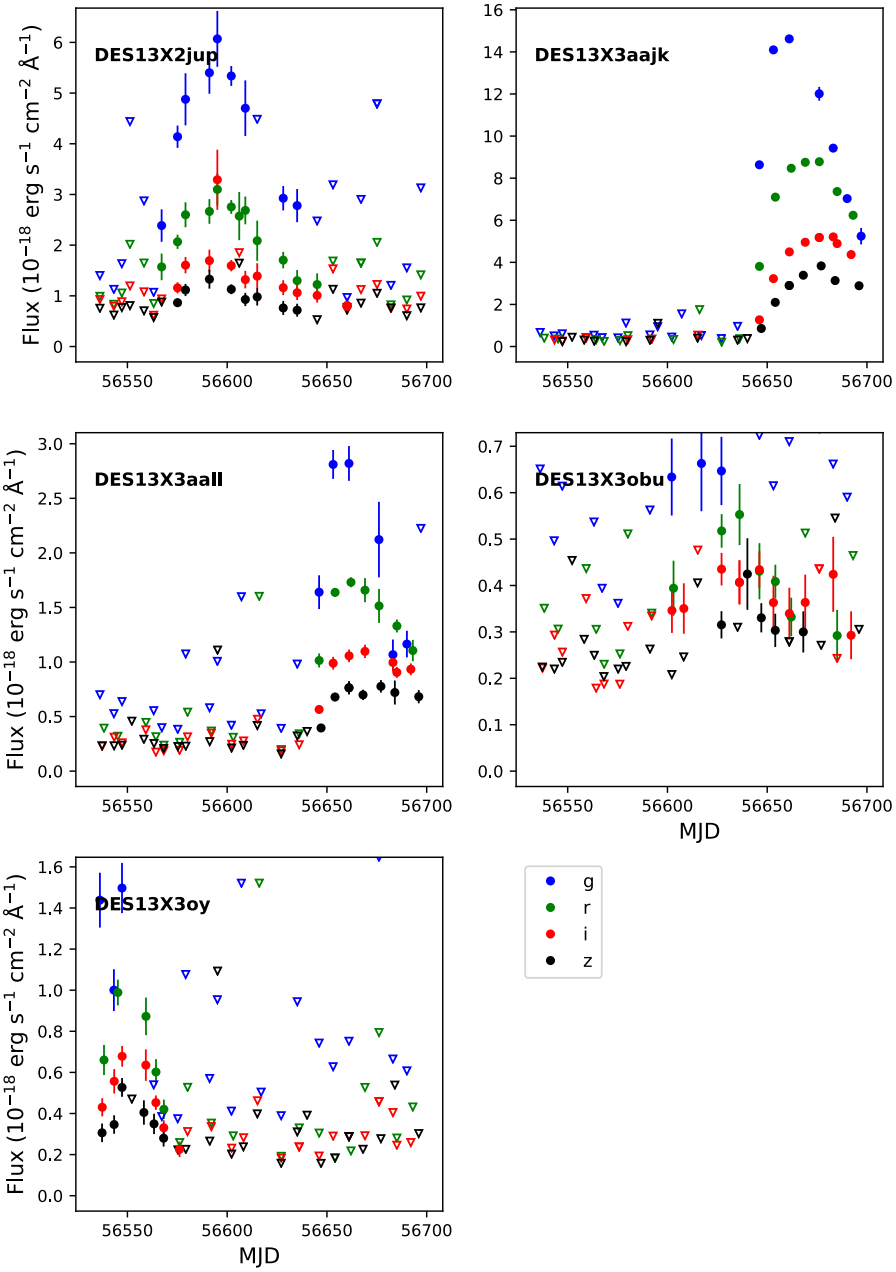
DES13X2jup
DES13X3aajk
DES13X3aall
DES13X3obu
DES13X3oy
Flux (10^{-18} erg s^{-1} cm^{-2} Å^{-1})
MJD
g
r
i
z

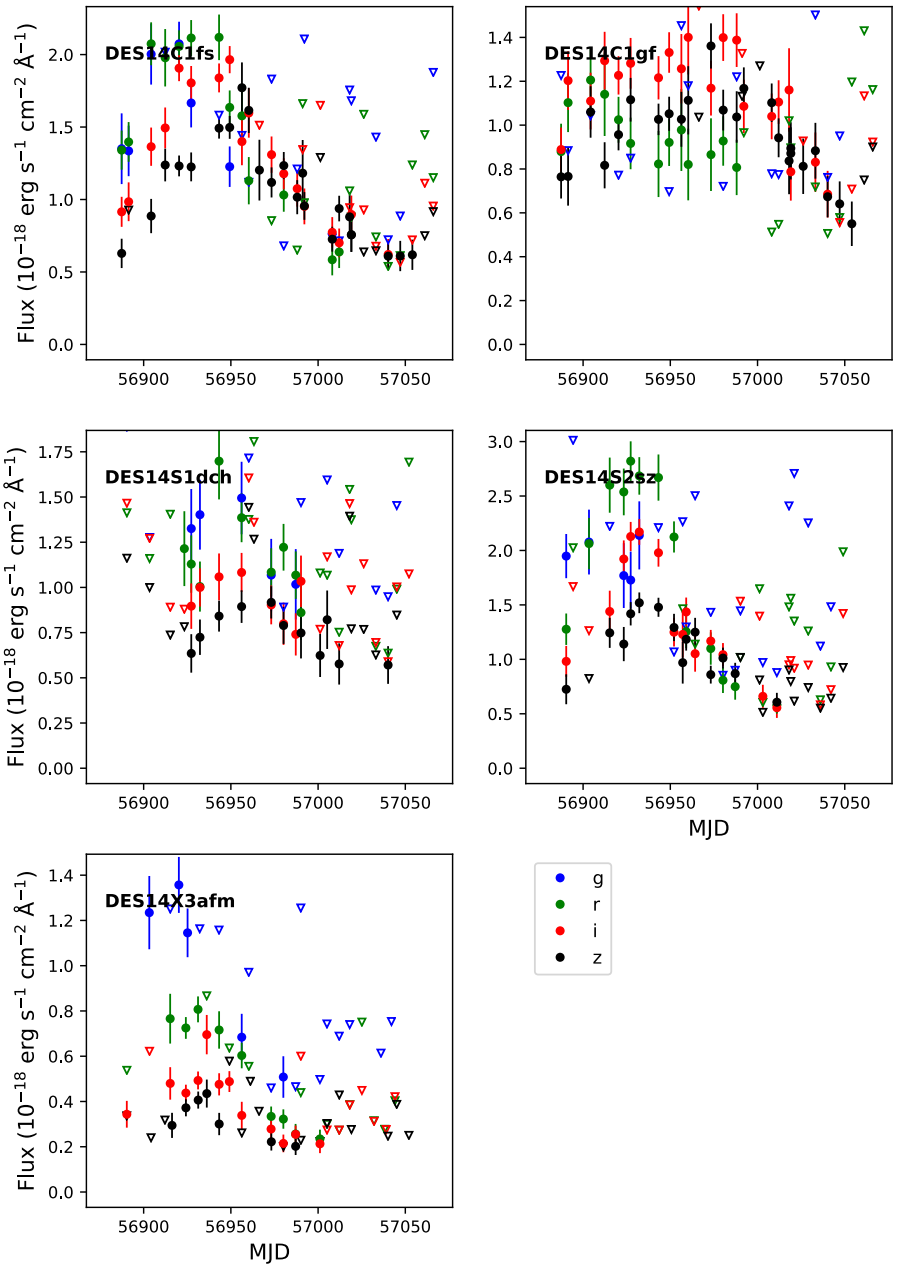
DES14C1fs
DES14C1gf
DES14S1dch
DES14S2sz
DES14X3afm
Flux (10^{-18} erg s^{-1} cm^{-2} Å^{-1})
MJD
g
r
i
z

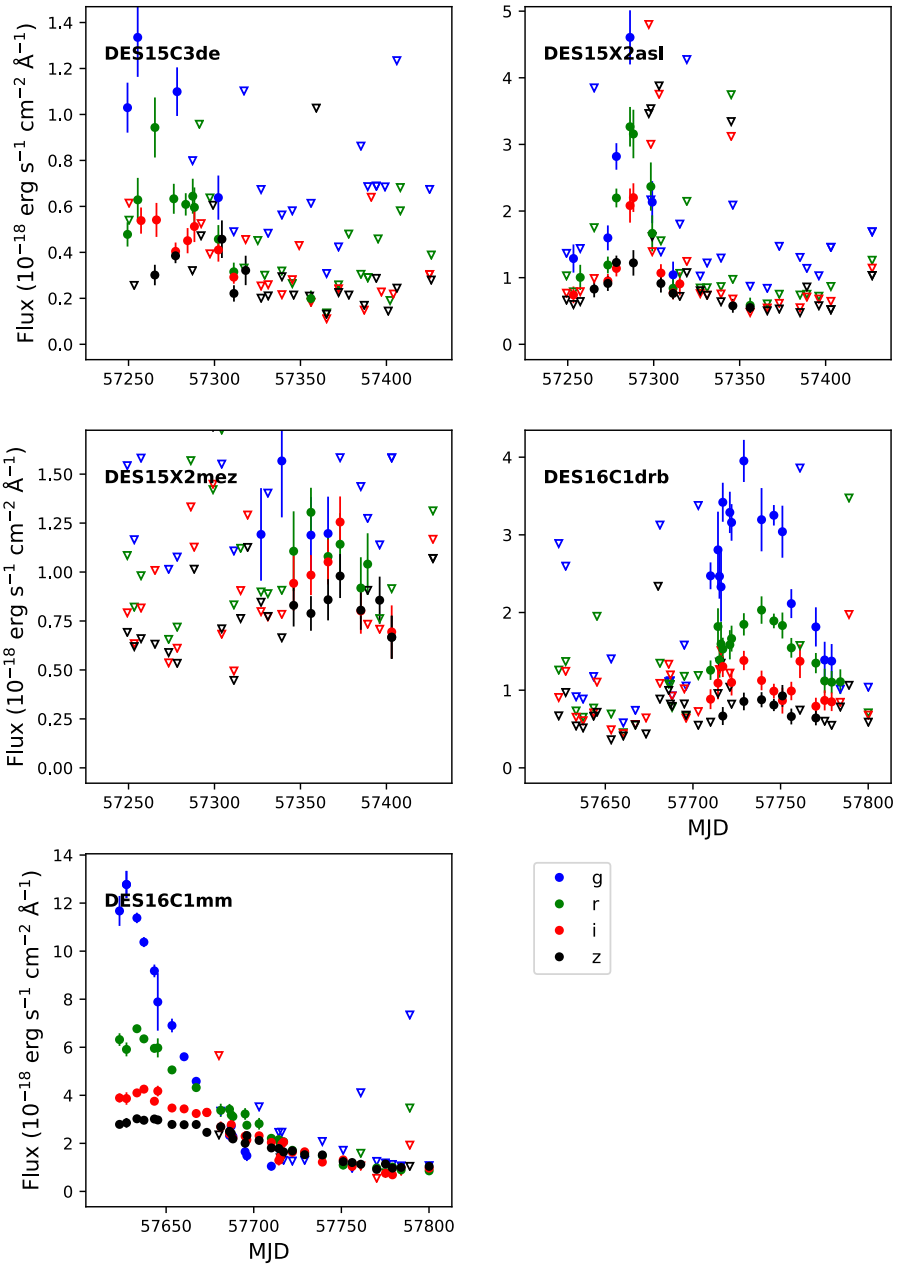
DES15C3de
DES15X2asl
DES15X2mez
DES16C1drb
DES16C1mm
Flux (10^{-18} erg s^{-1} cm^{-2} Å^{-1})
MJD
g
r
i
z

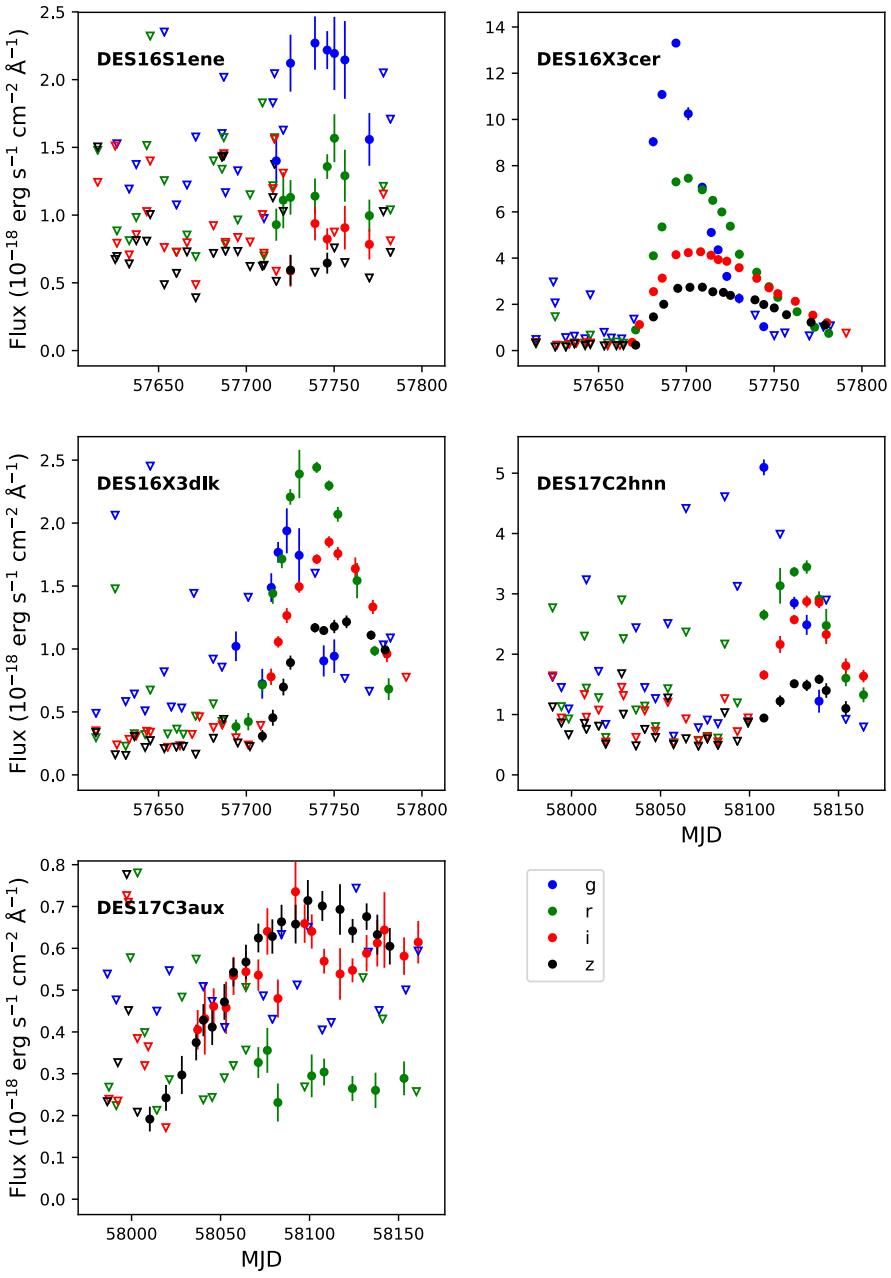
DES16S1ene
DES16X3cer
DES16X3dlk
DES17C2hnn
DES17C3aux
Flux (10^{-18} erg s^{-1} cm^{-2} Å^{-1})
MJD
g
r
i
z

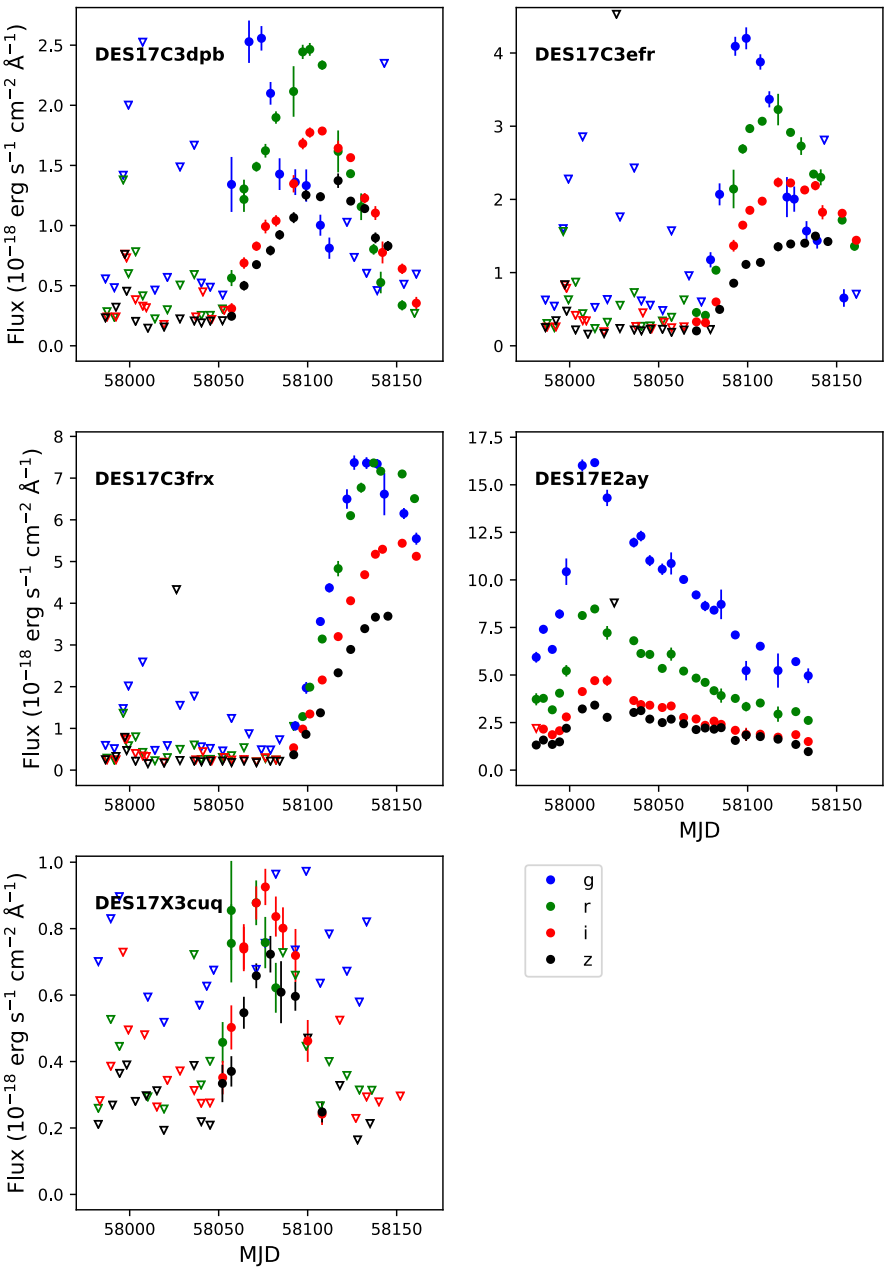
DES17C3dpb
DES17C3efr
DES17C3frx
DES17E2ay
DES17X3cuq
Flux (10^{-18} erg s^{-1} cm^{-2} Å^{-1})
MJD
g
r
i
z

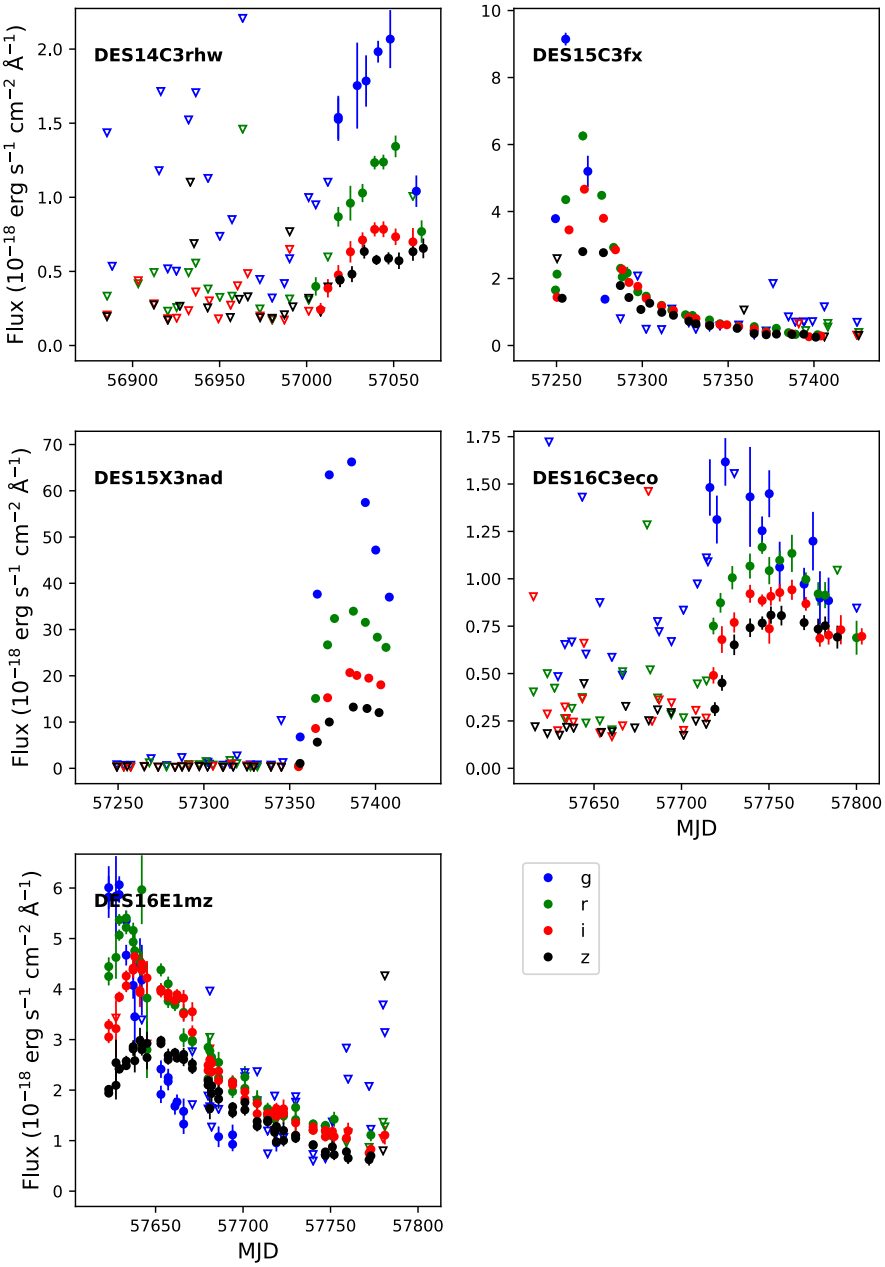

Figure 4.11: Single season lightcurves of the 7 spectroscopically classified contaminants that passed the photometric search pipeline.

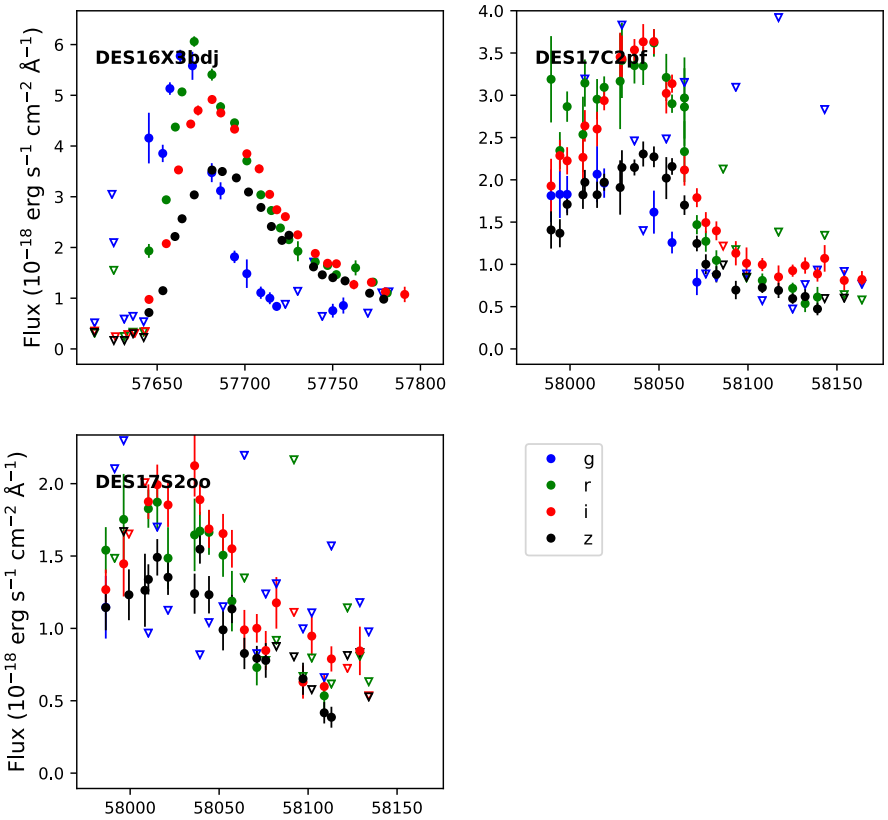
DES16X3bdj
DES17C2pf
DES17S2oo
Flux (10^{-18} erg s^{-1} cm^{-2} Å^{-1})
g
r
i
z

Chapter 5

The Volumetric Rate of Superluminous Supernovae

The work detailed in this chapter is entirely my own. References to other works, where necessary, are given throughout.

In this chapter I bring together the results of Chapters 3 and 4 to calculate the volumetric rate of SLSNe. I begin by introducing the volumetric rate equation for SNe. I compute the effective volume-time of the survey using the efficiency simulations of Chapter 3, along with the field of view of DECam. I present the final sample of SLSNe including the photometric SLSNe from Chapter 4. I account for SLSN candidates without redshift information using a Monte Carlo simulation method, which results in the distribution of possible SLSN volumetric rates. I fit a lognormal probability distribution function (PDF) to the Monte Carlo distribution and thereby determine the final result and its systematic uncertainty. I compare this result with literature measurements, and conclude by discussing the implications.

5.1 The Rate Equation

As discussed in Chapter 1, the volumetric rate ($R_{\rm V}$) of a sample of N SNe in a redshift bin $z_1 < z < z_2$ is calculated (e.g. Perrett et al. 2012) by summing over the inverse of the detection efficiencies ($\epsilon_{\rm i}$), and dividing by the comoving volume (V) contained within that redshift range,

$$R_{\rm V} = \frac{1}{V\,\Delta T}\sum_{i=1}^{N}\frac{(1+z_{\rm i})}{\epsilon_{\rm i}}. \tag{5.1}$$

The factor $(1+z_{\rm i})\,/\,\Delta T$ represents the effective observing time (ΔT) of the survey in the rest frame of the ith supernova. Taken together, the factor $V\Delta T$ is called the *effective volume-time* of the survey. The comoving volume V is given by,

$$V = \frac{\Phi}{41253}\frac{4\pi}{3}\Big[\frac{c}{H_0}\int_{z_1}^{z_2}\frac{dz'}{\sqrt{\Omega_{\rm M}(1+z')^3+\Omega_\Lambda}}\Big]^3, \tag{5.2}$$

where Φ is the search area of the survey in deg^2, z_1 and z_2 are the lower and upper limits of the redshift range of interest, c is the speed of light, and H_0, $\Omega_{\rm M}$, and Ω_Λ are the cosmological parameters. Throughout this thesis I have assumed a flat ΛCDM universe with $H_0 = 67.8$ km s^{-1} Mpc^{-1}, $\Omega_{\rm M} = 0.307$, and $\Omega_\Lambda = 0.693$ (Planck Collaboration et al., 2016).

5.1.1 Determination of the effective volume-time

In Chapter 3, I described the simulations used to determine the regions in redshift-explosion date space over which the survey is photometrically complete for all spectroscopic SLSNe whose peak was observed by DES and whose peak absolute magnitudes were brighter than $M_{\rm i} < -19.8$. These simulations resulted in 5 regions for each of the 10 DES fields in which the survey is photometrically complete. To find the effective volume-time of the survey, I transformed the redshift axis of these regions using Equation 5.2, such that the regions were now in volume-explosion date space. To carry out this computation, I first defined the area on the sky of each field, ϕ.

Survey area

I calculated ϕ by considering the CCD layout of DECam. DECam has 62 total science CCDs. Each of the 10 DES-SN fields is a single footprint of DECam, visited many times during the survey. I calculated the angular area of the footprint by considering the angular size of a DECam pixel, (0.263 arcsec, Flaugher et al. 2015), the number of pixels on a DECam CCD (4096×2048, Flaugher et al. 2015), and multiplying by the total number of active CCDs (60 after accounting for 2 non-active CCDs). The angular area of a SN field is then,

$$\phi = 4096 \times 2048 \times \left(\frac{0.263}{3600}\right)^2 \times 60 = 2.69\,\mathrm{deg}^2. \tag{5.3}$$

This method circumvents the need to account for gaps between CCDs. The positions of the CCDs on the sky in the case of the X fields is shown in Figure 5.1. Adjacent fields had an overlap of order 1% (D'Andrea et al., 2018). Repeat observations were also dithered by an angle on the order of a few arcseconds to mitigate the presence of artefacts in the difference imaging pipeline. Finally, pixels at the edge of the CCDs collected more light than those in the center, and an edge of a width of 8 pixels was not used for DES imaging (Estrada et al., 2010). Around 1% of the area of the CCDs was discarded due to edge effects. I considered the overlap, dithering and edge effects to be negligible in the rate calculation.

The redshift axis of the photometrically complete regions was transformed to comoving volume using Equation 5.2. The effective volume-time in each field-year combination was then simply the area of that region in the volume-explosion date space. The total effective volume-time of the survey, $V\Delta T$, was the sum of the areas of these 5 years $\times$ 10 fields = 50 regions. The region of effective volume-time from Y5 of observations of the C3 field can be seen in Figure 5.3. Summing the 50 photometrically complete regions gave a total effective volume-time of the survey $V\Delta T = (12.96 \pm 1.17) \times 10^7\,\mathrm{Mpc}^3\,\mathrm{yr}$, where the error comes from the estimation of a 9% systematic from the binning resolution given in Chapter 3.

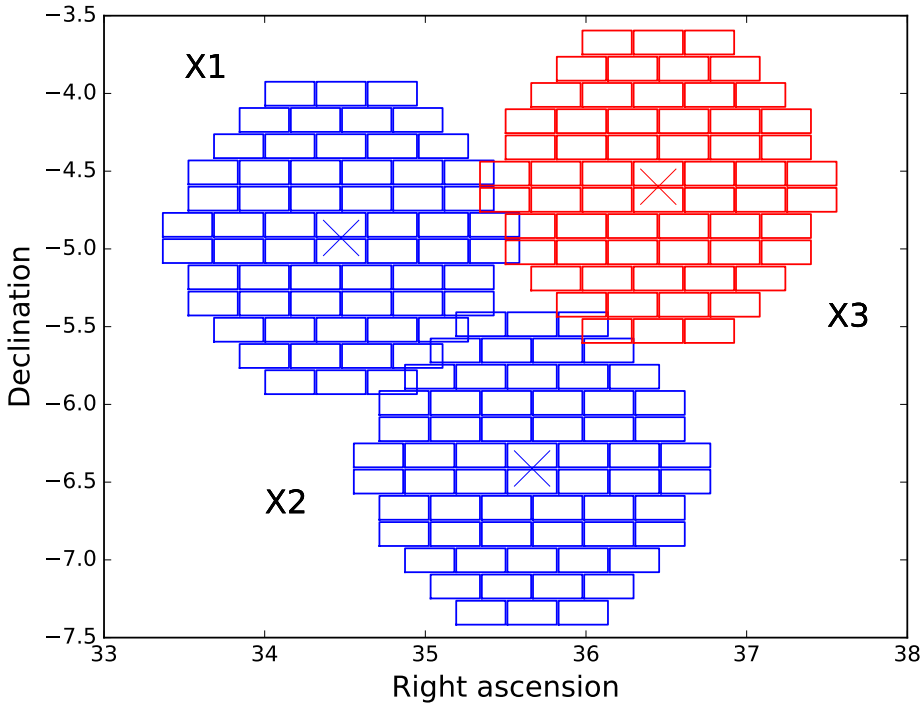

Figure 5.1: The position on the sky of individual CCDs in the X fields. Shallow fields are plotted in blue, and the deep field in red. I summed the angular area on the sky of each CCD in the footprint of a single field to compute the total area of that field. This area was used in the computation of the comoving volume for the rate. The overlap between adjacent fields was small (order 1%; D'Andrea et al. 2018), and I neglected it in the rate computation.

5.1.2 Detection efficiency

The computation of Equation 5.1 required knowledge of the detection efficiency ϵ of the survey. As described in Chapter 1, this efficiency is the product of two parts, and can be written,

$$\epsilon = \epsilon_{\rm phot} \times \epsilon_{\rm spec}. \tag{5.4}$$

I have carried out detailed simulations to evaluate the photometric efficiency as a function of both redshift and explosion date, as described in Chapter 3. For the rate computation in this chapter, I selected an effective volume-time in which the DES-SN search for SLSNe was photometrically complete. I therefore set $\epsilon_{\rm phot} = 1$.

Furthermore, I have searched for and recovered the SLSN candidates that were not spectroscopically classified and that exploded in this effective volume-time, as described in Chapter 4. I considered this search to have discovered all SLSNe which exploded in the effective volume-time[1]. I therefore set $\epsilon_{\rm spec} = 1$. I note here that this does not mean that DES-SN obtained spectra for all candidates within some redshift range, but rather that the candidates that were not spectroscopically confirmed were nonetheless recovered and included in the volumetric rate computation.

The culmination of the work of Chapters 3 and 4 is that Equation 5.1 could be simplified to,

$$R = \frac{1}{V\,\Delta T} \sum_{i=1}^{N} 1 + z_{\rm i}. \tag{5.5}$$

5.2 Final sample of SLSNe

The photometric search of Chapter 4 resulted in a sample of 44 objects after removing spectroscopically classified non-SLSNe. 11 of the 44 objects were outside of the photometrically complete effective volume-time. These

[1]In practise a small number of SLSNe may have failed the selection criteria. However, none of these are found by the machine learning pipeline of Chapter 6, in support of this assumption.

11 objects did not explode in the volume or the temporal region I used to compute the rate, and they were henceforth excluded from the sample. For example, Figure 5.3 demonstrates the exclusion of DES17C3gyp.

Of the 33 that remain, 6 were spectroscopically confirmed SLSNe and 27 were unclassified SLSN candidates. To compute the rate using Equation 5.5, the redshift of each of these objects needed to be either measured or estimated.

Sources of redshift information

The redshift information I used for each of the objects is presented in Table 4.2, and a summary is given here. The DES-SN program obtained redshifts from the spectra of the 6 spectroscopically classified SLSNe that were in the final sample of 33 objects. Host galaxy spectroscopic redshifts were available for 3 of the remaining 27 SLSN candidates.

Of the 24 objects in the sample that lacked a spectroscopic redshift of either the SN or host galaxy, 7 had a host galaxy photometric redshift available. Photometric redshift estimates in DES are described in Sánchez et al. (2014) and Gschwend et al. (2018). In Figure 5.2, I plot the photometric redshift against the spectroscopic redshift for 13,677 galaxies from `SNGALS` to check their reliability. This figure shows that the majority of the photometric redshifts were well estimated, although on an individual basis there were a minority of photometric redshifts which did not match the spectroscopic redshift of their corresponding host.

The host galaxies of the remaining 17 objects were not detected in the single epoch DECam images, and therefore spectroscopic and photometric redshift estimates were not available. I attempted to derive photometric redshifts from the observed lightcurves of these objects, but the uncertainty on these estimates was unacceptably large. Instead, I have devised a method to systematically account for the large uncertainty in the redshifts of these objects using a Monte Carlo simulation, which is detailed in the next section.

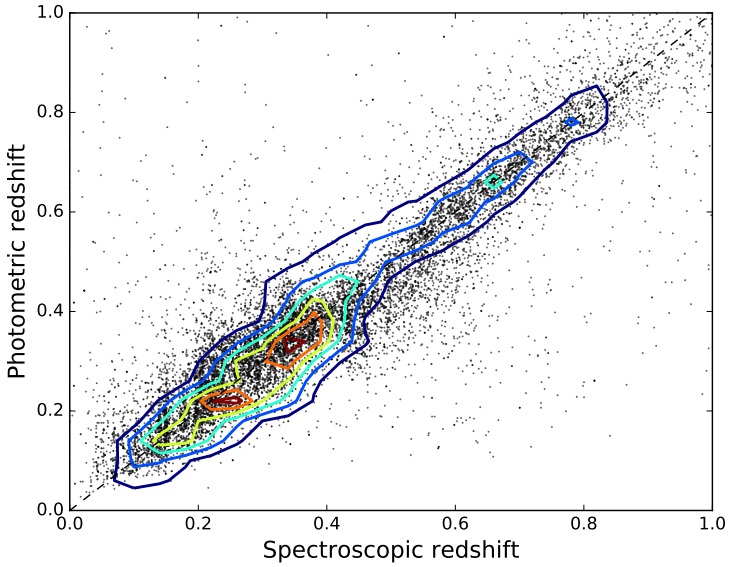

Figure 5.2: Photometric redshift against spectroscopic redshift for 13,777 DES galaxies. The black points are individual galaxies, while the contours indicate the galaxy count within 2D histogram bins. The vast majority of the photometric redshifts of DES-SN host galaxies were reliable, and I used seven of these in my rate computation when the spectroscopic redshift was not available.

5.3 Monte Carlo Computation of the Rate

To compute the rate I employed a Monte Carlo simulation method. Monte Carlo simulations are generally used to characterise some target quantity from known or assumed distributions of related parameters. First, a set of parameters is randomly drawn from the known distributions. Then, these parameters are propagated through an analysis pipeline relating the parameters to the target quantity. This process is repeated many times, each time selecting a new random set of parameters, and iteratively building up the distribution of the target quantity. In the case of my analysis, the distributions of parameters are the redshift distribution of the SLSN sample and the effective volume-time (although this is relatively well constrained), and the target quantity to be characterised is the volumetric rate.

Assuming a redshift

To compute the rate, I first assumed a redshift distribution which was sensible for the SLSNe with unknown redshifts to follow. If the rate was constant with comoving distance, the underlying distribution of SLSNe as a function of redshift would have the same functional form as the comoving volume element dV of the universe. Meanwhile, the explosion date of the unknown objects is well constrained by the last non-detection before the lightcurve begins to rise. The limits of the redshift distribution are assumed to lie at the boundaries of the photometrically complete region at this fixed explosion date, as can be seen in Figure 5.3. I used this assumed redshift distribution to iteratively draw random redshifts z_i from the range defined on an object-by-object basis, and with a probability weighted by the normalised dV.

Calculating absolute magnitudes

As stated in Chapter 3, the completeness of a sample can be improved by imposing a magnitude limit $M_{\rm lim}$ such that objects fainter than $M_{\rm lim}$ are not included. Faint SNe will fall beneath the detection limit of DECam more

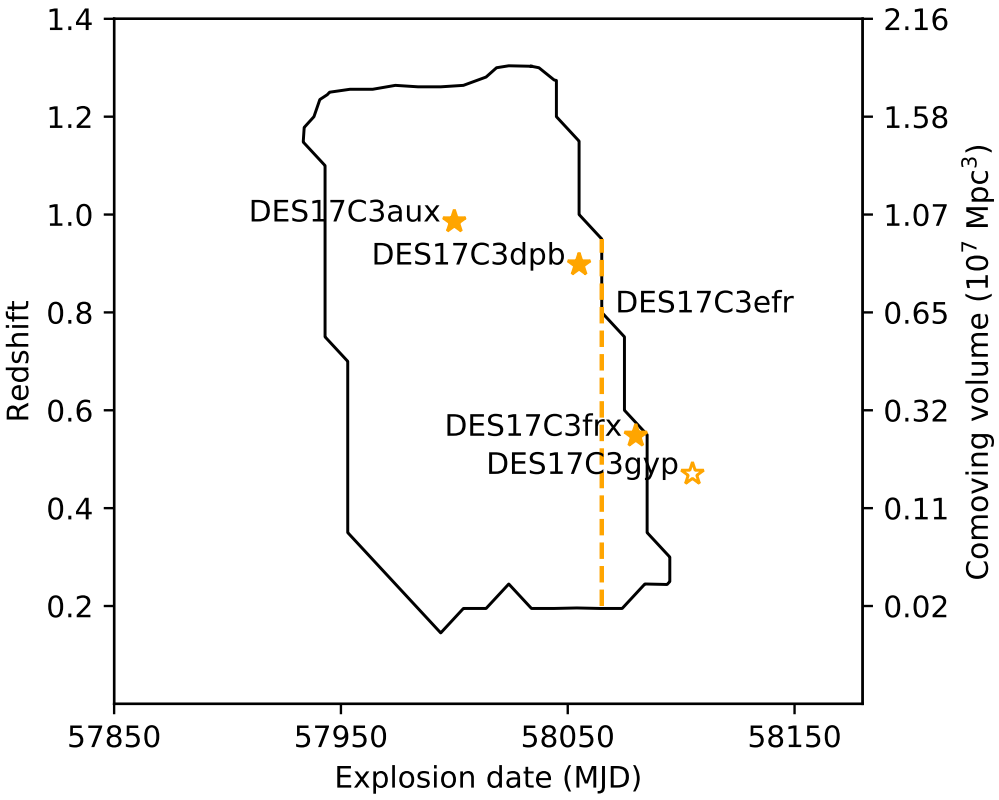

Figure 5.3: The photometrically complete region in Y5 of field C3 is shown as the black contour. The transformation of redshift to the comoving volume bounded by the field at that redshift is shown on the vertical axes. The redshift and explosion date of sample SLSNe and candidates are shown as orange stars. DES17C3gyp was outside of the photometrically complete region, and was not included in the rate measurement. The redshift of DES17C3efr was unknown, but was assumed to lie along the orange dotted line.

quickly than bright supernovae. To maintain the completeness of the sample, and to remain consistent with the selection criteria used in my photometric simulations, I have chosen a magnitude limit, $M_{\rm i} < -19.8$, such that the remaining sample was complete within the effective volume-time. Additionally I required that the objects had a realistic peak magnitude for a SLSN, $M_{\rm i} > -23.5$, given the assumed redshift, else they were discarded from the sample on that iteration. To enforce these criteria, I calculated the absolute magnitudes of the objects in the following manner.

I first interpolated[2] the lightcurves (of a nominal 7 day cadence) to find the true peak, and then modified the absorbed black body SED model of Chapter 3 to fit only a single epoch. For objects whose redshift was known, I fit this single epoch SED to the observed peak to find the radius R, temperature T, and absorption parameter $l_{\rm B}$ of the peak. I then de-redshifted the single epoch SED to a distance of 10pc, and integrated through the DES filters to compute the absolute magnitude.

For the objects without redshift information, I defined a grid of redshifts $0.05 \leq z \leq 1.5$, with 20 steps. I then computed the absolute magnitude using the technique described above, but this time for the entire grid of redshifts. This resulted in a relation between redshift and absolute magnitude for each object, which was logged. When the assumed redshifts, $z_{\rm i}$, were generated, the corresponding absolute magnitude was then retrieved from these look-up tables. Naively I might have used the simple equation $\mu = m - M$ to compute the absolute magnitude from the redshift and observed magnitude, but this does not account for the K-correction (Wirtz, 1918; Hubble, 1936; Hogg et al., 2002), which is significant at high redshift.

Monte Carlo simulation

I began the Monte Carlo computation by drawing redshifts for the unknown objects from the distributions described above. I also selected an effective

[2]I used a machine learning technique called Gaussian processes. More details of Gaussian processes are given in Chapter 6.

volume-time $V\Delta T_{\rm i}$ from a normal distribution characterised by $V\Delta T = (12.96 \pm 1.17) \times 10^7\,{\rm Mpc}^3\,{\rm yr}$ (Section 5.1.1). Using the assumed redshifts, I retrieved absolute magnitudes and applied the absolute magnitude cuts described above, and thereby obtained an intermediate sample of size $N_{\rm i}$. Then, using the effective volume-time and redshifts of this intermediate sample, I calculated a single measurement of the rate using Equation 5.5.

I then re-selected the redshifts for the unknown objects and an effective volume-time, retrieved absolute magnitudes, made the magnitude cuts as before, and found a new intermediate sample of size $N_{\rm i+1}$. The rate was calculated from the new sample, which resulted in a second measurement. This process was iterated 10^5 times, which allowed me to build up the distribution of possible SLSN rates shown in Figure 5.4. The average sample size after applying the peak absolute magnitude cut was $\overline{N} = 15$, which I use to compute the statistical (Poisson) error in Section 5.3.1.

5.3.1 Error analysis

The distribution of possible volumetric rates is shown in Figure 5.4. I fit a lognormal PDF to this asymmetric distribution to find the result and systematic error. I normalised the PDF and computed the cumulative distribution function (CDF) using a simple summing algorithm. This allowed me to find the mean and systematic error of the rate measurement, given by the 16th, 50th and 84th percentiles of the CDF, shown by vertical lines on Figure 5.4.

To calculate the statistical error, I found the symmetric Poisson interval $\sigma_{\rm N}$ for the average sample size after the absolute magnitude cut; $\overline{N} = 15$. The Poisson interval is used when counting a small integer number of events. From the Poisson intervals I found the fractional error $\sigma_{\rm N} \,/\, \overline{N}$. The statistical error was then the mean volumetric rate multiplied by this fractional error.

The Volumetric Rate of Superluminous Supernovae

The final result of the volumetric rate of SLSNe-I from DES is,

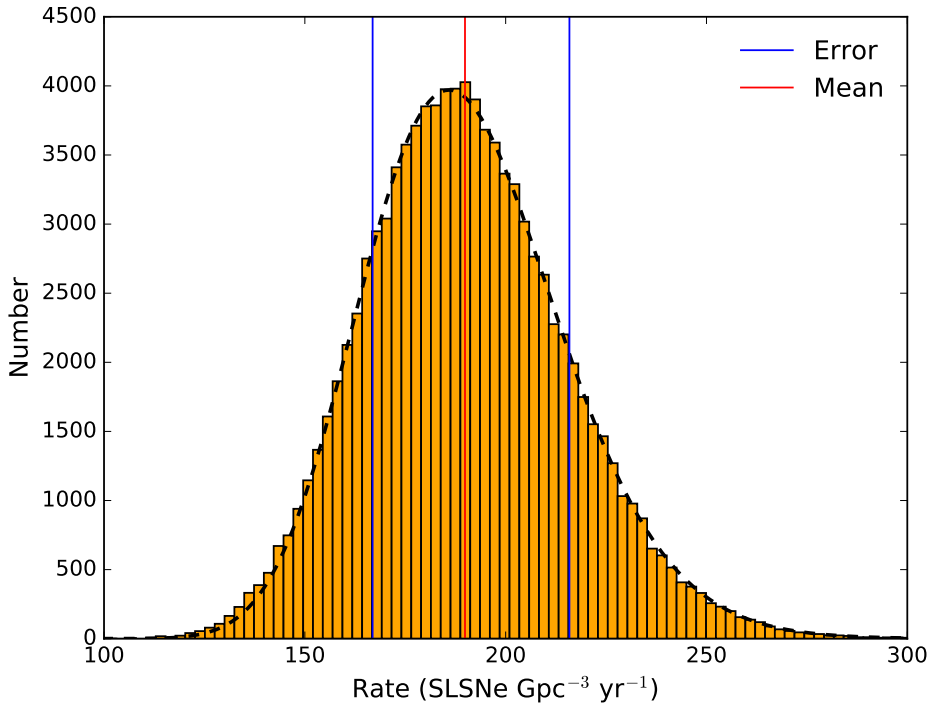

Figure 5.4: The distribution of the volumetric rate of SLSNe from my Monte Carlo simulation. A lognormal PDF was fit (dotted line) to the asymmetric distribution to evaluate the final result. The mean and 68% confidence region of this PDF are shown as red and blue vertical lines, and defined the final result and systematic error of my rate computation.

$$R_{\rm V} = 190\,^{+26}_{-23}\,({\rm sys}) \pm 52\,({\rm stat})\,{\rm SLSNe\,yr^{-1}\,Gpc^{-3}}, \tag{5.6}$$

at a volume weighted mean redshift of $\overline{z} = 0.797$. The systematic error is from the 68% confidence region of the lognormal PDF fit to the Monte Carlo simulated distribution of the rate (Figure 5.4). The statistical error is from the Poisson interval on the mean sample size $\overline{N} = 15$ after the absolute magnitude cut. A detailed discussion of both the result and error analysis is given in Section 5.3.2.

5.3.2 Discussion

Comparison to previous results

I compare my measurement of the volumetric rate of SLSNe-I to other measurements from the literature in Figure 5.5. The total error shown is given by the quadrature sum of the systematic and statistical errors. The horizontal errors of both my work and the Prajs et al. (2017) measurement show the redshift range of objects used in the computation. Details of the literature measurements are given in Chapter 1. Solid points and their error bars show volumetric rates of the hydrogen-poor SLSNe-I, while empty points with dotted error bars show rates of SLSNe-I and SLSNe-II combined for comparison.

The cosmic star formation history (SFH) with the functional form of Cole et al. (2001), is shown as the black dotted line,

$$SFH = k\,\frac{(a+bz)}{(1+(z/c)^d)}\,h\,{\rm M_\odot\ Mpc^{-3}\ yr^{-1}} \tag{5.7}$$

where *a, b, c* and *d* are parameters from Hopkins & Beacom (2006), z is the redshift, and h is the dimensionless Hubble parameter. If the progenitors of SLSNe are massive stars, I expect that the rate should follow the cosmic SFH due to the small time delay between formation and subsequent explosion of these stars. I introduced the normalisation constant, k, to Equation 5.7 to scale the cosmic SFH to the volumetric rate of SLSNe. In Chapter 1,

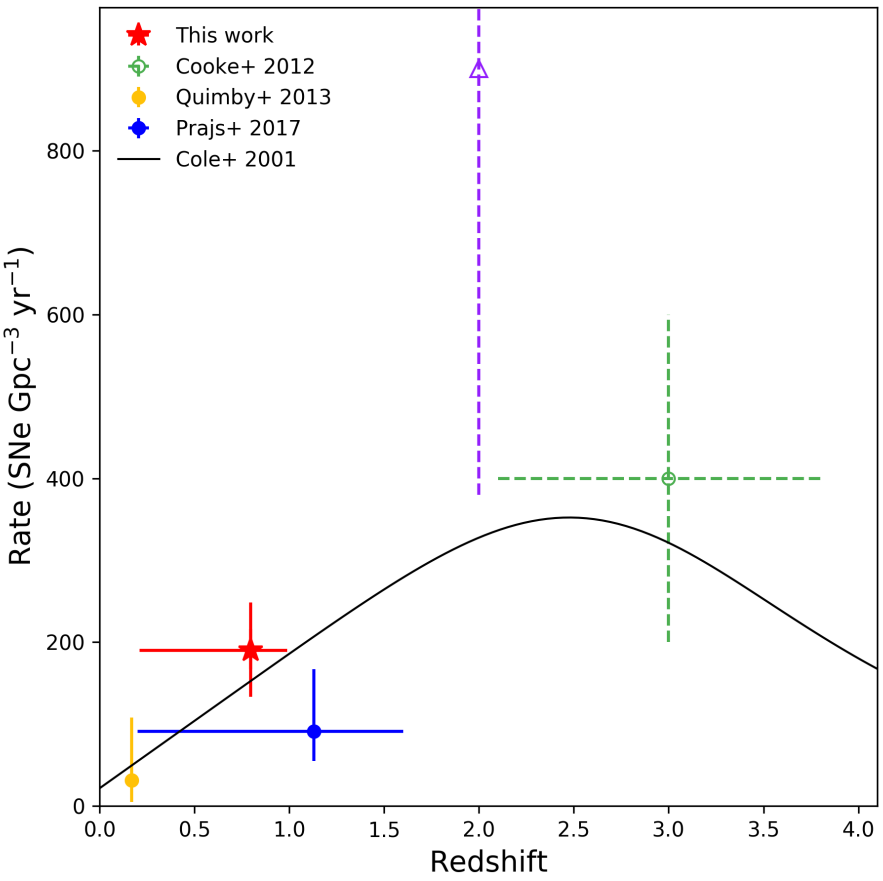

Figure 5.5: Comparison of the volumetric rate of SLSNe-I to previous measurements. The three measurements at $z < 1.6$ are of the SLSNe-I rate, while the dotted points at higher redshift used SLSNe of uncertain subtype, and are shown here for comparison. The black line is the cosmic star formation history, with a normalisation constant fit to the three SLSN-I rate measurements.

the normalisation constant of the cosmic SFH was scaled to match the low redshift measurement of Quimby et al. (2011), as had been done previously (Prajs et al., 2017). In light of the work of this thesis, I refit k to the three current measurements of the SLSN-I rate, but not to the two measurements of all SLSN types at high redshift. This increased k by 36%, or 1.4σ, and therefore I found no compelling evidence for a higher rate than had been previously estimated. Indeed, Figure 5.5 shows that my measurement is consistent with the Prajs et al. (2017) rate of SLSNe-I at a similar redshift.

However, the faintest SLSN-I in the sample of Prajs et al. (2017) had a peak magnitude $M_{\rm u} = -20.9$, while I used a lower peak magnitude cutoff of $M_{\rm i} = -19.8$. Therefore the Prajs et al. (2017) selection of SLSNe from SNLS may have missed fainter members of the SLSN spectroscopic class, which if included would have pushed their rate higher. Due to the increased sensitivity of the DES-SN search, it was able to observe both spectroscopic SLSNe and SLSN candidates that were observationally fainter than had previously been possible, and a slightly higher rate from the DES sample might have been expected. Further measurements could determine this. For example, the Pan-STARRS sample of 17 SLSNe-I (Lunnan et al., 2018) would give an additional rate measurement at a similar redshift.

On the other hand, the presence of spectroscopically classified contaminants in the sample resulting from my search for photometric SLSN candidates indicates that a small number of non-SLSNe may have entered the sample used to compute the rate. However, it is not yet possible to securely classify the SLSN candidates from their photometry alone, and I assume that all objects without spectroscopic classifications are good SLSN candidates.

Furthermore, I assumed that the SLSN candidates without a known redshift must have exploded within the photometrically complete regions defined by the simulations of Chapter 4. If they had instead exploded at higher redshift, as is perhaps implied for objects which were too faint for spectra to be obtained, then they would have fallen outside of the complete regions, and would not have been included in my rate computation. In that case my rate

may be overestimated. On the other hand, these objects may have been on the faint end of the SLSN distribution and at lower redshift, in which case they should lie in the photometrically complete regions.

Systematic and statistical errors

I note here that this measurement of the volumetric rate is limited by the statistical error on the mean sample size of 15 objects, which gives a 27% error. The dominant source of systematic error in my rate measurement is the number and redshift of the hostless SLSN candidates that exploded in the photometrically complete regions. I also estimated the contribution from the error on the peak magnitude, peak time, and binning resolution to the systematic uncertainty in the effective volume-time in Chapter 3. These are the uncertainties that contribute to the Monte Carlo distribution of possible volumetric rates shown in Figure 5.4, and give a total systematic error of 13%.

Throughout the Monte Carlo simulation the sample size varied as a result of the embedded absolute magnitude cut. Therefore, some fraction of the statistical Poisson error may have been included in the systematic error. However, this systematic error was less than the Poisson error on 15 objects, and it cannot account for the entire statistical error. For that reason, and lacking another means to estimate the statistical error, I have included the statistical error in addition to the systematic error from the Monte Carlo. If I had not included this Poisson error, the total error would have been underestimated. In this case however, the total error may have been slightly overestimated, but I have chosen this as the most conservative estimation of the total error. For future measurements of the volumetric rate, a more detailed understanding of the systematic error will be crucial as much larger samples of SLSNe-I become available, and these analyses become limited by their systematics.

Other sources of systematic error included the uncertainty in the cosmological parameters that are used to compute the comoving volume (Equation

5.2). These parameters have been measured by e.g. the Planck satellite (Planck Collaboration et al., 2018), who found a 1%, 3% and 1% error on H_0, $\Omega_{\rm M}$ and Ω_Λ respectively. Including the effect of discrepant measurements of H_0 would have increased the potential contribution of that parameter to $\sim$5%. These contributions are lower than both the statistical and systematic effects described above, and I considered cosmological contributions to the systematic error to be negligible.

High redshift measurements

Finally, it is clear that more work is needed to constrain the volumetric rate at $z > 1.6$. While the current work, as well as Quimby et al. (2013) and Prajs et al. (2017), have measured the volumetric rate for SLSNe-I at low and intermediate redshift, Cooke et al. (2012) and Moriya et al. (2019) have estimated lower bounds to the rate of all SLSN types at higher redshift. It is challenging to constrain the spectroscopic and photometric efficiencies at these redshifts as SLSNe at the lower end of the luminosity function fall below the detection limit of spectroscopic and imaging facilities. It is also difficult to obtain a secure sub-classification from high redshift spectra both due to a low signal to noise and because any prospective Hα lines will be redshifted out of the wavelength range of spectroscopic facilities. Nonetheless, current and future facilties such as ZTF (Graham et al., 2019), LSST (Villar et al., 2018) and Euclid (Inserra et al., 2018b) will observe large samples of SLSNe both at low and high redshift, allowing more precise measurements of the high redshift SLSN rate, which may constrain the turnover of the cosmic SFH. More details of the predicted samples of SLSNe from ZTF, LSST and Euclid are given in Chapter 7.

5.4 Conclusion

In this chapter I have brought together the work of Chapters 3 and 4 to compute the volumetric rate of SLSNe from DES. I began by presenting

the volumetric rate equation and defining the parameters required for its computation (Equation 5.1).

I calculated the sky area of the DES-SN fields by considering the pixel scale and CCD layout of DECam. I then used Equation 5.2 to compute the effective volume-time of the survey given the simulations over redshift and explosion date of the spectroscopic SLSN sample from Chapter 3.

I discussed the final sample of SLSNe which both meet my selection criteria and that were within the effective volume-time of the survey. I selected the effective volume-time in which the survey search for SLSNe was photometrically complete for objects with $M_{\rm i} < -19.8$. I searched for and recovered the photometric candidates within this effective volume-time in Chapter 4. These two steps allowed me to set the detection efficiency, $\epsilon = 1$, in Equation 5.1.

I presented the sources of redshift information for the final sample of 33 objects. 9 of these had spectroscopic redshifts from the SN or host galaxy spectrum, 7 had photometric redshift estimates from the host galaxy photometry, and 17 were hostless and had no redshift information available.

I described the Monte Carlo simulation method used to accommodate for the uncertainty in both the effective volume-time and the redshifts of hostless objects. This required me to assume an underlying redshift distribution. I then iteratively assigned random redshifts from this distribution to the 17 unknown objects, calculated the absolute magnitudes, and based on the criterion, $-19.8 \leq M_{\rm i} \leq -23.5$, either included or excluded them in each iterative rate calculation. I thereby built up the distribution of rates shown in Figure 5.4.

I fit a lognormal PDF to this asymmetric distribution, and derived the final rate result and systematic error from the mean and 68% confidence region of the corresponding CDF. I computed the statistical error using the Poisson interval for a small integer number of events. I presented my final volumetric rate measurement from DES,

$$R_{\rm V} = 190\,^{+26}_{-23}\,({\rm sys}) \pm 52\,({\rm stat})\,{\rm SLSNe\,yr^{-1}\,Gpc^{-3}}, \tag{5.8}$$

at a volume weighted mean redshift of $\overline{z} = 0.797$. I compared my result to SLSN volumetric rates from the literature, and found that these were largely consistent. Finally, I considered the effect of the assumptions that were made both in this work and in previous measurements, discussed the systematic and statistical errors, and considered the effect that future samples of SLSNe-I will have on high redshift volumetric rate measurements.

Chapter 6

Machine learning with the DES-SN catalogue

The work detailed in this chapter is entirely my own, except for the Gaussian processing of DES-SN lightcurves in Section 6.2, which was done in collaboration with M. Pursiainen. References to other works, where necessary, are given throughout.

In this chapter I exploit machine learning algorithms to explore the DES transient catalogue in a search for anomalous transients, including any SLSNe which may have been missed by the photometric search of Chapter 4, as well as other unusual objects. I begin by describing some of the nomenclature used in the field of machine learning. Machine learning algorithms are broadly separated into two distinct groups.

The first are 'supervised' machine learning algorithms. Supervised learning algorithms create an informative model using both the input data and outputs (classes, or labels). The broad area of supervised learning is separable into two primary types of algorithms; classification and regression algorithms. Classification algorithms have the capability to automate the categorisation of objects into some predefined discrete classes. Regression algorithms predict a target variable given a number of predictor variables.

The second are 'unsupervised' machine learning algorithms. Unsupervised learning algorithms create an informative model of the relationship among data points[1] using only the input data. These algorithms detect commonalities among data points, and thereby reveal hidden structure in the data. The most common type of unsupervised learning algorithms are clustering algorithms, in which the commonalities among data points are quantified, and similar data points are grouped together into clusters. Another regularly used class of unsupervised learning algorithms are dimensionality reduction algorithms, in which the number of features (i.e. dimensions) of a dataset are reduced. Dimensionality reduction is particularly useful both to remove degeneracy among features, and to allow otherwise computationally unfeasible tasks to be tractable by computers of limited computational power.

In recent years the field of machine learning has seen a wide range of applications in astronomy due to both the increase in the quantity and complexity of astronomical datasets, and the increase in availability and power of computational resources. Astronomical applications of machine learning have so far included the separation of galaxies and point sources in large astronomical datasets (e.g. Morice-Atkinson et al., 2018), the classification of galaxy morphologies (e.g. Barchi et al., 2019), the detection of strong gravitational lenses (e.g. Hartley et al., 2017), and exoplanet transit detection (e.g. Schanche et al., 2019). Recently, it has been shown that one of the most prolific and promising applications of machine learning in astronomy is in the classification of astrophysical transients (Lochner et al., 2016; Narayan et al., 2018; Sooknunan et al., 2018; Muthukrishna et al., 2019; Mahabal et al., 2019; Möller & de Boissière, 2019). The increasing volume of data produced by astronomical surveys combined with the short time for which the objects are visible means that it is vital to photometrically classify these transients in real time. This photometric classification is required not only to

[1]For example, the data points could be a parameterisation of images, videos, audio time series, or SN lightcurves.

select samples for population studies and cosmological analyses (in the case of Type Ia SNe, e.g. Kessler et al. 2010), but also to prioritise subsequent spectroscopic observations in order to test the reliability of the photometric classifications (D'Andrea et al., 2018).

In addition, machine learning can be applied to large astronomical data catalogues in an unsupervised clustering approach. In Chapter 4, I described the method I used to select a photometric sample of SLSNe for the computation of the volumetric rate of Chapter 5. During this process it became apparent that there were many unusual transients in the DES transient catalogue which did not fit into the traditional classification scheme of SNe. This suggested that there is significant potential for interesting discoveries in the DES catalogue.

In this chapter I detail the systematic pursuit of these elusive and unusual objects. I have chosen an unsupervised machine learning approach with the intent to discover astrophysical transients which were outside of the mainstream classification of SNe. I first describe the preprocessing steps required to clean the data from observational artefacts and spurious detections in Section 6.1. I elucidate the interpolation of the lightcurves using Gaussian processes in Section 6.2. I detail the method used for feature extraction known as the stationary wavelet transform in Section 6.3. I follow this with dimensionality reduction using principal component analysis (PCA) in Section 6.4, and then project these principal components onto a two dimensional surface, leading to the emergence of visual similarities in the dataset in Section 6.5. Finally, I show some of the unusual transients discovered by this analysis in Section 6.6, and conclude in Section 6.7.

6.1 Preprocessing

Of the 28,184 objects in the catalogue of Gaussian processed lightcurves (Section 6.2) of DES-SN transients, many were spurious detections or artefacts produced as a result of difference imaging. As detailed in Chapter 2,

a supervised machine learning algorithm called `autoScan` (Goldstein et al., 2015) is used to score the subtracted images with a probability that the image is an artefact or a real astrophysical transient, where a score of 1 represents a high probability of a real astrophysical transient and a score of 0 represents an artefact. Epochs were considered to have passed the `autoScan` test if they score 0.3 or better (Kessler et al., 2015; D'Andrea et al., 2018).

I began by making a simple selection to remove a large number of the spurious transients from the sample. The number of detections with a signal to noise ratio SNR ≥ 5 is quantified by the parameter `numepochs` in the DES-SN database, while the number of these detections which pass `autoScan` is quantified by `numepochs_ml`. Figure 6.1 shows the distribution of the ratio $R_{\rm ml}$ = `numepochs_ml`/`numepochs`. 13,005 of the total 28,184 objects had all epochs passing the `autoScan` test ($R_{\rm ml} = 1$). Visual inspection of a random subset of the lightcurves showed that; (1) objects that were good candidates for real astrophysical transients had a score $R_{\rm ml} \geq 0.5$ and (2) objects that were obviously spurious detections with unrealistic lightcurves had $R_{\rm ml} < 0.5$. I have therefore chosen a threshold of $R_{ml} \geq 0.5$ and selected only objects that pass this criterion. This removed 27% of the objects.

6.2 Gaussian processes

To run a dimensionality reduction procedure on the remaining sample of 20,588 objects, the lightcurves of these objects needed to be interpolated such that the epochs were on a uniform grid. M. Pursiainen (University of Southampton) has used a technique known as Gaussian processes to interpolate all of the DES transient lightcurves, using the `python` package `George`[2].

Gaussian processes are a class of functions which may be used to model the correlated noise within a time series dataset. The Gaussian processed lightcurve $f(x)$ is constructed from two components, the mean function $\mu(x)$ and the covariance function $k(x, x')$ which describes the correlation among

[2]http://dfm.io/george/current/

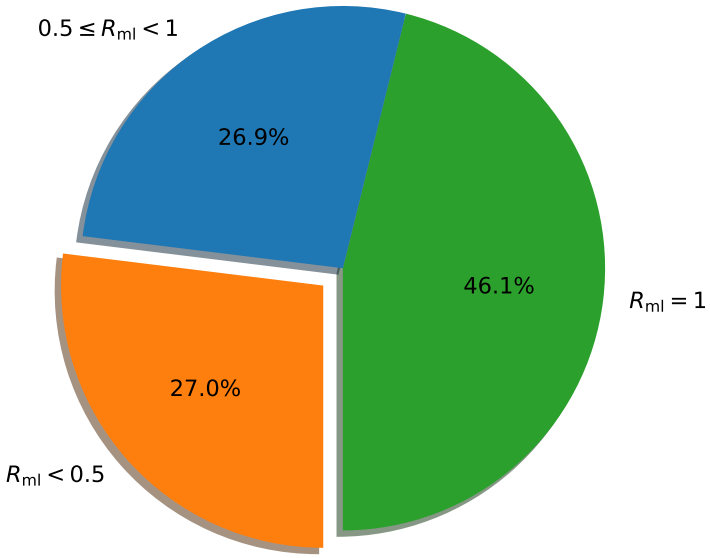

Figure 6.1: The distribution of the ratio $R_{\mathrm{ml}} =$ `numepochs_ml`/`numepochs`. This parameter R_{ml} was used to initially select objects for which the majority of detected epochs passed the machine learning `autoScan` test. Objects with $R_{\mathrm{ml}} < 0.5$ were discarded.

the uncertainties in lightcurve epochs x and x'. In other words,

$$f(x) = GP(\mu(x), k(x, x')). \tag{6.1}$$

Gaussian processes can be considered as a generalisation of the Gaussian distribution, where the value and uncertainty of each point of the time series function is represented by a normal distribution. Adjacent points are correlated, with a covariance matrix given by the predetermined kernel $k(x, x')$. The advantage of using Gaussian processes over traditional parametric astrophysical modelling techniques is that any systematic source of uncertainty in the data is implicitly marginalised over as a result of the choice of kernel $k(x, x')$, whether or not the source of the systematic uncertainty is well understood.

In the case of the DES transient catalogue, an exponential squared kernel was chosen as the form of the covariance matrix,

$$k(x, x') = \exp(-\frac{|d|^2}{2l^2}), \tag{6.2}$$

where $d = x - x'$ and l is the characteristic length scale over which the data vary (i.e. how close data points x and x' had to be to significantly influence one another). This kernel was chosen due to its simplicity (a single parameter), and because a fast computation was required to model 28,184 lightcurves. The hyperparameter value was optimized using a log likelihood minimization method to obtain the best possible fit to each season of the data in each band. In other words, a separate value of l was used for each band in each season, and so for a single transient there were 4 bands $\times$ 5 seasons = 20 values of l. This method was chosen as while some transients vary on fast timescales (e.g. rapidly evolving transients, Pursiainen et al. 2018) others vary on much slower timescales (e.g. SLSNe), and therefore different kernel hyperparameters are required to capture both fast and slow lightcurve evolution.

Typical Gaussian processed lightcurves, $f(x)$, are shown in Figure 6.2. The fluxes measured by DES are shown as solid circles with error bars, while

the Gaussian processed lightcurves are shown with centroids depicted as solid lines with the surrounding translucent contours depicting the one sigma uncertainty. It can be seen from this plot that both the overall lightcurve shape and smaller scale fluctuations were well captured by the Gaussian process technique. Only the flux centroids were used hereafter.

The Gaussian processes were originally carried out to interpolate the lightcurves to a half-day cadence, giving nearly 2000 features per filter, or 8000 per object. Adjacent data points in the GP lightcurves are highly correlated due to their smooth variation. Therefore, for this analysis the lightcurves were resampled to a 5 day cadence, (every 10th sample was retained), without significant loss of information (especially given the nominal 7 day cadence of DES-SN), leaving 800 features per object.

In the following section, I describe the next stage of the feature selection process, the stationary wavelet transform.

6.3 Stationary wavelet transform

Traditionally the field of signal processing has made extensive use of the Fourier transform to decompose periodic signals into their constituent frequencies for further analysis. Classical Fourier analysis assumes that the constituent frequencies are infinite in duration, and Fourier transforms suffer from the fact that the decomposed signal does not retain any information on the temporal location of the frequencies. If a given frequency only exists at a specific temporal location in the signal or for a short duration then it becomes impossible to reconstruct the signal in the time domain.

Attempts have been made to solve this issue by dividing the time domain signal into finite regions, and performing the Fourier transform on these regions. An issue with this short-time Fourier transform (Gröchenig, 2013) is that an increasing resolution in the time domain, gives a decreasing resolution in the frequency domain. Thus, temporal location and frequency are an example of complementary variables, and the precision with which these can

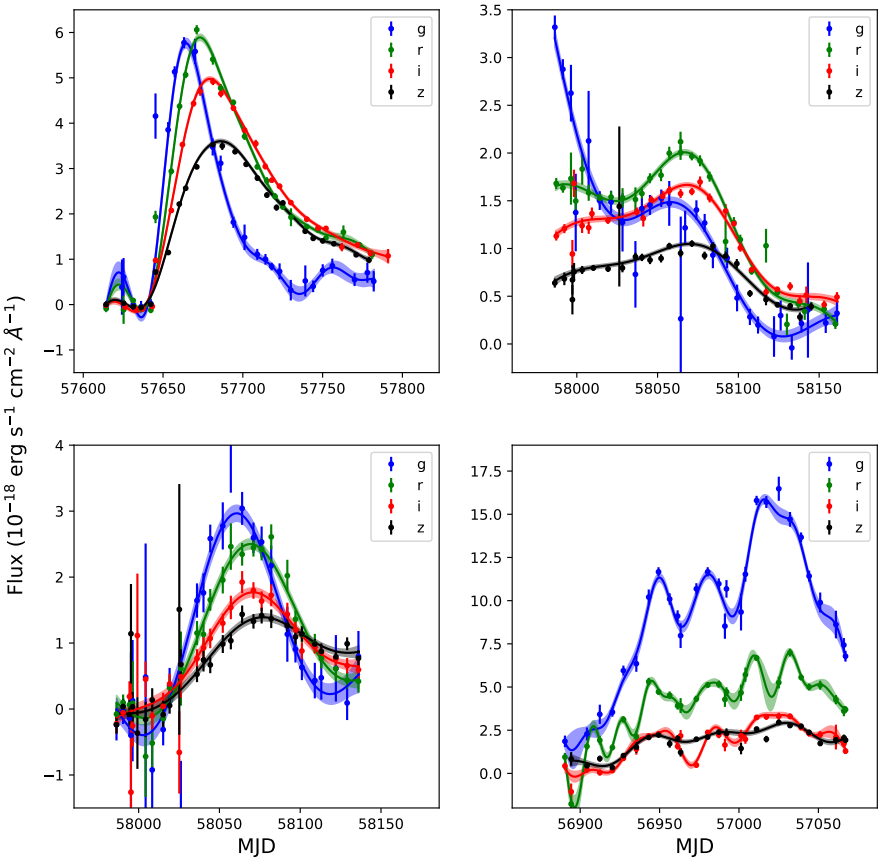

Figure 6.2: Example single season lightcurves fit with Gaussian processes. The circles depict the flux values and uncertainties measured by DES, while the solid lines and surrounding translucent contours depict the centroid and one sigma uncertainty of the Gaussian process fit. *Top left:* The SN Ib/c DES16X3bdj. *Top right:* The SN II DES17C3dw. *Bottom left:* The SLSN-I DES17X1blv. *Bottom right:* The AGN DES14C2nza.

be measured is fundamentally limited by the uncertainty principle.

Wavelet transforms (see Valens 1999 for a review) have become a popular tool for signal processing due to their ability to represent information in both the time and frequency domain simultaneously. The starting point of the wavelet transform is the continuous wavelet transform (CWT; Mallat 2008). The CWT is calculated by shifting a continuously scalable function over the signal and calculating the correlation between the two. The problem implicit in this method is twofold. Not only does one obtain an infinite number of wavelet coefficients, but these coefficients are highly redundant. Further, in most signals these correlations do not have analytic solutions, and must be computed numerically. An attractive feature of the CWT, however, is that it is translation and scale invariant. In other words, the CWT of a translated or resized signal is equivalent to the translated or resized CWT of the original signal.

The problem of redundancy is partially solved by the introduction of the discrete wavelet transform, which as the name implies, is not continuously shiftable and scalable but instead must be shifted and scaled in discrete steps. Whilst, under some additional conditions, this serves to remove the intrinsic redundancy of the CWT, it comes at the cost of the scale and translation invariance. The discrete wavelet transform of a signal and of a translated or scaled signal are not simply translated or rescaled versions of each other. This is an issue as an astrophysical transient may be observed by DES at any point during its lightcurve. For my analysis it was desirable for transients that were of the same class to lie close to each other in the similarity space regardless of the time in the DES observing season at which they happened to explode. In other words the wavelet transform of the transient lightcurves should have been translation invariant. Conveniently, the effect of cosmological time dilation can be mitigated by a wavelet transform which is scale invariant, as the transient lightcurves are stretched due to cosmological time dilation. Reddening effects in the spectral energy distribution however, cannot be approximated by any kind of invariance in the wavelet transformation.

To approximate translation and scale invariance I invoked the stationary wavelet transform (SWT; Holschneider et al., 1989). The SWT has been shown to be an excellent choice for feature extraction in machine learning transient classification algorithms (Lochner et al., 2016; Narayan et al., 2018; Sooknunan et al., 2018) as, while it approximates these translation and scale invariances, it is also fast to compute.

I used the `Pywavelets`[3] (Lee et al., 2006) `python` library to perform the SWT on the $20,588$ Gaussian processed lightcurves of Section 6.1. The lightcurve in each photometric passband was transformed independently, which resulted in two sets of coefficients per filter. These coefficients are known as the approximation and detail coefficients. As the name implies, the approximation coefficients represent the overall shape of the Gaussian processed lightcurve, while the detail coefficients represent small scale fluctuations in the lightcurve. A single-level SWT decomposes the signal into a single set of approximation and detail coefficients, while further levels would have decomposed the first-level approximation coefficients into second-level approximation and detail coefficients. An example SWT decomposed lightcurve is shown in Figure 6.3.

I used a single-level decomposition with the symlet family of wavelets, which are a more symmetric version of the commonly used Debauchies family of wavelets (Daubechies & Bates, 1993). This wavelet family was initally used for transient classification by Lochner et al. (2016), (and subsequently by Sooknunan et al. 2018 and Narayan et al. 2018), who found that the choice of wavelet family did not significantly alter their results in classification problems.

There were nearly 1600 data points for each transient that form the feature set for subsequent machine learning algorithms used in this chapter. This high dimensional dataset needed to first be dimensionally reduced such that it became feasible to run machine learning algorithms on reasonable time scales, as well as to mitigate the redundancy present in the current fea-

[3]https://pywavelets.readthedocs.io/

ture set. In the next section I describe the method of PCA I used to achieve this dimensional reduction.

6.4 Principal component analysis

PCA is a dimensional reduction technique which works by computing the eigenvectors of a (usually normalised) dataset and rotating the correlated features of that dataset such that the new independent but abstract features align with the eigenvectors. This can be thought of as rotating the axes of a graph such that the principal axis lies in the direction of greatest variance of the dataset and the subsequent axes are in the direction of the next greatest variance which is also orthogonal to all previous axes. The new abstract features (axes) are thereby ranked in order of the variance which the data exhibits in their direction. The first $N_{\text{components}}$ of these are retained while the components greater than $N_{\text{components}}$ are discarded as they have the least variance. It is this approach that allows PCA to reduce the dimensionality of the data while retaining as much of the information (variance) as possible. Through PCA one can thereby find the most descriptive set of abstract (rotated) features.

PCA was first invented by Pearson (1901) and later independently discovered and named by Hotelling (1933). However, it was the advent of electronic computers that made it feasible to compute PCA beyond trivially small datasets. Today, PCA is used extensively in a wide variety of fields, ranging from quantitative finance (e.g. Ghorbani & Chong, 2018) to neuroscience (e.g. Brenner et al., 2000). In astronomy, PCA has been critical to many analyses, especially in statistical studies of stellar spectra (e.g. McGurk et al., 2010), but also as a precursor to clustering analyses of SLSN nebular spectra (Nicholl et al., 2019), among others.

In this work I used PCA to reduce the dimensionality of the highly redundant coefficients from the stationary wavelet transform. The first step of many PCA analyses is to normalise the dataset such that each dimension

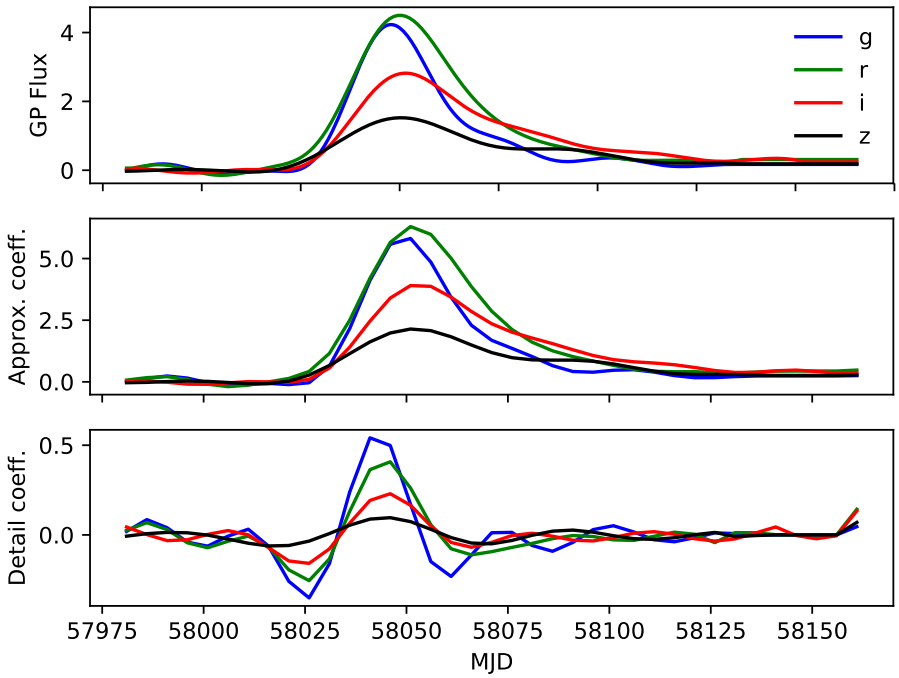

Figure 6.3: Feature extraction using a stationary wavelet decomposition for the well observed Type Ia SN DES17X3bhi. *Top:* The centroid values of the Gaussian processed lightcurve. *Middle:* The downsampled approximation coefficients plot against MJD. *Bottom:* The downsampled detail coefficients plotted against MJD. The two sets of coefficients are the features used in the rest of this chapter.

has a mean of zero and a variance of one, so that features with large values do not dominate. To achieve this I used the `StandardScaler` routine from the `scikit-learn` library[4].

The next step was to perform a PCA with the same number of principal components as there are features in the original dataset, and to study the contribution of each PCA feature to the total variance of the original dataset. This gave an indication of the number of features that were required to capture some predetermined fraction of the total variance. This is called the 'explained variance' and is shown in Figure 6.4. I have chosen to keep 22 of the PCA features while discarding the remaining 282, which resulted in a 22 dimensional dataset that retains $\gtrsim 70$ percent of the variance. In the next section I project this 22 dimensional dataset onto 2 dimensions, and thereby reveal the similarities that are inherent in the data.

6.5 t-distributed stochastic neighbour embedding

The t-distributed stochastic neighbour embedding algorithm (t-SNE; Maaten & Hinton 2008) is a method used to visualise high dimensional datasets in a lower (2 or 3) dimensional space. To achieve this, t-SNE computes the probability that the high dimensional data points x_{i} and x_{j} are nearest neighbours. This conditional probability is given by a Gaussian distribution on the high dimensional Euclidean distance separating the two, $|x_{\mathrm{i}} - x_{\mathrm{j}}|$. For nearby points this probability is relatively large, while for distant points it tends to zero. This results in a set of probabilities which describe the pairwise similarities among all data points in the high dimensional space.

The t-SNE algorithm then seeks to find a map of the data points in the low dimensional space which minimizes the Kullback-Leibler divergence[5] between

[4]https://scikit-learn.org/

[5]The Kullback-Leibler divergence is a quantification of the dissimilarity between two probability distributions (Kullback & Leibler, 1951).

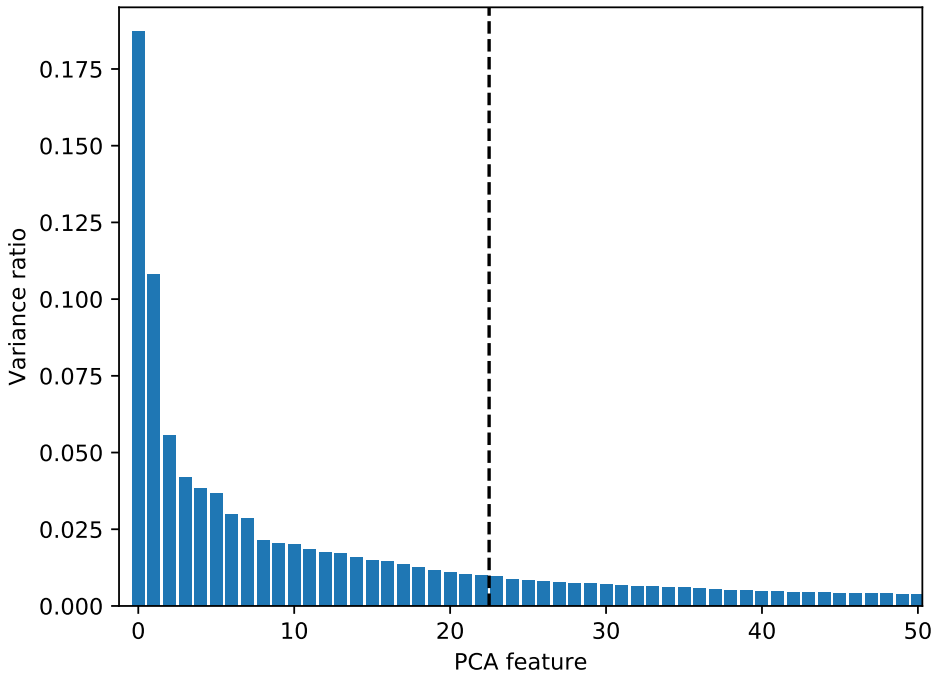

Figure 6.4: PCA variance ratio to determine the number of principal components to retain. On the vertical axis the variance ratio is the fractional contribution of the PCA features to the total variance of the dataset. The 50 features of greatest explained variance are shown here, of which I retained the first 22.

the probability distribution in the high dimensional space and an analogous probability distribution in the low dimensional space. The probability distribution in the low dimensional space, however, is computed using a Student's t-distribution (Student, 1908) rather than the Gaussian distribution used in the high dimensional space. A Student's t-distribution is chosen in order to simplify the cost function in the gradient descent, as well as to alleviate a well known problem in classical stochastic neighbour embedding known as the "crowding problem", in which moderately separated points in the high dimensional space have an undesirably large similarity (i.e. proximity) under a Gaussian distribution. As the Student's t-distribution has a larger probability in the tails, it allows for points with moderate probability in the high dimensional space to map to more distant locations in the low dimensional space, and thereby mitigates the crowding problem. The minimisation of the Kullback-Leibler divergence is achieved using a gradient descent method.

In the this work, I used the implementation of `t-SNE` from the `python` package `sklearn-manifold` to map the 22 principal components from Section 6.4 onto a two dimensional space, which revealed the similarities inherent in the dataset. The t-SNE plot is shown in Figure 6.5.

The stationary wavelet transform and the PCA required the lightcurves to lie on a uniform grid. However, the first season of DES-SN observations was 25 days shorter than the subsequent 4 seasons, and it was thus difficult to compare Y1 lightcurves to lightcurves of the other seasons without extrapolating the Y1 lightcurves, which is beyond the scope of this thesis. Objects detected in the first season of DES observations were therefore excluded.

While the t-SNE algorithm is usually used for visualisation purposes, unfortunately my time constraints have meant that further clustering analyses in the 22 dimensional PCA space have had to be delayed for future work. Nonetheless, in the following sections I present preliminary results using the t-SNE visualisation to search for anomalous lightcurves.

Obvious structures are apparent in the t-SNE plot. In order to gain insight into the meaning of these structures, the transients that were spec-

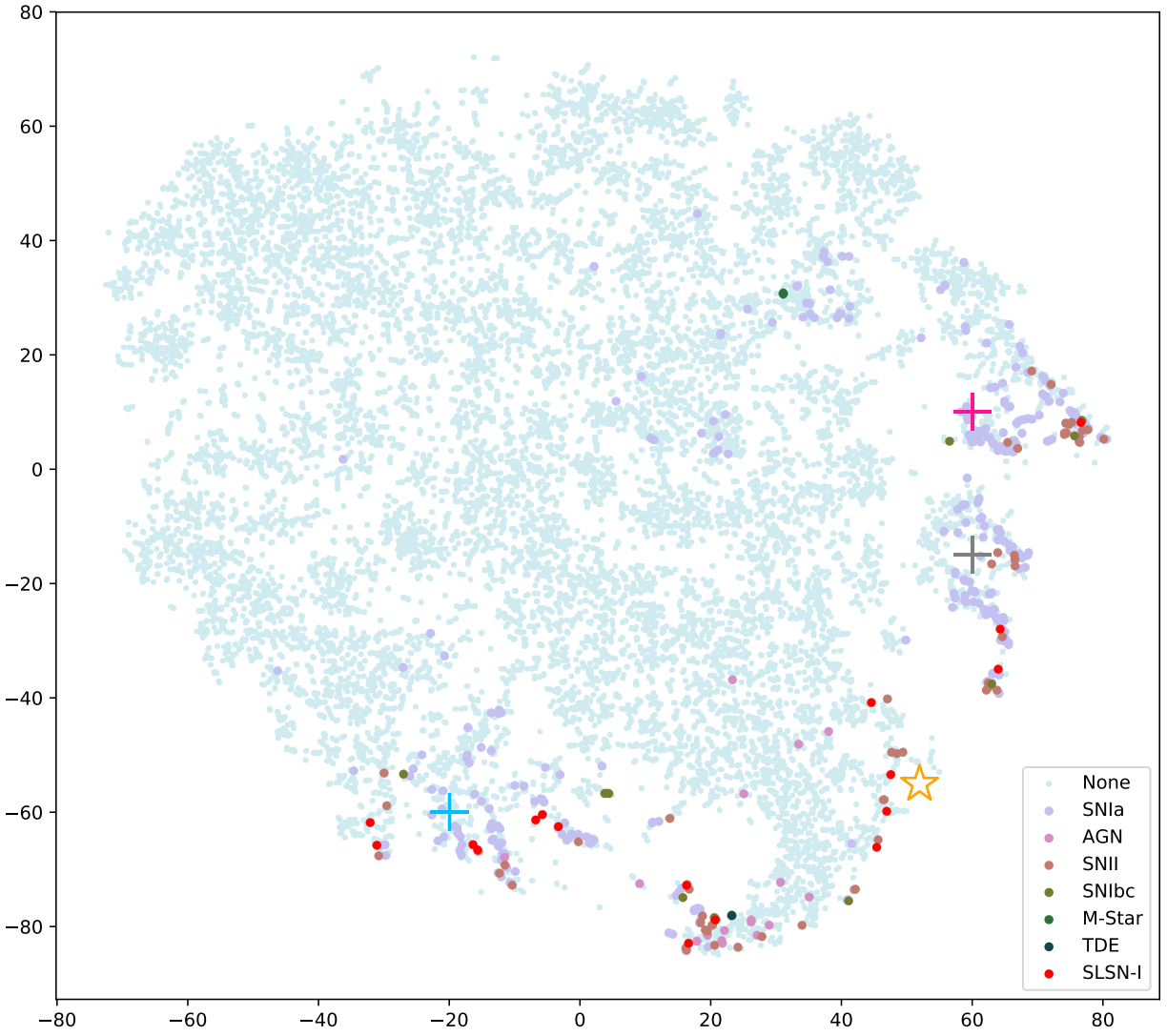

Figure 6.5: t-SNE visualisation of transients from the DES-SN catalogue. The axes are abstract. Transients with similar lightcurves should be close in proximity. Transients depicted as pale blue points were not spectroscopically classified. The crosses and star indicate regions referenced in the text. Spectroscopically classified SLSNe are of particular interest, and are shown here as red points.

troscopically classified by the DES-SN follow up program (Chapter 2) are shown in distinct colours. The majority of classifications were of Type Ia SNe, but there is significant contribution from Type II SNe, Type Ib/c SNe, SLSNe and AGN.

The vast majority of the parameter space is inhabited by unclassified transients. Investigation of a random sub-sample of these objects located at the top left and towards the center of the t-SNE figure showed that they are constituted almost entirely by spurious detections. Statistical fluctuations in the measured flux flagged epochs as containing transient light, when there was little evidence for genuine astrophysical variability. Lightcurves of a selection of these objects are shown in Figure 6.6.

The lower and right regions of the t-SNE visualisation were inhabited by almost all of the spectroscopically classifed SNe, indicating that the unclassified objects were also likely to be SNe. Visual inspection of a random sample of these lightcurves showed that regions located at approximately $(-20, -60)$ (blue cross), $(60, -20)$ (grey cross) and $(60, 10)$ (pink cross) in the t-SNE coordinates were largely inhabited by rising, centered, and declining objects respectively. This suggested that the t-SNE algorithm may have been unable to identify the similarity among objects of the same astrophysical class but whose lightcurves suffer from different temporal edge effects.

DES-SN was optimised to find SNe Ia, with less priority given to other SN types. Therefore, the vast majority of classifications were of SNe Ia. However, this bias obviously did not extend to the unclassified objects, and it is likely that the regions that contained a large number of classified SNe also included both unclassified normal SN types and anomalous SNe. Interestingly, spectroscopically classified objects that inhabited the elongated vertical region located around $(45, -50)$ (orange star) in the t-SNE visualisation were predominantly the longer duration Type II and superluminous SNe.

To find anomalous astrophysical transients in the DES-SN catalogue, it was thought that one could simply select the objects furthest from any obvi-

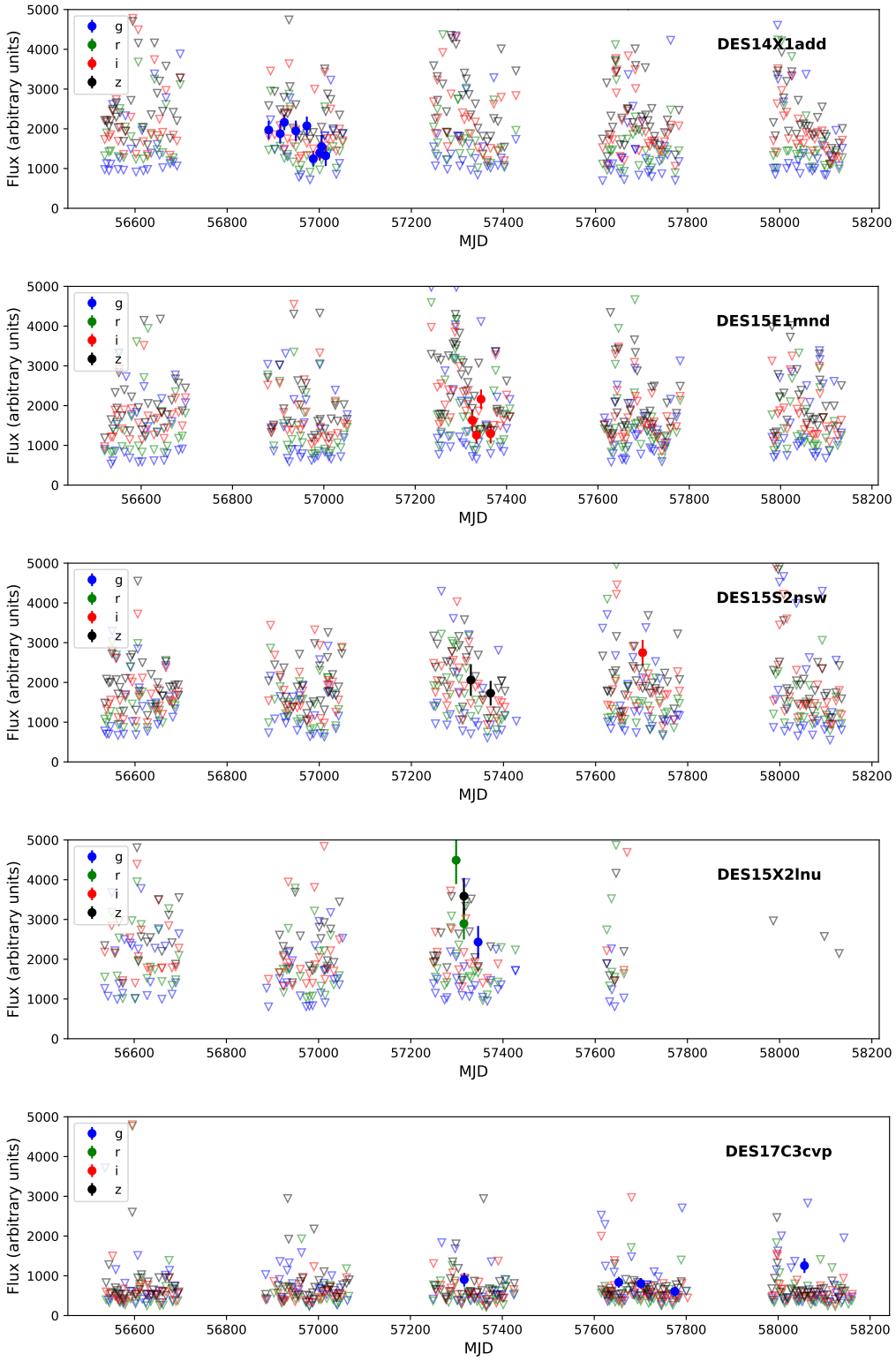

Figure 6.6: A selection of objects from the upper left of the t-SNE plot (Figure 6.5). Downward facing triangles show 5σ upper limits. These lightcurves have a small number of epochs that passed the `autoScan` test, but show little evidence for genuine astrophysical variability.

ous cluster. However, the objects lying at the edges of the t-SNE distribution are almost invariably composed of a very small number of detections, most or all of which are spurious. As these objects typically only have 2 or 3 detections, it is possible that they erroneously pass the preprocessing `autoScan` criteria of Section 6.1.

Perhaps it is to be expected that the most remote objects on the t-SNE plot are artefacts and spurious detections, as the lightcurves of these tend to be dissimilar from astrophysical objects; artefacts do not vary smoothly. In seeking another method to identify anomalous transients using this visualisation, I have chosen to investigate the nearest objects to the most anomalous transients that can be located on the figure in a straightforward way; SLSNe. I investigated the nearest objects to each of the 22 spectroscopically classified SLSNe shown on the plot (red points). While some of these objects were obvious AGN or SNe of standard types, others were of a more interesting nature, and are detailed below.

6.6 Unusual transients

DES14C1gm

The lightcurve and an example stamp of DES14C1gm are shown in Figure 6.7. This object was discovered in the t-SNE space in close proximity to the spectroscopically classified SLSN DES16C2nm, indicating similarity in the lightcurve (observations and lightcurves of spectroscopically classified SLSNe from DES are presented in Chapter 3).

However, when examining the stamp of this object a host galaxy was clearly visible in the center of the template image. As SLSNe have shown a strong preference to explode in star forming dwarf galaxies (Neill et al., 2011; Lunnan et al., 2014; Leloudas et al., 2015; Angus et al., 2016; Perley et al., 2016; Chen et al., 2017; Schulze et al., 2018) which often remained undetected in DES images, this indicated that DES14C1gm could be an AGN imposter, despite the fact that it was only detected in one season. A spectrum was

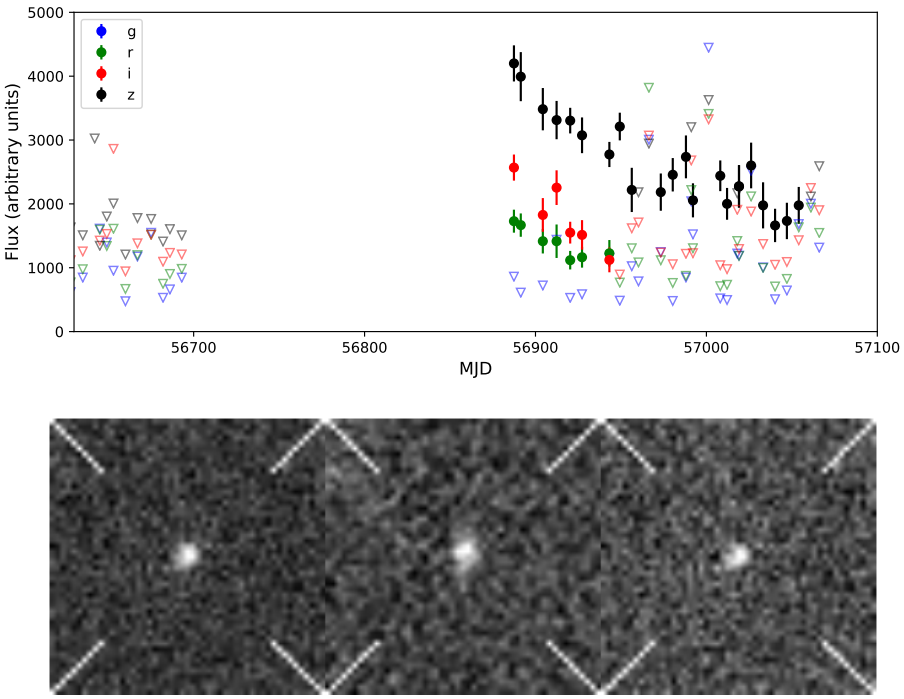

Figure 6.7: *Top:* Lightcurve of DES14C1gm. This lightcurve is similar to the high redshift SLSN DES16C2nm. *Bottom:* Example stamp for the z band epoch at 56920 (MJD). On the left is the search image, in the center is the template image, and on the right is the difference image. A host galaxy is central in the template image, indicating that this object is a likely AGN.

not taken of the host, but a photometric redshift of $z_{\rm phot} = 0.522 \pm 0.060$ was available in the DES database. This photometric redshift combined with the long duration and red colour of the lightcurve suggested that this object is not a SN. Given $z_{\rm phot}$, I estimated an absolute peak i band magnitude $M_{\rm i} = m_{\rm i} - \mu = -19.6$, which can be reached even for relatively faint AGN (Richards et al., 2006).

DES14C3plm

The lightcurve and an example stamp of DES14C3plm are shown in Figure 6.8. This object was a particularly interesting transient due to the extreme

colour evolution. It was discovered in the t-SNE space in close proximity to DES14C1rhg. It reached peak brightness in the g-band in a single DES epoch, and then declined in g. However, the three redder bands continued to rise steeply until the end of the observing season. While somewhat similar behaviour has been seen in some Type II SNe (C. Gutiérrez, private communication), in these cases the redder bands tend to plateau at g-band peak.

Inspection of the stamp of this object showed a host galaxy in the template and science images. This host galaxy is slightly off centre in the template image, indicating that DES14C3plm is unlikely to be an AGN. Indeed, in the science image the transient light can be seen as a clear off centre contribution to the total galaxy plus transient flux. A photometric redshift was available in the DES database for this galaxy, indicating that this transient may have exploded at $z_{\rm phot} = 0.168 \pm 0.088$. From $z_{\rm phot}$ I estimated an peak absolute i band magnitude $M_{\rm i} = m_{\rm i} - \mu = -17.3$, reasonable for Type Ib/c and Type II SNe. Given the evidence, DES14C3plm may have been a peculiar Type II SN.

DES15C2nfw

The lightcurve and an example stamp of DES15C2nfw are shown in Figure 6.9. This was a multi-season transient which exhibited an unusually long duration. It was discovered in the t-SNE space in proximity to the spectroscopically classified SLSN DES14C1rhg. In the observer frame, it was visible for ∼300 days. It also had interesting behaviour in the rising lightcurve, with a shoulder in an otherwise monotonic rise seen in r and i bands. It reached peak in around 50 (observer frame) days, and began to decline, at which point the observing season ended. When DES-SN restarted observations at the beginning of the fourth year, this object was still visible for multiple epochs in both z and r with one epoch in i.

The stamp of DES15C2nfw clearly shows an off centre resolved host, indicating that it was not an AGN. In the science image, the transient and

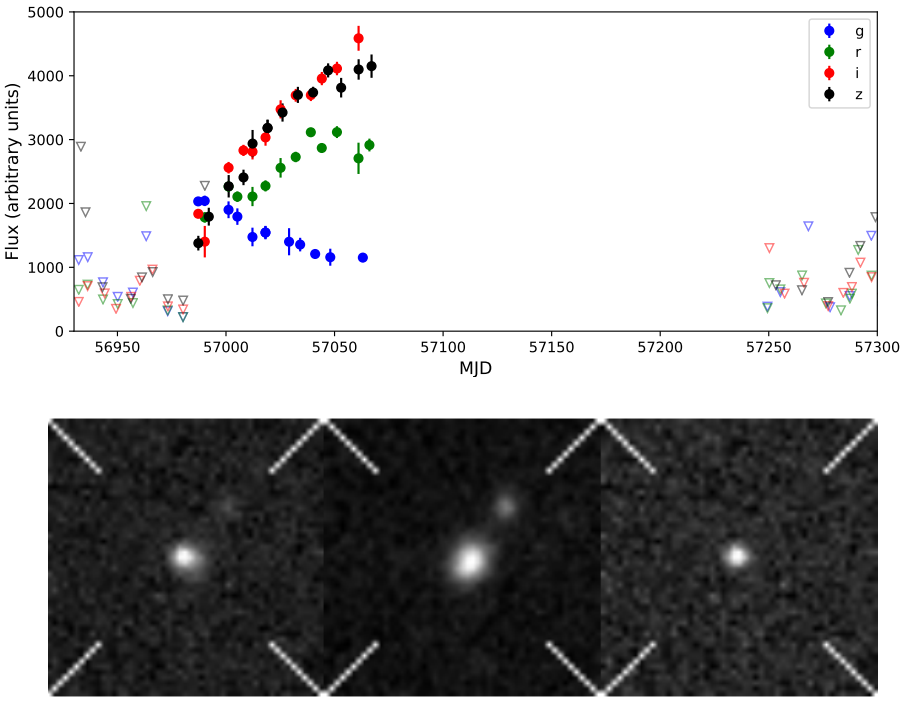

Figure 6.8: *Top:* Lightcurve of DES14C3plm, a single season transient. An anomalous degree of colour evolution is evident from the precise photometry. *Bottom:* The i band stamp for the epoch 57051 (MJD). From left to right the images are: search image, template image and difference image. A host galaxy is clearly visible in the template image, although this host is slightly off center, indicating that this object is unlikely to be an AGN.

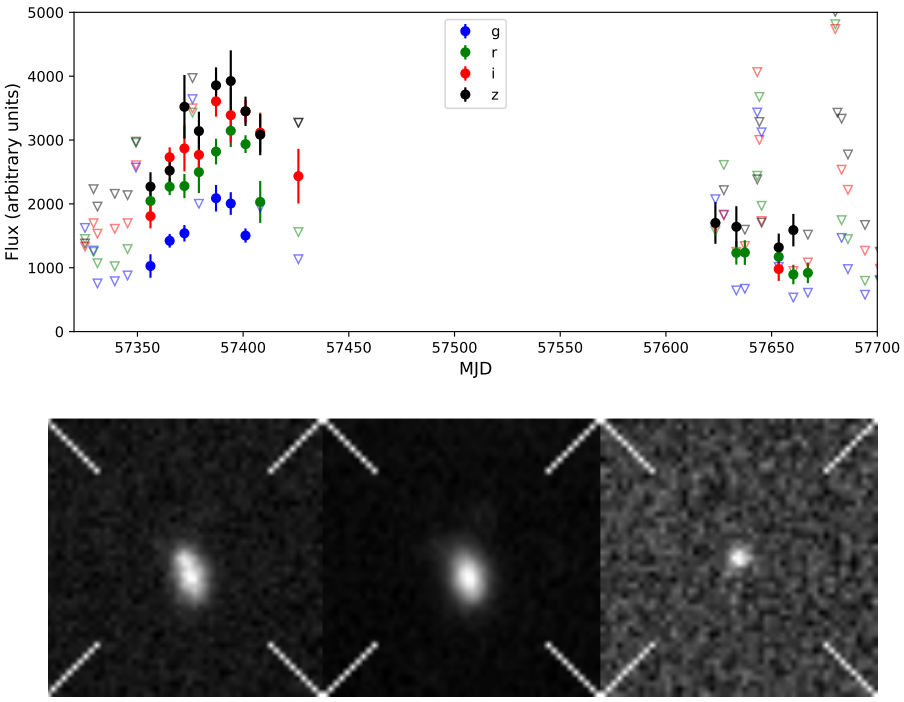

Figure 6.9: *Top:* Lightcurve of DES15C2nfw. This object exhibits an anomalous duration, lasting on the order of a year from rise to fading below the DES detection limit. *Bottom:* Example r band stamp (search, template, and difference images) for epoch 57365 (MJD). A host galaxy is clearly visible in the template image, although this host is off center. Both the SN and the galaxy light can be seen in the search image.

galaxy light can clearly be seen, with the transient in the outer part of the galaxy. The rising lightcurve of DES15C2nfw was consistent with a `pSNID` fit to a SN Ia at MJD 57376, and a spectroscopic redshift of the host galaxy was obtained as part of the OzDES program, which puts it at $z_{\rm spec} = 0.338$. I estimated a peak z band magnitude $M_{\rm z} = m - \mu = -18.9$. This object may be a Type II or Type Ib/c SN, but of abnormally long duration. Of SNe II and SNe Ib/c, SNe IIP have the longest duration of < 150 rest frame days (Arcavi, 2017). Meanwhile, DES15C2nfw had a duration of $\sim 300/1.338 = 224$ rest frame days.

DES15X3hk

The lightcurve and an example stamp of DES15X3hk are shown in Figure 6.10. This object was an unusual transient due to its long duration. It was seen declining for an entire observing season, and did not exhibit any flux in other observing seasons, except for the end of a z band tail in the subsequent season which was consistent with the main decline. Visually, the lightcurve appears similar to the high redshift SLSN DES16C2nm. It was discovered in the t-SNE space in proximity to DES14C1fi.

The stamp of DES15X3hk shows what appears to be an irregular galaxy. As this galaxy had an unusual morphology it was difficult to say whether the transient was located in the exact centre, and therefore AGN activity could not be ruled out. The DES database contained one associated host galaxy, with a spectroscopic redshift of $z_{\rm spec} = 0.357$. I estimated a peak absolute z band magnitude of $M_{\rm z} = m_{\rm z} - \mu = -19.3$. Given this peak magnitude, the spectroscopic redshift of the host, and the long duration and red colour of the lightcurve, this object was most likely to be an AGN.

DES16X3cer

The lightcurve and an example stamp of DES16X3cer are shown in Figure 6.11. This object was an excellent SLSN candidate due to both the long rise and slow decline. It was found in the t-SNE space in close proximity to the spectroscopically classified SLSN DES14X2byo. It was also highlighted by the search for SLSN candidates in Chapter 4, and was therefore in the SLSN sample used to compute the volumetric rate.

The stamp showed that there was no host galaxy detected in the template image of DES16X3cer. The host galaxy was likely fainter in apparent magnitude than the single epoch DES depth, which supported the hypothesis that this object was a true SLSN.

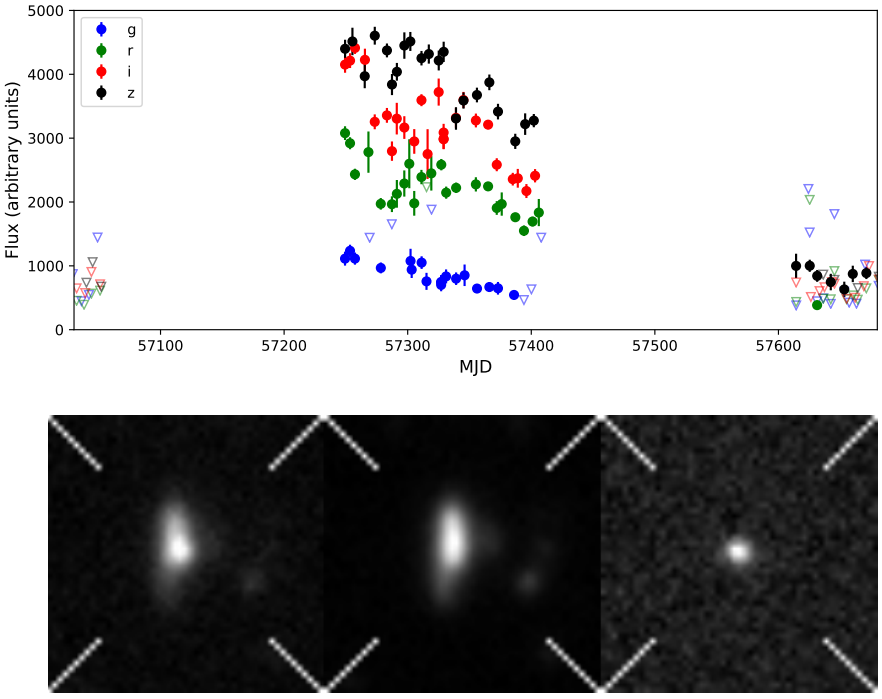

Figure 6.10: *Top:* Lightcurve of DES15X3hk. This object was an interesting transient due to the long duration and red colour of the lightcurve. *Bottom:* Example i band stamp (search, template, difference) for the epoch 57257 (MJD). A resolved host galaxy is clearly visible in the template image and search image, although the center of this irregular galaxy is difficult to locate. AGN activity cannot be ruled out.

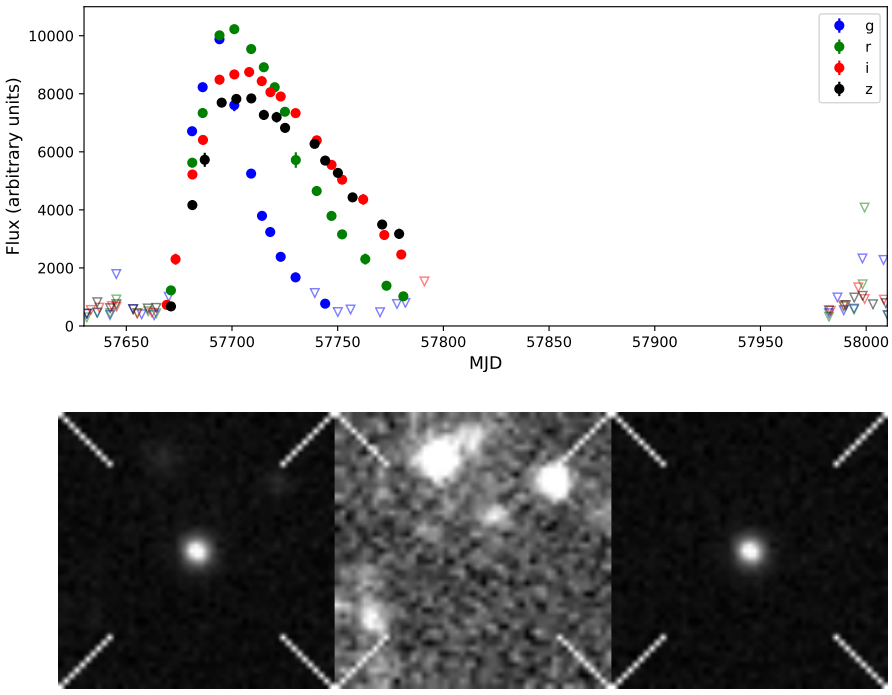

Figure 6.11: *Top:* Lightcurve of DES16X3cer. This was a strong candidate for a SLSN due to both the relatively long rise and slow decline. *Bottom:* Example r band stamp (search, template, difference) for the epoch 57709 (MJD). No host galaxy is seen in the template image, strengthening the case for this object as a SLSN. It was also discovered as a SLSN candidate by the photometric search of Chapter 4.

DES17C3efr

The lightcurve and an example stamp of DES17C3efr are shown in Figure 6.12. This object was another excellent SLSN candidate, this time discovered in the t-SNE space in close proximity to the spectroscopically classified SLSN DES14C1fi. The lightcurve of this object shows an extended rise and slow decline. It was also highlighted by the photometric search in Chapter 3 and is included in the rate sample.

The stamp for this object again shows no clear host galaxy. Therefore, it is likely to have exploded in a dim host which was too faint to be detected in the DES single epoch images, as expected for SLSNe.

6.7 Discussion and further work

Upon initial inspection of remote unclassified objects in the t-SNE visualisation it was clear that many of these were detected in a small number of epochs (often 2 or 3), and did not show clear evidence for genuine astrophysical flux variations. To remove these objects from the sample, additional criteria could be added to the preprocessing stage of the pipeline, for example, requiring objects to be detected in some minimum number of epochs. However, recently discovered classes of anomalous transients (e.g. rapidly evolving transients; Pursiainen et al. 2018) often have only a few epochs on the lightcurve (typically 3 detected to 5σ), and would likely be removed from the sample under such criteria. Nonetheless, long duration transients would remain, and this could be a promising route for future investigation.

When all five observing seasons were included in the analysis, I found that objects detected in the same DES observing season tended to group in proximity in the t-SNE visualisation space, regardless of their astrophysical class. To mitigate this problem, I have chosen to include only the single season lightcurves. However, this meant that flux information in other seasons was discarded, and therefore AGN contaminants were introduced into regions of the diagram otherwise inhabited by SNe. Further work on the

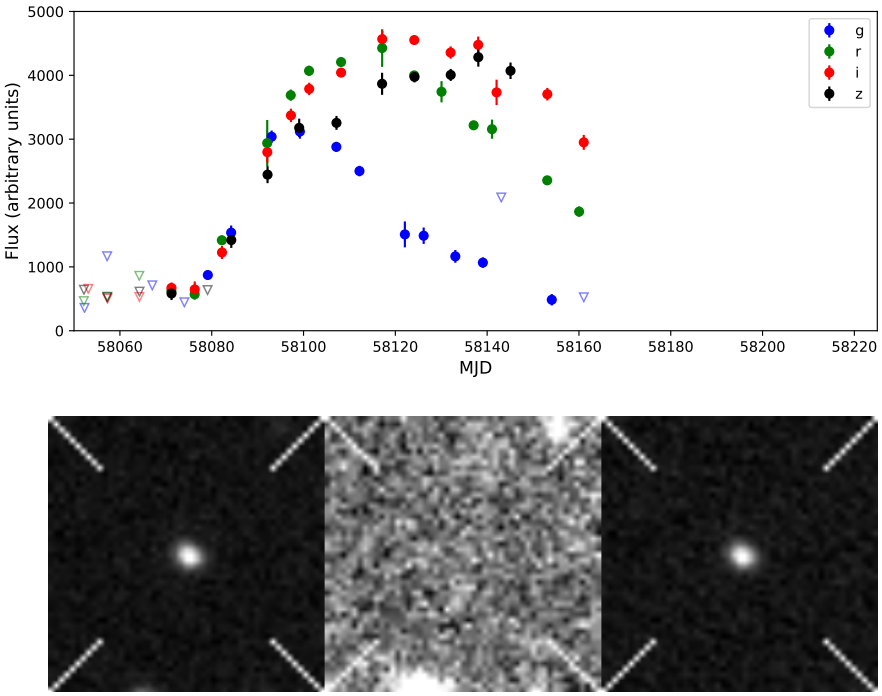

Figure 6.12: *Top:* Lightcurve of DES17C3efr. This object was a strong candidate for a SLSN due to both the relatively long rise and slow decline. *Bottom:* Example r band stamp (search, template, difference) for the epoch 58124 (MJD). No host galaxy is seen in the template image, strengthening the case for this object as a SLSN. It was also discovered as a SLSN candidate by the photometric search of Chapter 4.

unsupervised learning pipeline should include a more stringent selection of objects in the preprocessing stage to remove AGN contaminants. For example, convolutional neural networks have been shown to achieve $> 95\%$ accuracy in AGN/SN classification (M. Pursiainen, private communication). Alternatively, selection criteria similar to those described in Chapter 4 could be used to reduce AGN contamination.

Upon visual inspection of regions inhabited by spectroscopically classified objects, it appeared that the t-SNE algorithm tended to find similarities among objects based on the lightcurve coverage. This resulted in three primary regions in the t-SNE space in which rising, declining and events central to the detection season were found. To mitigate this effect one could cut from the sample all objects suffering from temporal edge effects, although this would significant reduce the sample size, due to the relatively short duration of the DES seasons (many objects suffer from temporal edge effects). Alternatively, one could extrapolate the lightcurves which have been otherwise cut by the edge of the observing seasons. This would require detailed modelling of the lightcurves, which may be challenging given the unknown spectroscopic class of the majority of the objects.

As well as anomalous transients, the unsupervised learning pipeline showed potential for the identification of thousands of SNe of standard types, including Type Ia, Type Ib/c and Type II SNe. A large number of unclassified SN candidates of standard types emerged when exploring the t-SNE parameter space. In general, the pipeline worked well for separating spurious detections and artefacts from genuine astrophysical transients, as shown in Section 6.5. However, the t-SNE method does not provide a clear way to sub-classify these objects, as there is considerable degeneracy between, for example, Type Ia and Type Ib/c lightcurves.

The unsupervised learning method will require further work to be able to identify a significant number of the anomalous transients in the DES photometric database. Given that there is necessarily some degree of information loss in the t-SNE two dimensional projection, future efforts that use

unsupervised learning for anomaly detection should identify the anomalous lightcurves in the high dimensional space resulting from the PCA analysis. Clustering methods such as k-means (Lloyd, 1982; Arthur & Vassilvitskii, 2007) or DBSCAN (Ester et al., 1996; Schubert et al., 2017) may be able to better differentiate between anomalous objects and those of standard types.

Finally, zero convincing SLSN candidates were discovered in proximity to the classified SLSNe that were not already discovered in Chapter 4. This supports the assumption that the Chapter 4 search for photometric SLSN candidates discovered the majority of such candidates in the photometrically complete effective volume-time used for the rate computation.

6.8 Conclusion

This chapter demonstrates the use of machine learning, particularly the t-SNE visualisation algorithm, in exploring the DES dataset of $28,184$ objects. I discussed the data preprocessing, and used scores from the machine learning algorithm `autoScan` (Goldstein et al., 2015) to remove $7,596$ spurious objects. I detailed the interpolation of the DES transient lightcurves using Gaussian processes, and thereby interpolated the photometry of all objects to lie on a uniform grid. I performed a stationary wavelet transform on the remaining objects to mitigate the effect of translation variance of the lightcurves. I followed this with a principal component analysis to vastly reduce the dimensionality of the wavelets and reduce the computational time of the t-SNE algorithm. I used the t-SNE algorithm to visualise these principal components in a two dimensional abstract parameter space in which object similarities emerged. I discussed some of the anomalous and interesting transients that were discovered in proximity to the classified SLSNe. Finally, I discussed the pitfalls and further steps needed to ensure the success of unsupervised machine learning pipelines in identifying anomalous transients in the DES-SN catalogue.

Chapter 7

Summary and future perspectives

Section 7.1 is a summary of my own work. Section 7.2 is an an outlook to the future of scientific projects relevant to this thesis; references are given throughout.

This thesis has described the definitive measurement of the volumetric rate of SLSNe-I. By fitting a modified black body model to the spectroscopic sample of SLSNe-I from DES-SN, I have simulated synthetic lightcurves to determine the photometric detection efficiency across the DES-SN observed cosmological volume and observing time. I have searched for and recovered the SLSN candidates that were not spectroscopically classified, and by combining these with the spectroscopic sample I have measured the volumetric rate of SLSNe in the redshift range $0.21 < z < 0.99$. I have also implemented a machine learning pipeline to discover peculiar transients in the DES-SN database. In this chapter, I summarise the results and implications of my work. Finally, I discuss upcoming samples of SLSNe, and how they can be used to solve outstanding problems in our understanding of SLSNe.

7.1 Summary

7.1.1 Modelling spectroscopic SLSNe and simulations

In Chapter 3 I detailed the model used to fit the spectroscopic SLSN sample from DES-SN. This model assumed a linearly expanding and cooling photosphere combined with an absorption template to account for the effects of ejecta metals on the UV part of the SED. I showed that the model adequately represented the detectability of the lightcurves for the spectroscopically classified SLSNe in DES which passed the following criteria: (1) the peak brightness must lie within the DES observing window in at least 2 bands; (2) the peak i band absolute magnitude must be brighter than $M_{\rm i} \leq -19.8$.

Using these model fits to the DES-SN spectroscopic SLSNe, I simulated $> 10^6$ lightcurves across the DES-SN survey volume and observing time. I defined the 'detection' of a lightcurve as the following: (1) at least 5 epochs detected in each of 3 filters to 5σ; (2) at least one epoch before maximum light in 2 filters; (3) at least one epoch after maximum light in 2 filters. By computing the fraction of lightcurves detected in each redshift and explosion date bin, I was able to characterise the photometrically complete regions of the DES-SN search for SLSNe.

The results of these efficiency simulations showed that bright members of the spectroscopic SLSNe sample are detectable to higher redshift than faint members, as expected. I found that the DES-SN search for SLSNe is photometrically complete out to $z \sim 0.8$ in the shallow fields, and $z \sim 1.0$ in the deep fields. Prajs et al. (2017) used a similar technique to estimate the completeness of the SNLS survey for SLSNe, and found that SNLS was complete out to $z \sim 1.3$. The faintest object in their sample had absolute peak magnitude $M_{\rm u} = -20.9$, while I used a cut off of $M_{\rm i} = -19.8$, and a smaller photometrically complete region is expected in my simulations.

These simulations were a crucial part of my rate measurement. By defining the effective volume-time as the regions over which the DES-SN search

for SLSNe was photometrically complete, I was able to set the photometric efficiency $\epsilon_{\rm phot} = 1$ in Equation 5.1. This effective volume-time constituted both the cosmological volume, and the observer frame time in which the count of SLSNe was used to compute the volumetric rate.

7.1.2 The search for photometric SLSN candidates

In Chapter 4, I performed a search into the DES-SN database of transients to identify promising photometric SLSN candidates. I enforced a succession of selection criteria using both lightcurve and host galaxy information, and reduced the raw sample to 229 objects (0.7% of the raw dataset). I then led a visual inspection effort to further reduce the sample. This resulted in a sample of 52 objects including 14 spectroscopically classified SLSNe, 8 contaminants, and 30 photometric SLSN candidates. I assumed that this search had found all photometric SLSNe in the effective volume-time defined in Chapter 3. This allowed me to set the spectroscopic efficiency, $\epsilon_{\rm spec} = 1$, in Equation 5.1.

As a result of my search for photometric SLSN candidates, two especially interesting transients were identified. The first of these, DES16C3eco, had a duration of > 1 year, and was still detected above 5σ when DES-SN concluded its observations. A Gemini spectrum of this object was reduced by M. Smith (University of Southampton), and a tentative classification of a SN II at $z = 0.12$ was made based on a suspected broad Hα feature at 7320Å. There is also a possibility that this object may have been an AGN based on a small number of objects in the DES-SN catalogue that exhibited similar lightcurve behaviour. In either case, the lightcurve behaviour was peculiar.

Second, my search also discovered DES17X1blv in the dataset. This was a good SLSN candidate, whose Gemini spectrum was retrieved from an archive and subsequently reduced by M. Smith and C. Angus (University of Southampton), resulting in a classification of SLSN-I at $z = 0.69$. This object was presented with the DES SLSN sample in Angus et al. (2019).

The result of my search is the largest sample of SLSNe that has yet

been compiled. This sample can be used for further population studies. For example, Angus et al. (2019) have found that the lightcurves of 8 of the 22 spectroscopically classified SLSNe cannot be adequately reproduced by the magnetar model. Additional magnetar fits to the photometric candidates that I have identified could further constrain the fraction of the total SLSNe from DES that can be fit by this model. This fraction could inform us as to whether the magnetar model is the correct explosion mechanism for SLSN lightcurves, or whether an additional energy source is needed.

7.1.3 The volumetric rate of SLSNe from DES

In Chapter 5 I brought together the results of Chapters 3 and 4 to compute the volumetric rate of SLSNe from DES. To achieve this, I carried out a Monte Carlo simulation to account for the uncertainty in the redshift of 17 hostless candidates in my photometric sample. This allowed me build up the distribution of possible rates shown in Figure 5.4. I fit a lognormal PDF to this distribution, and from the mean and 68% confidence interval of this PDF I derived the volumetric rate and its systematic uncertainty,

$$R_{\rm V} = 190\,^{+26}_{-23}\,({\rm sys}) \pm 52\,({\rm stat})\,{\rm SLSNe\,yr^{-1}\,Gpc^{-3}}, \tag{7.1}$$

at a volume weighted mean redshift of $\overline{z} = 0.797$.

This measurement was largely consistent with previous measurements at a similar redshift. I fit a normalised cosmic SFH to the measurements both with and without my measurement. The normalisation constant is increased by $1.4\,\sigma$ with my measurement included, and there was no compelling evidence to indicate that a different fraction of massive stars explode as SLSNe than what had previously been estimated, although further rate measurements at a similar redshift are needed to test this. For example, the sample of 17 SLSNe-I (Lunnan et al., 2018) from the Pan-STARRS MDS survey are in the redshift range $0.3 < z < 1.6$, and could provide an independent measurement of the volumetric rate.

7.1.4 Machine learning with the DES-SN catalogue

In Chapter 6, I applied an unsupervised machine learning pipeline to the Gaussian processed catalogue of DES-SN transients. This involved preprocessing, stationary wavelet decomposition, principal component analysis, and finally a t-SNE visualisation. It became apparent that the t-SNE visualisation method used was particularly sensitive to the temporal edges of the 6 month DES observing window that cut many of the transient lightcurves before or after the peak. Future machine learning pipelines using the DES-SN data would either need to account for these temporal edge effects, or otherwise reject objects suffering from temporal edge effects from the sample.

Nonetheless, I was able to present six interesting candidates which were uncovered by this pipeline. Two of these were rediscoveries of SLSN candidates from my photometric search in Chapter 4. There were zero SLSN candidates found by the machine learning pipeline which were not found by the photometric search of Chapter 4, in support of the assumption that the photometric search found the majority of the SLSN candidates which exploded in the effective volume-time of the rate calculation (i.e. that $\epsilon_{\rm spec} = 1$).

For the remaining four candidates, I estimated peak absolute magnitudes based on host galaxy spectroscopic or photometric redshifts. By considering the lightcurve, absolute peak magnitude, and location of these objects within the host galaxy, I suggested that two of these were likely peculiar Type Ib/c or Type II SNe and two were likely a result of AGN variability.

This chapter demonstrated the need to account for temporal edge effects when using machine learning methods for studies of observed SN lightcurves. The lessons learned in this chapter will be invaluable to future SN analyses that use machine learning especially in the DES-SN transient dataset, but also in any transient survey that uses a seasonal observing strategy.

7.2 Future perspectives

The primary work of this thesis was the measurement of the volumetric rate of SLSNe-I at $0.21 < z < 0.99$. Upcoming samples of SLSNe-I will be larger, increasing the precision of volumetric rate measurements, and facilitating statistical studies of other aspects of the nature and applications of SLSNe.

The Zwicky Transient Facility (ZTF; Bellm, 2014) began observations in 2018, and is repeatedly scanning the entire northern sky in 2 filters every 3 nights down to an apparent magnitude of $m_{\rm R} \sim 20.5$ (Graham et al., 2019). ZTF produces on order a million alerts each night, and identifying promising SLSN candidates in the data is challenging. However, the photometric criteria I developed in Chapter 4 were defined in such a way that they can be applied to any transient survey with only minor modifications. Applying these criteria to the ever-growing catalogue of objects from ZTF will provide many promising SLSN candidates. These candidates will be observationally bright due to both their nearby location in the local Universe, and their intrinsically bright peak magnitudes. Therefore, they are excellent candidates for nebular spectroscopy; when the ejecta have become optically thin, spectroscopic observations can probe into the inner layers of the SN explosion. Nicholl et al. (2019) analysed nebular spectra of 12 SLSNe, and found similar late time spectral evolution to SNe Ic, in support of the idea that SLSNe and SNe Ic may form a continuous distribution.

In addition, if SLSN candidates can be identified in the ZTF alert stream that are very nearby ($\lesssim$ 30 Mpc; Smartt 2009), searches for the progenitor stars themselves can be carried out. Traditional methods of progenitor searches have been successful in identifying the parent stars of Type II SNe (e.g. Van Dyk et al., 2003) by precisely identifying the location of the SN explosion in legacy HST images that were taken before the SN exploded. ZTF is well suited to these studies due to its large search area, alleviating the rarity of SLSNe at low redshift. If SLSN progenitors are successfully identified it would constitute the first such detection, and would inform us as to whether these transients are the result of the explosion of very high mass

stars, as expected (Gal-Yam, 2018).

ZTF produces 10% of the alerts expected from the Large Synoptic Survey Telescope (LSST; LSST Science Collaboration et al. 2009; Ivezić et al. 2019), which is scheduled to see first light in 2022. Scovacricchi et al. (2016) predicted that the LSST wide-field survey will find 10,000 SLSN candidates up to a redshift of $z \lesssim 2$ (assuming a lightcurve quality of at least 5 epochs in 2 filters). Similar to the ZTF catalogue, the criteria I have developed in Chapter 4 can be used to select SLSNe from the LSST transient catalogue that will be polluted by subtraction artefacts, AGN and standard SN types. The sample of 10,000 SLSNe from the LSST wide-field survey will allow the computation of the volumetric rate at low and intermediate redshifts to orders of magnitude better precision than has yet been achieved. Volumetric rate measurements with LSST could be separated into different redshift bins, and the rate as a function of redshift can be measured with a single homogeneously selected sample of SLSNe for the first time. This will allow an independent measurement of the shape of the cosmic SFH history at $z < 2$ (Scovacricchi et al., 2016), and thereby inform models of the star formation history of the Universe.

The Euclid Deep Survey (EDS) is predicted to discover 210 SLSNe at high redshift ($z < 3.5$, Inserra et al. 2018b), which will permit a precise measurement of the volumetric rate of SLSNe at $z > 2$, providing that challenges in determining the sample contamination and detection efficiencies can be overcome. If so, such a measurement may inform the redshift of the turnover of the cosmic SFH independently from other methods that study galaxy populations (Madau & Dickinson 2014 give a detailed review).

Another exciting prospect for the application of SLSNe is their use as cosmological distance indicators. The preliminary work of Inserra & Smartt (2014) found correlations between the peak magnitude and the brightness decline rate at 30 rest frame days after peak, suggesting that SLSNe-I may be standardised in an analogous manner to Type Ia SNe. If so, an observed distance modulus-redshift relation for SLSNe-I, $\mu_{\rm obs}$, can be obtained. The

distance modulus-redshift relation predicted by a cosmological model, $\mu_{\rm model}$, can then be fit to $\mu_{\rm obs}$ by varying the cosmological parameters, and these parameters can thereby be constrained.

Scovacricchi et al. (2016) combined their LSST wide-field sample of SLSNe-I, SNe Ia from DES, and Planck CMB measurements, to predict constraints of 2%, 5% and 0.14 on $\Omega_{\rm M}$, w_0 and $w_{\rm a}$ respectively. Meanwhile, work using observed SLSNe-I to produce the first Hubble diagram along with its cosmological constraints is ongoing (Inserra et al., subm). Preliminary results indicate that SLSNe-I will hold an important position in future cosmological measurements, especially as they can be observed to much higher redshift than SNe Ia due to their blue colour and intrinsic brightness.

7.2.1 Concluding remarks

Significant progress has been made in understanding the origin and applications of SLSNe-I since their discovery and classification (Quimby et al., 2011). However, much remains to be learned. For example, despite amassing evidence pointing towards the magnetar model as the most convincing model to power SLSN-I lightcurves (e.g. Inserra et al. 2013; Nicholl et al. 2013, 2017b), this model cannot reproduce a significant fraction of these (De Cia et al. 2018; Angus et al. 2019), which may indicate that multiple energy sources are necessary (e.g. interaction between the ejecta and H-poor circumstellar material, Chatzopoulos et al. 2013). Similarly, it remains unclear as to whether SLSNe form a continuous distribution in brightness with the fainter SNe Ic-BL and SNe Ic (De Cia et al., 2018). The precise and deep photometry of DES-SN has contributed to this latter mystery by detecting fainter SLSNe than previously (Angus et al., 2019). Upcoming surveys such as LSST will continue this effort, and perhaps form a unified understanding of SLSNe and their fainter counterparts.

Bibliography

Abazajian K. N., et al., 2009, ApJS, 182, 543

Abbott B. P., et al., 2017, Nature, 551, 85

Abbott T. M. C., et al., 2018a, Phys.Rev.D, 98, 043526

Abbott T. M. C., et al., 2018b, ApJS, 239, 18

Abbott T. M. C., et al., 2019, ApJ, 872, L30

Adelman-McCarthy J. K., et al. 2007, VizieR Online Data Catalog, 2276

Alam S., et al., 2017, MNRAS, 470, 2617

Anderson J. P., et al., 2014, ApJ, 786, 67

Angel J. R. P., Hilliard R. L., Weymann R. J., 1979, in The MMT and the Future of Ground-Based Astronomy. p. 87

Angus C. R., Levan A. J., Perley D. A., Tanvir N. R., Lyman J. D., Stanway E. R., Fruchter A. S., 2016, MNRAS, 458, 84

Angus C. R., et al., 2019, MNRAS, 487, 2215

Antilogus P., Astier P., Doherty P., Guyonnet A., Regnault N., 2014, Journal of Instrumentation, 9, C03048

Arcavi I., 2017, Hydrogen-Rich Core-Collapse Supernovae. p. 239, doi:10.1007/978-3-319-21846-5˙39

Arthur D., Vassilvitskii S., 2007, in Proceedings of the eighteenth annual ACM-SIAM symposium on Discrete algorithms. pp 1027–1035

Baade W., Zwicky F., 1934a, Proceedings of the National Academy of Science, 20, 254

Baade W., Zwicky F., 1934b, Proceedings of the National Academy of Science, 20, 259

Barbon R., Ciatti F., Rosino L., 1979, A&A, 72, 287

Barchi P. H., de Carvalho R. R., Rosa R. R., Sautter R., Soares-Santos M., Marques B. A. D., Clua E., 2019, arXiv e-prints, p. arXiv:1901.07047

Becker A., 2015, HOTPANTS: High Order Transform of PSF ANd Template Subtraction, Astrophysics Source Code Library (ascl:1504.004)

Bellm E., 2014, arXiv e-prints, pp 27–33

Bernstein J. P., et al., 2012, ApJ, 753, 152

Bertin E., 2010, SWarp: Resampling and Co-adding FITS Images Together, Astrophysics Source Code Library (ascl:1010.068)

Bertin E., 2011, in Evans I. N., Accomazzi A., Mink D. J., Rots A. H., eds, Astronomical Society of the Pacific Conference Series Vol. 442, Astronomical Data Analysis Software and Systems XX. p. 435

Bertin E., Arnouts S., 1996, A&AS, 117, 393

Bethe H. A., Wilson J. R., 1985, ApJ, 295, 14

Betoule M., et al., 2014, A&A, 568, A22

Bhirombhakdi K., Chornock R., Margutti R., Nicholl M., Metzger B. D., Berger E., Margalit B., Milisavljevic D., 2018, ApJ, 868, L32

Bigelow B. C., Dressler A. M., Shectman S. A., Epps H. W., 1998, in D'Odorico S., ed., Society of Photo-Optical Instrumentation Engineers (SPIE) Conference Series Vol. 3355, Optical Astronomical Instrumentation. pp 225–231, doi:10.1117/12.316760

Bonvin V., et al., 2017, MNRAS, 465, 4914

Bothwell M. S., et al., 2011, MNRAS, 415, 1815

Branch D., Wheeler J. C., 2017, Supernova Explosions. Springer-Verlag

Brenner N., Bialek W., de Ruyter van Steveninck R., 2000, Neuron, 26, 695

Cardelli J. A., Clayton G. C., Mathis J. S., 1989, ApJ, 345, 245

Carrasco Kind M., Drlica-Wagner A., Koziol A. M. G., Petravick D., 2018, preprint, (`arXiv:1810.02721`)

Carrasco Kind M., Drlica-Wagner A., Koziol A., Petravick D., 2019, The Journal of Open Source Software, 4, 1022

Carter P., Beutler F., Percival W. J., Blake C., Koda J., Ross A. J., 2018, MNRAS, 481, 2371

Cepa J., et al., 2003,] 10.1117/12.460913, 4841, 1739

Chandrasekhar S., 1931, ApJ, 74, 81

Chandrasekhar S., 1984, Science, 226, 497

Chatzopoulos E., Wheeler J. C., 2012, ApJ, 760, 154

Chatzopoulos E., Wheeler J. C., Vinko J., 2012, ApJ, 746, 121

Chatzopoulos E., Wheeler J. C., Vinko J., Horvath Z. L., Nagy A., 2013, ApJ, 773, 76

Chen T.-W., et al., 2017, ApJ, 849, L4

Chevalier R. A., Fransson C., 2003, Supernova Interaction with a Circumstellar Medium. pp 171–194, doi:10.1007/3-540-45863-8˙10

Childress M. J., et al., 2017, MNRAS, 472, 273

Clark D. H., Stephenson F. R., 1982, in Rees M. J., Stoneham R. J., eds, NATO Advanced Science Institutes (ASI) Series C Vol. 90, NATO Advanced Science Institutes (ASI) Series C. pp 355–370

Cole S., et al., 2001, MNRAS, 326, 255

Cooke J., et al., 2012, Nature, 491, 228

Couch S. M., 2017, Philosophical Transactions of the Royal Society of London Series A, 375, 20160271

D'Andrea C. B., et al., 2018, arXiv e-prints, p. arXiv:1811.09565

DES Collaboration 2005, arXiv e-prints, pp astro–ph/0510346

DES Collaboration et al., 2017, arXiv e-prints, p. arXiv:1712.06209

DES Collaboration et al., 2018a, arXiv e-prints, p. arXiv:1810.02499

DES Collaboration et al., 2018b, arXiv e-prints, p. arXiv:1811.02375

DES Collaboration et al., 2019, ApJ, 872, L30

Dahlen T., Strolger L.-G., Riess A. G., Mattila S., Kankare E., Mobasher B., 2012, ApJ, 757, 70

Daubechies I., Bates B. J., 1993, Acoustical Society of America Journal, 93, 1671

De Cia A., et al., 2018, ApJ, 860, 100

Desai S., et al., 2012, ApJ, 757, 83

Dexter J., Kasen D., 2013, ApJ, 772, 30

Dilday B., et al., 2010, ApJ, 713, 1026

Ester M., Kriegel H.-P., Sander J., Xu X., et al., 1996, in Kdd. pp 226–231

Estrada J., et al., 2010. p. 77351R, doi:10.1117/12.857651

Faber S. M., et al., 2003, SPIE, 4841, 1657

Filippenko A. V., 1988, AJ, 96, 1941

Firth R. E., et al., 2015, MNRAS, 446, 3895

Fischer J., 2015, PhD thesis, University of Pennsylvania

Fitzpatrick M., 2010, in Mizumoto Y., Morita K.-I., Ohishi M., eds, Astronomical Society of the Pacific Conference Series Vol. 434, Astronomical Data Analysis Software and Systems XIX. p. 260

Flaugher B., et al., 2015, AJ, 150, 150

Frohmaier C., et al., 2019, MNRAS, 486, 2308

Gal-Yam A., 2012, Science, 337, 927

Gal-Yam A., 2018, arXiv e-prints, p. arXiv:1812.01428

Ghorbani M., Chong E. K., 2018, arXiv preprint arXiv:1803.05075

Goldstein D. A., et al., 2015, AJ, 150, 82

Graham M. J., et al., 2019, PASP, 131, 078001

Green J. C., et al., 2012, ApJ, 744, 60

Gröchenig K., 2013, Foundations of time-frequency analysis. Springer Science & Business Media

Gruppioni C., et al., 1999, MNRAS, 305, 297

Gschwend J., et al., 2018, Astronomy and Computing, 25, 58

Gupta R. R., et al., 2016, AJ, 152, 154

Guy J., Astier P., Nobili S., Regnault N., Pain R., 2005, A&A, 443, 781

Guy J., et al., 2007, A&A, 466, 11

Hamuy M., Pinto P. A., 2002, ApJ, 566, L63

Hartley P., Flamary R., Jackson N., Tagore A. S., Metcalf R. B., 2017, MNRAS, 471, 3378

Heger A., Jeannin L., Langer N., Baraffe I., 1997, A&A, 327, 224

Hicken M., et al., 2017, ApJS, 233, 6

Hillebrandt W., Niemeyer J. C., 2000, ARA&A, 38, 191

Hogg D. W., Baldry I. K., Blanton M. R., Eisenstein D. J., 2002, arXiv e-prints, pp astro–ph/0210394

Holoien T. W.-S., et al., 2016, Acta Astronomica, 66, 219

Holschneider M., Kronland-Martinet R., Morlet J., Tchamitchian P., 1989, in Combes J.-M., Grossmann A., Tchamitchian P., eds, Wavelets. Time-Frequency Methods and Phase Space. p. 286

Hook I. M., Jørgensen I., Allington-Smith J. R., Davies R. L., Metcalfe N., Murowinski R. G., Crampton D., 2004, PASP, 116, 425

Hopkins A. M., Beacom J. F., 2006, ApJ, 651, 142

Hotelling H., 1933, Journal of educational psychology, 24, 417

Howell D. A., et al., 2013, ApJ, 779, 98

Hubble E., 1936, ApJ, 84, 517

Iben I. J., Tutukov A. V., 1984, ApJ, 284, 719

Inserra C., Smartt S. J., 2014, ApJ, 796, 87

Inserra C., et al., 2013, ApJ, 770, 128

Inserra C., et al., 2018a, MNRAS, 475, 1046

Inserra C., et al., 2018b, A&A, 609, A83

Inserra C., et al., subm, Nature Astronomy

Ivezić Ž., et al., 2019, ApJ, 873, 111

Janka H.-T., 2012, Annual Review of Nuclear and Particle Science, 62, 407

Jansen F., et al., 2001, A&A, 365, L1

Jarvis M. J., et al., 2013, MNRAS, 428, 1281

Kaiser N., et al., 2010, in Ground-based and Airborne Telescopes III. p. 77330E, doi:10.1117/12.859188

Kasen D., Bildsten L., 2010, ApJ, 717, 245

Kasen D., Metzger B. D., Bildsten L., 2016, ApJ, 821, 36

Kaspi V. M., Beloborodov A. M., 2017, ARA&A, 55, 261

Kessler R., Conley A., Jha S., Kuhlmann S., 2010, arXiv e-prints, p. arXiv:1001.5210

Kessler R., et al., 2015, AJ, 150, 172

Kessler R., et al., 2019, MNRAS, 485, 1171

Komossa S., Bade N., 1999, in Poutanen J., Svensson R., eds, Astronomical Society of the Pacific Conference Series Vol. 161, High Energy Processes in Accreting Black Holes. p. 234 (`arXiv:astro-ph/9901008`)

Kullback S., Leibler R. A., 1951, The annals of mathematical statistics, 22, 79

LSST Science Collaboration et al., 2009, arXiv e-prints, p. arXiv:0912.0201

Law N. M., et al., 2009, PASP, 121, 1395

Lee G., Gommers R., Wasilewski F., Wohlfahrt K., O'Leary A., Nahrstaedt H., Contributors 2006, `https://github.com/PyWavelets/pywt`

Leloudas G., et al., 2015, MNRAS, 449, 917

Li W., Chornock R., Leaman J., Filippenko A. V., Poznanski D., Wang X., Ganeshalingam M., Mannucci F., 2011, MNRAS, 412, 1473

Lieb E. H., Yau H.-T., 1987, ApJ, 323, 140

Lloyd S., 1982, IEEE transactions on information theory, 28, 129

Lochner M., McEwen J. D., Peiris H. V., Lahav O., Winter M. K., 2016, ApJS, 225, 31

Lonsdale C. J., et al., 2003, PASP, 115, 897

Lunnan R., et al., 2014, ApJ, 787, 138

Lunnan R., et al., 2018, ApJ, 852, 81

Ly C., Malkan M. A., Hayashi M., Motohara K., Kashikawa N., Shimasaku K., Nagao T., Grady C., 2011, ApJ, 735, 91

Lyman J. D., Bersier D., James P. A., Mazzali P. A., Eldridge J. J., Fraser M., Pian E., 2016, MNRAS, 457, 328

Maaten L. v. d., Hinton G., 2008, Journal of machine learning research, 9, 2579

Madau P., Dickinson M., 2014, ARA&A, 52, 415

Mahabal A., et al., 2019, PASP, 131, 038002

Mallat S., 2008, A Wavelet Tour of Signal Processing, Third Edition: The Sparse Way, 3rd edn. Academic Press, Inc., Orlando, FL, USA

Masci F. J., et al., 2017, PASP, 129, 014002

Mazzali P. A., Sullivan M., Pian E., Greiner J., Kann D. A., 2016, MNRAS, 458, 3455

McCrum M., et al., 2015, MNRAS, 448, 1206

McGurk R. C., Kimball A. E., Ivezić Ž., 2010, AJ, 139, 1261

Miknaitis G., et al., 2007, ApJ, 666, 674

Minkowski R., 1941, PASP, 53, 224

Mohr J. J., et al., 2008, in Observatory Operations: Strategies, Processes, and Systems II. p. 70160L (arXiv:0807.2515), doi:10.1117/12.789550

Mohr J. J., et al., 2012, in Software and Cyberinfrastructure for Astronomy II. p. 84510D (arXiv:1207.3189), doi:10.1117/12.926785

Möller A., de Boissière T., 2019, arXiv e-prints, p. arXiv:1901.06384

Monet D. G., et al., 2003, AJ, 125, 984

Morganson E., et al., 2018, PASP, 130, 074501

Morice-Atkinson X., Hoyle B., Bacon D., 2018, MNRAS, 481, 4194

Moriya T. J., Liu Z.-W., Mackey J., Chen T.-W., Langer N., 2015, A&A, 584, L5

Moriya T. J., et al., 2019, ApJS, 241, 16

Muthukrishna D., Narayan G., Mandel K. S., Biswas R., Hložek R., 2019, arXiv e-prints, p. arXiv:1904.00014

Nadyozhin D. K., 1994, ApJS, 92, 527

Narayan G., et al., 2018, ApJS, 236, 9

Neill J. D., et al., 2011, ApJ, 727, 15

Neilsen E., Annis J., 2014, in Manset N., Forshay P., eds, Astronomical Society of the Pacific Conference Series Vol. 485, Astronomical Data Analysis Software and Systems XXIII. p. 77

Nicholl M., Smartt S. J., 2016, MNRAS, 457, L79

Nicholl M., et al., 2013, Nature, 502, 346

Nicholl M., et al., 2015, MNRAS, 452, 3869

Nicholl M., Berger E., Margutti R., Blanchard P. K., Guillochon J., Leja J., Chornock R., 2017a, ApJ, 845, L8

Nicholl M., Guillochon J., Berger E., 2017b, ApJ, 850, 55

Nicholl M., Berger E., Blanchard P. K., Gomez S., Chornock R., 2019, ApJ, 871, 102

Oke J. B., Gunn J. E., 1982, PASP, 94, 586

Oke J. B., et al., 1995, PASP, 107, 375

Padovani P., et al., 2017, A&A Rev., 25, 2

Pakmor R., Kromer M., Taubenberger S., Springel V., 2013, ApJ, 770, L8

Pan Y. C., et al., 2017, MNRAS, 470, 4241

Papadopoulos A., 2016, PhD thesis, University of Portsmouth

Papadopoulos A., et al., 2015, MNRAS, 449, 1215

Pascale E., et al., 2009, ApJ, 707, 1740

Pastorello A., et al., 2007, Nature, 447, 829

Pearson K., 1901, The London, Edinburgh, and Dublin Philosophical Magazine and Journal of Science, 2, 559

Perley D. A., et al., 2016, ApJ, 830, 13

Perlmutter S., et al., 1999, ApJ, 517, 565

Perrett K., et al., 2010, AJ, 140, 518

Perrett K., et al., 2012, AJ, 144, 59

Pierre M., et al., 2004, Journal of Cosmology and Astro-Particle Physics, 2004, 011

Piro A. L., 2015, ApJ, 808, L51

Planck M., 1900, Verhandl. Dtsch. Phys. Ges., 2, 237

Planck Collaboration et al., 2016, A&A, 594, A13

Planck Collaboration et al., 2018, arXiv e-prints, p. arXiv:1807.06209

Porter A. C., Filippenko A. V., 1987, AJ, 93, 1372

Prajs S., et al., 2017, MNRAS, 464, 3568

Puls J., Vink J. S., Najarro F., 2008, A&A Rev., 16, 209

Pursiainen M., et al., 2018, MNRAS, 481, 894

Quimby R. M., 2006, PhD thesis, The University of Texas at Austin

Quimby R. M., Aldering G., Wheeler J. C., Höflich P., Akerlof C. W., Rykoff E. S., 2007, ApJ, 668, L99

Quimby R. M., et al., 2011, Nature, 474, 487

Quimby R. M., Yuan F., Akerlof C., Wheeler J. C., 2013, MNRAS, 431, 912

Quimby R. M., et al., 2018, ApJ, 855, 2

Rau A., et al., 2009, PASP, 121, 1334

Rest A., et al., 2014, ApJ, 795, 44

Richards G. T., et al., 2006, AJ, 131, 2766

Röpke F. K., et al., 2012, ApJ, 750, L19

Rujopakarn W., et al., 2010, ApJ, 718, 1171

Sako M., et al., 2008, AJ, 135, 348

Sako M., et al., 2011, ApJ, 738, 162

Sako M., et al., 2018, PASP, 130, 064002

Sánchez C., et al., 2014, MNRAS, 445, 1482

Saunders W., et al., 2004, in Moorwood A. F. M., Iye M., eds, Society of Photo-Optical Instrumentation Engineers (SPIE) Conference Series Vol. 5492, Ground-based Instrumentation for Astronomy. pp 389–400, doi:10.1117/12.550871

Schanche N., et al., 2019, MNRAS, 483, 5534

Schlafly E. F., Finkbeiner D. P., 2011, ApJ, 737, 103

Schlegel E. M., 1990, MNRAS, 244, 269

Schlegel D. J., Finkbeiner D. P., Davis M., 1998, ApJ, 500, 525

Schmidt B. P., et al., 1998, ApJ, 507, 46

Schubert E., Sander J., Ester M., Kriegel H. P., Xu X., 2017, ACM Transactions on Database Systems (TODS), 42, 19

Schulze S., et al., 2018, MNRAS, 473, 1258

Scolnic D. M., et al., 2018, ApJ, 859, 101

Scovacricchi D., Nichol R. C., Bacon D., Sullivan M., Prajs S., 2016, MNRAS, 456, 1700

Sevilla I., et al., 2011, arXiv e-prints, p. arXiv:1109.6741

Shiode J. H., Quataert E., 2014, ApJ, 780, 96

Smartt S. J., 2009, ARA&A, 47, 63

Smith N., 2014, ARA&A, 52, 487

Smith N., Owocki S. P., 2006, ApJ, 645, L45

Smith G. A., et al., 2004, in Moorwood A. F. M., Iye M., eds, Society of Photo-Optical Instrumentation Engineers (SPIE) Conference Series Vol. 5492, Ground-based Instrumentation for Astronomy. pp 410–420, doi:10.1117/12.551013

Smith N., et al., 2007, ApJ, 666, 1116

Smith M., et al., 2016, ApJ, 818, L8

Smith M., et al., 2018, ApJ, 854, 37

Sooknunan K., et al., 2018, arXiv e-prints, p. arXiv:1811.08446

Stritzinger M., Moriya T., 2018, arXiv e-prints, p. arXiv:1801.06643

Student 1908, Biometrika, pp 1–25

Sullivan M., et al., 2006, ApJ, 648, 868

Taam R. E., Sandquist E. L., 2000, ARA&A, 38, 113

Valens 1999, `http://math.ecnu.edu.cn/~qgu/friendintro.pdf`

Van Dyk S. D., Li W., Filippenko A. V., 2003, PASP, 115, 1

Vernet J., et al., 2011, A&A, 536, A105

Villar V. A., Nicholl M., Berger E., 2018, ApJ, 869, 166

Vinko J., et al., 2017, ApJ, 837, 62

Vreeswijk P. M., et al., 2014, ApJ, 797, 24

Vreeswijk P. M., et al., 2017, ApJ, 835, 58

Wang B., Han Z., 2012, New Astron. Rev., 56, 122

Webbink R. F., 1984, ApJ, 277, 355

Wheeler J. C., Harkness R. P., 1986, in Madore B. F., Tully R. B., eds, Vol. 180, NATO Advanced Science Institutes (ASI) Series C. pp 45–54

Whelan J., Iben Icko J., 1973, ApJ, 186, 1007

Wirtz C., 1918, Astronomische Nachrichten, 206, 109

Woodgate B. E., et al., 1998, Publications of the Astronomical Society of the Pacific, 110, 1183

Woosley S. E., 2010, ApJ, 719, L204

Woosley S. E., Blinnikov S., Heger A., 2007, Nature, 450, 390

Xue Y. Q., et al., 2011, ApJS, 195, 10

Yan L., et al., 2017, ApJ, 840, 57

Young D. R., et al., 2010, A&A, 512, A70

Yuan F., et al., 2015, MNRAS, 452, 3047

Zwicky F., 1938a, Physical Review, 53, 1019

Zwicky F., 1938b, ApJ, 88, 529

Zwicky F., 1942, ApJ, 96, 28

da Silva L. A. L., 1993, Ap&SS, 202, 215

van den Bergh S., Tammann G. A., 1991, ARA&A, 29, 363

FORM UPR16

Research Ethics Review Checklist

University of Portsmouth

Please include this completed form as an appendix to your thesis (see the Postgraduate Research Student Handbook for more information

Postgraduate Research Student (PGRS) Information			**Student ID:**	UP793777
PGRS Name:	Benjamin Thomas			
Department:	ICG	**First Supervisor:**	Bob Nichol	
Start Date: (or progression date for Prof Doc students)	**01/10/15**			

Study Mode and Route:	Part-time ☐	MPhil ☐	MD ☐
	Full-time ☒	PhD ☒	Professional Doctorate ☐

Title of Thesis:	The Volumetric Rate of Superluminous Supernovae from the Dark Energy Survey
Thesis Word Count: (excluding ancillary data)	36228

If you are unsure about any of the following, please contact the local representative on your Faculty Ethics Committee for advice. Please note that it is your responsibility to follow the University's Ethics Policy and any relevant University, academic or professional guidelines in the conduct of your study

Although the Ethics Committee may have given your study a favourable opinion, the final responsibility for the ethical conduct of this work lies with the researcher(s).

UKRIO Finished Research Checklist:
(If you would like to know more about the checklist, please see your Faculty or Departmental Ethics Committee rep or see the online version of the full checklist at: http://www.ukrio.org/what-we-do/code-of-practice-for-research/)

a)	Have all of your research and findings been reported accurately, honestly and within a reasonable time frame?	YES ☒ NO ☐
b)	Have all contributions to knowledge been acknowledged?	YES ☒ NO ☐
c)	Have you complied with all agreements relating to intellectual property, publication and authorship?	YES ☒ NO ☐
d)	Has your research data been retained in a secure and accessible form and will it remain so for the required duration?	YES ☒ NO ☐
e)	Does your research comply with all legal, ethical, and contractual requirements?	YES ☒ NO ☐

Candidate Statement:

I have considered the ethical dimensions of the above named research project, and have successfully obtained the necessary ethical approval(s)

Ethical review number(s) from Faculty Ethics Committee (or from NRES/SCREC):	7D76-B735-557A-86D8-3 8D3-E544-F27B-E50A

If you have *not* submitted your work for ethical review, and/or you have answered 'No' to one or more of

questions a) to e), please explain below why this is so:		
N/A		
Signed ***(PGRS)*:**		**Date:** 28/06/19